CMR-77-1

ADA037399
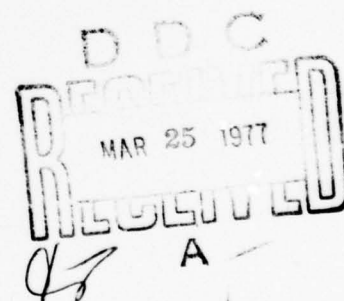
ANNUAL TECHNICAL REPORT

LONG RANGE MATERIALS RESEARCH

Sponsored by

Defense Advanced Research Projects Agency

ARPA Order No. 3018

January 1977

The views and conclusions contained in this document are those
of the authors and should not be interpreted as necessarily
representing the official policies, either expressed or implied,
of the Defense Advanced Research Projects Agency or the U. S.
Government.

CENTER FOR MATERIALS RESEARCH

STANFORD UNIVERSITY • STANFORD, CALIFORNIA

⑨ CMR-77-1

⑭

ANNUAL TECHNICAL REPORT. (Final)
1 Jan - 31 Dec 76, P2

⑥ Long Range Materials Research .

Sponsored by
Defense Advanced Research Projects Agency
ARPA Order No. 3018

Program Code Number: 5D10

Contractor: Leland Stanford, Jr. University

Effective Date of Contract: June 1, 1975

Contract Expiration Date: December 31, 1976

Amount of Contract: $183,400

⑮ Contract Number: N00014-75-C-1171 // ARPA Order - 3018

Principal Investigator: Robert A. Huggins
Phone: (415) 497-4118
⑩
Short Title: Long Range Materials Research

⑪ January 1977   ⑫ 148p.

The views and conclusions contained in this document are those
of the authors and should not be interpreted as necessarily
representing the official policies, either expressed or implied,
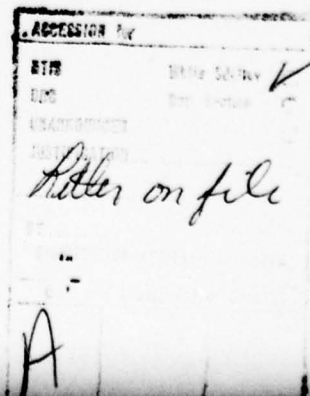of the Defense Advanced Research Projects Agency or the
U. S. Government.

Center for Materials Research
Stanford University
Stanford, California 94305
(415) 497-4118

400827

2B

TABLE OF CONTENTS

ii

I. GENERAL INTRODUCTION

I. GENERAL INTRODUCTION

This technical report on the research program entitled
"Long Range Materials Research," covers the time January 1
through December 31, 1976 and is a final report on two of the
following separate programs composing this program:

1. Detection of X-Ray Radiation

2. Superplasticity and Warm Working of Metals and Alloys

3. Synthesis of New Types of Catalyst Materials

4. Development of Elevated Temperature Electrocrystallization
   Techniques

The programs Detection of X-Ray Radiation (1) and Synthesis
of New Types of Catalyst Materials (3) are completed as of
December 31. The research entitled Superplasticity and Warm
Working of Metal and Alloys (2) is continuing as another program
under another contract.

The remaining program, Development of Elevated Temperature
Electrocrystallization Techniques (4) is continuing under the
present contract.

Reports of each of these programs will be described separately
in the succeeding sections of this report.

II. DETECTION OF X-RADIATION

C. W. Bates, Jr.

Associate Professor of Materials Science
and Engineering
and Electrical Engineering

A. Introduction

This is the final report of a three year study of basic luminescent phenomena in CsI and CsI(Na) which are very efficient detectors of ultraviolet and X-radiation respectively. Two graduate students involved in these studies have received their Ph.D.'s. Dr. Akinola Salau of the Applied Physics Department at Stanford University, received his degree for his work on "Luminescence Studies in CsI" and is presently a Lecturer in the Physics Department at the University of Ife, Ife, Nigeria. Dr. Olive Lee Hsu received her degree for her studies on "Excitonic Emission from CsI(Na)" from the Department of Materials Science and Engineering at Stanford University and is presently employed by Diagnostic Information, Inc. of Sunnyvale, California, a company involved in the manufacture of X-Ray Image Intensification Systems for Diagnostic Radiology. Both of their work have contributed significantly to a more fundamental understanding of these materials as they relate to the detection of X-radiation.

Abstracts of their work constitute the technical part of this report and copies of their complete work are included as a supplement.

B. Investigation of Luminescence from Trapped Excitons in CsI

The ultraviolet absorption, photoluminescence, and electron spin resonance (ESR) of pure CsI which had not been exposed to ionizing radiation and which was relatively strain and defect free was studied between room and

-4-

liquid helium temperatures. Bulk single crystals were used in the photo-
luminescence and ESR experiments and both bulk single crystals and thin
films 500 $\overset{o}{A}$ - 2000 $\overset{o}{A}$ thick were employed for taking the ultraviolet absorption
data. These samples were mounted on a copper block with silicon vacuum grease
to provide thermal contact between sample and copper. At room temperature
before cooling no emissions or ESR signals were observed for any of the samples
investigated. As the temperature was lowered to that of liquid nitrogen, two
emissions with λ_{max} at 420 and 350 nm appear for excitation in the 205 - 235 nm
range, i.e. from the excitonic region to the long wavelength tail of the
fundamental absorption. The 350 nm emission is excited most efficiently in
the excitonic region 205 - 225 nm, whereas the 420 nm emission is more readily
produced by excitation in the long wavelength tail of the fundamental ab-
sorption at 235 nm. This general behavior continues down to liquid helium
temperature. At the temperature of liquid helium (4.2^{o}K) an emission at 2900 $\overset{o}{A}$
appears under excitation in the excitonic region and disappears at ~25°K.
This emission has been observed by other workers and was proposed to be due
to radiative recombination of a free electron with a V_K-center. However,
our results show that this emission results from radiative recombination of
a trapped electron (F-center) with a V_K-center.

An interesting effect has been observed when the samples are
temperature cycled between room and liquid nitrogen and lower temperatures.
Emissions which were not present at room-temperature-before-cooling (RTBC) appear
in the 350 - 550 nm range depending on the excitation wavelength. It has been
found that the intensities of these room-temperature-after-cooling luminescences
(RTAC) are approximately 30 - 40 percent stronger when the samples are exposed
to radiation in the 205 - 235 nm range when at the lower temperatures before
warming back to room temperature, relative to samples which were not similarly
exposed.

ESR data were taken on pure single crystals of CsI and single crystals of CsI doped with thallium (0.1 mole percent) and sodium (0.01 mole percent). Experiments were performed on the doped samples which are known from previous studies to produce stable hole centers at liquid nitrogen temperatures to compare with the pure samples which under conditions of high gain hint at the presence of an anisotropic hole-like paramagnetic center. At room temperature the pure samples showed no ESR signals. Cooling slowly to about 80°K produced an ESR signal described by magnetic parameters indicating the presence of an F-center. The signal is characterized by a g-value of 2.003 ± 0.001 with a peak-to-peak linewidth of 100 Gauss and is isotropic in nature. The signal intensity increased as the temperature was lowered to 80°K and changed very little between 80°K and 20°K, the maximum amplitude occurring between $60^\circ - 70^\circ$K, with the signal intensity remaining isotropic. The signal persists upon warming back to room temperature which correlates quite nicely with the optical data. Efforts to correlate the hole-like centered observed in pure CsI with hole-centers observed in CsI(Tℓ) and CsI(Na) were only moderately successful.

Using the theoretical model developed by Bassani and Inchauspé for determining the positions of the α and β-bands in CsI we obtain values of 235 ± 5 nm and 224 ± 2 nm respectively for these bands, which coincide with the peaks observed in the excitation spectra for the 350 and 420 nm emissions, further suggesting that the observed emissions are due to the annihilation of excitons bound to negative ion vacancies (α-bands) and excitons bound to F-centers (β-bands). These observations seem to imply that in pure CsI cooling to liquid nitrogen and lower temperatures produces traps for both electrons and holes which do not release them upon warming back to room temperature and that these centers are responsible for the luminescence observed at RTAC.

C. Excitonic Emission from CsI(Na)

Photoluminescence in CSI(Na) was studied. This work used non-ionizing light sources and obtained the data from well-annealed, zone-refined specimens. A series of absorption excitation and emission spectra were measured at temperatures between $300^{\circ}K$ and $4.2^{\circ}K$. There are strong absorption bands on the long wavelength side of the fundamental absorption edge of the host CsI crystal. The excitation spectra are closely related to the absorption bands. The emission spectra consist of the characteristic blue emission and other low temperature emissions. The emission spectra were decomposed into the super-position of Gaussian peaks by computer. It is found for the first time that the characteristic emission consists of two bands, centered at 4200 Å and 3700 Å respectively. The latter one increased as the temperature decreased.

The energies of localized excitons were calculated by employing a Born-Haber cycle. The calculated results were compared with the measured absorption and excitation spectra. Each absorption and excitation band was identified as the transition of either a free or a localized exciton. The most important one is the exciton created by transferring an electron from an iodine ion to a substitutional sodium ion. This localized exciton called "impurity" exciton is responsible for the absorption peak and the excitation band of the characteristic emission. The β exciton also contributes to this absorption and excitation at low temperatures.

A configuration coordinates diagram is proposed to explain the evolution of the two characteristic emission bands. The diagram consists of the ground state and two excited states.

Two polarization experiments were carried out in order to understand the symmetry of the characteristic luminescent center. Neither of the two characteristic emission bands was polarizable. The absorption spectrum of

an ultraviolet irradiated CsI(Na) crystal was measured at 15°K. No evidence of the existence of V_k centers was found. It is concluded that during the relaxation of "impurity" excitons, isolated V_k centers are not necessarily formed.

III. SUPERPLASTICITY AND WARM WORKING

OF METALS AND ALLOYS

O. D. Sherby

Professor of Materials Science
and Engineering

A. Summary of Accomplishments

Much has been accomplished since our last semi-annual progress report (January 1976). A fair portion of our time has centered on optimizing the processing variables for obtaining desirable superplastic and low temperature strength properties in our ultrahigh carbon steels. Several invited talks were given on the UHC steels since the last quarterly progress report attesting to the continued high outside interest in our work. These include a talk at Stanford Research Institute (July 21, 1976), at the Fourth International Conference on Mechanical Porperties of Metals and Alloys in Nancy, France (September 2, 1976), at the San Fernando Valley Chapter of ASM (October 26, 1976) and at the Los Alamos Chapter of ASM (December 14, 1976). A number of visitors were received at Stanford who came for the specific purpose of learning, first hand, our research effort on the UHC steels. Among several such visitors were Dr. Klaus Frommann of DeMag AG, Duisburg, Germany, Dr. R. D. Goolsby of Vought Corporation, Dallas, Texas and Mr. James Fayal of Greene Plastics Corp., Hope Valley, Rhode Island.

One publication and one issued patent have resulted since the last progress report. A paper authored by Bruno Walser, E. Sabri Kayali and Oleg D. Sherby has been published in the Conference Proceedings of the Fourth International Conference on the Strength of Metals and Alloys, Nancy, France (30 August - 3 September 1976). The paper is entitled "Warm Working and Superplasticity in Plain Ultrahigh Carbon Steels". A patent entitled "Superplastic Ultrahigh Carbon Steel" has been issued to the Board of Trustees of Leland Stanford Junior University. The inventors are Oleg D. Sherby, Conrad M. Young, Bruno Walser and Eldon M. Cady. The patent number is 3,951,697 and it was issued on April 30, 1976. The Office of Technology Licensing at Stanford University has filed this patent in Germany, England and Japan.

In the following sections we summarize our accomplishments in four
areas related to our work on warm working and superplasticity in ultrahigh
carbon steels. The first section (B) summarizes the work of Sabri Kayali
whose doctoral thesis covers the superplastic properties of eutectoid steel
and ultrahigh carbon content iron-carbon alloys (1.6 and 1.9% carbon). The
second section (C) covers the influence of heat treatment on the hardness
and compression strength of our UHC steels; this was the basis of an investi-
gation by visiting Professor H. Sunada of Himeji University, Japan and is
being completed by Dr. Jeffrey Wadsworth. The third section (D) summarizes
our work on powder metallurgy of UHC steel powders. Robert Caligiuri has
successfully demonstrated that high densification is readily achieved when
UHC steel powders contain a fine structure; superplastic flow mechanisms
clearly permit rapid densification at low temperatures and low pressures.
The fourth and last section (E) summarizes our views on superplasticity which
was presented at the ARPA Workshop on fine structures held at La Jolla,
California on July 14, 1976.

(B) Superplasticity of Euctectoid Steel and Iron-Carbon Alloys (of Ultrahigh
    Carbon Content).

E. S. Kayali

Superplasticity of a eutectoid composition steel and pure iron-carbon
alloys were studied and the major results and conclusions are outlined in the
following paragraphs.

The outstanding microstructural characteristic of superplastic materials
is their ultrafine grain size. Therefore production of ultrafine grain size
was considered essential for this study and several thermal-mechanical
processing techniques were developed to obtain fine grained structures.
One method of producing fine grained structures was by a cold working and

recrystallization process.   This processing technique led to a study of the
annealing behavior of severely cold worked iron-carbon alloys (0.0025%, 0.1%
and 0.8%C) based on hardness measurements and microstructural studies.   This
secondary study led to the following new observations:

i) The cold rolled iron-carbon alloys studied showed a hardness peak at about
300°C in the recovery range (Figure 1).   This peak is attributed to the forma-
tion of low-angle subgrain boundaries (Figure 2) which we consider as a
strengthening phenomenon.

ii) The magnitude of the hardness peak increased with increasing cementite
content.   This result was attributed to the increasing amount of stored energy
(higher dislocation densities) after cold-working with increasing cementite
content which leads to fine subgrains during recovery.

iii) The Fe-0.8%C alloy recrystallized at a lower temperature than those
observed for the Fe-0.1%C alloy and the electrolytic vacuum cast iron.   This
is probably due to the large amount of cementite in the Fe-0.8%C alloy.   The
work hardening capacity is increased by the presence of cementite resulting
in a very high dislocation density material.   The high stored energy present
leads to a strong driving force for recrystallization.   Thus, the Fe-0.8%C
alloy recrystallizes at a lower temperature ($\approx$ 400°C) than the other two
materials studied (500°C).

Superplasticity of a eutectoid steel and an iron-0.9%C alloy was studied
as a function of microstructure, temperature and strain rate.   These materials
were spheroidized and made fine grained by several thermal-mechanical processes.
Fine spheroidized structures of cementite in a ferrite matrix containing ferrite
grains and cementite particles finer than one micron were obtained by warm-
working, but the grain boundaries in this microstructure were a mixture of low
and high angle boundaries (Figure 3A).   The results of elevated temperature
tests in the temperature range 650-700°C showed that these materials were not

-12-
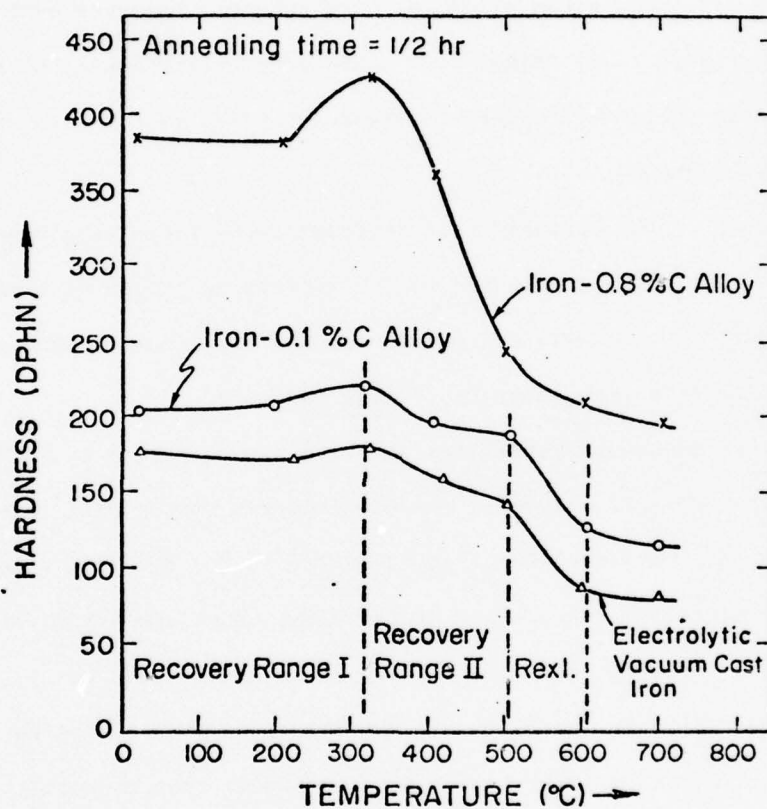
Figure 1. Influence of annealing temperature on the hardness of the severely cold-worked (85% cold-rolled) iron and iron-carbon alloys.
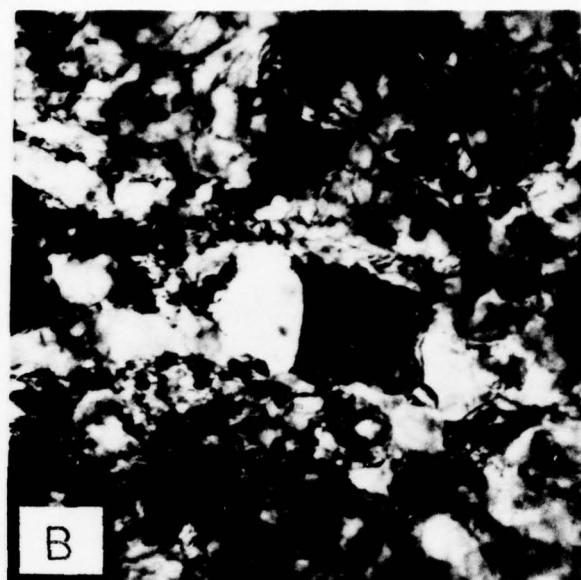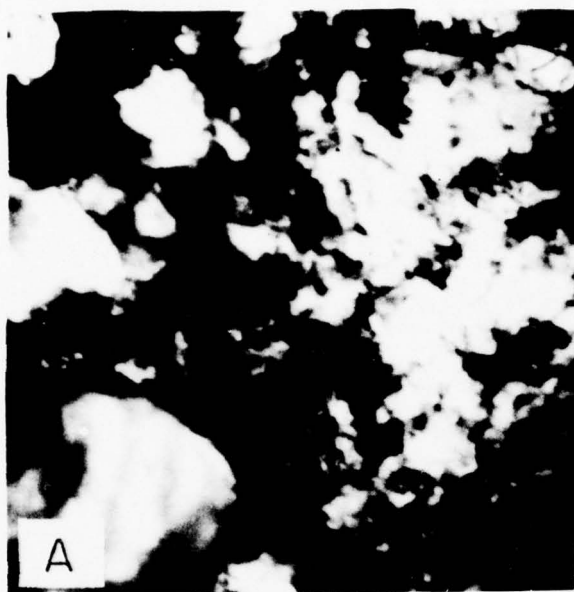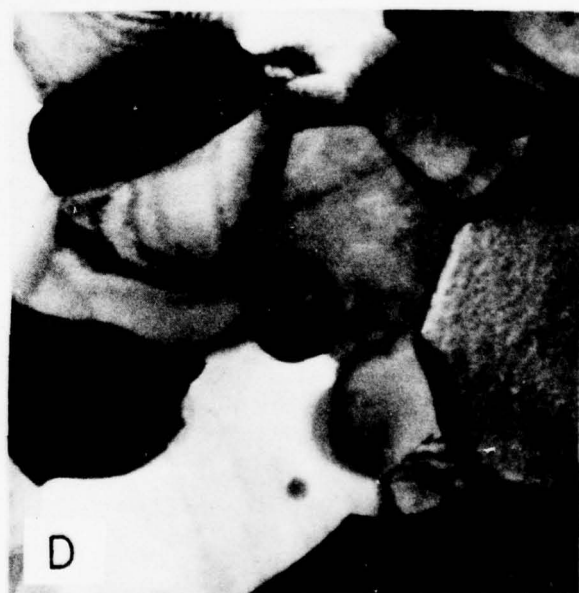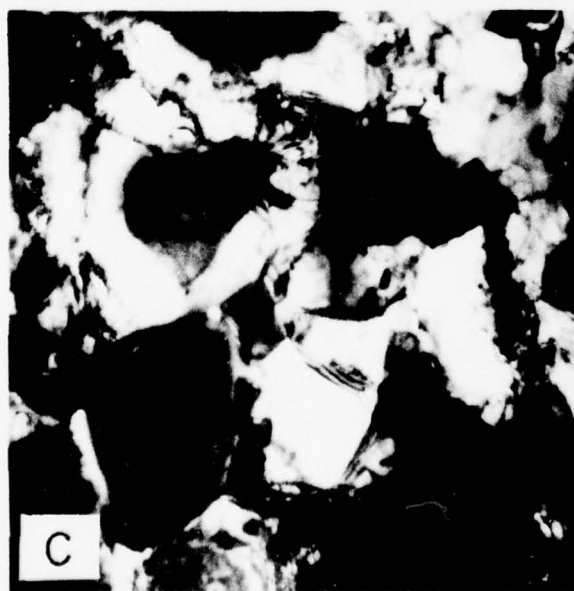
Figure 2. Microstructures of an initially 85% cold-rolled Fe-0.8%C alloy following annealing at different temperatures for 1/2 hour. A) at 200°C (hardness: 380 DPHN) B) at 325°C (hardness: 425 DPHN) C) at 400°C (hardness: 360 DPHN) D) at 500°C (hardness: 240 DPHN).

1 μm
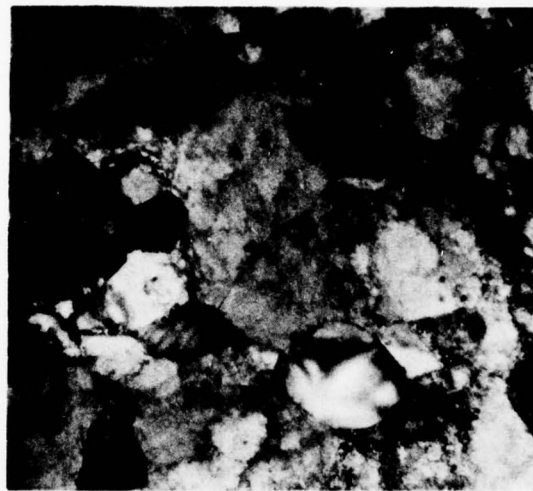
Figure 3. The microstructure of a eutectoid steel (A) as warm rolled at 500°C to a true strain of ε = 2.76, and (B) cold rolled then re-crystallized.
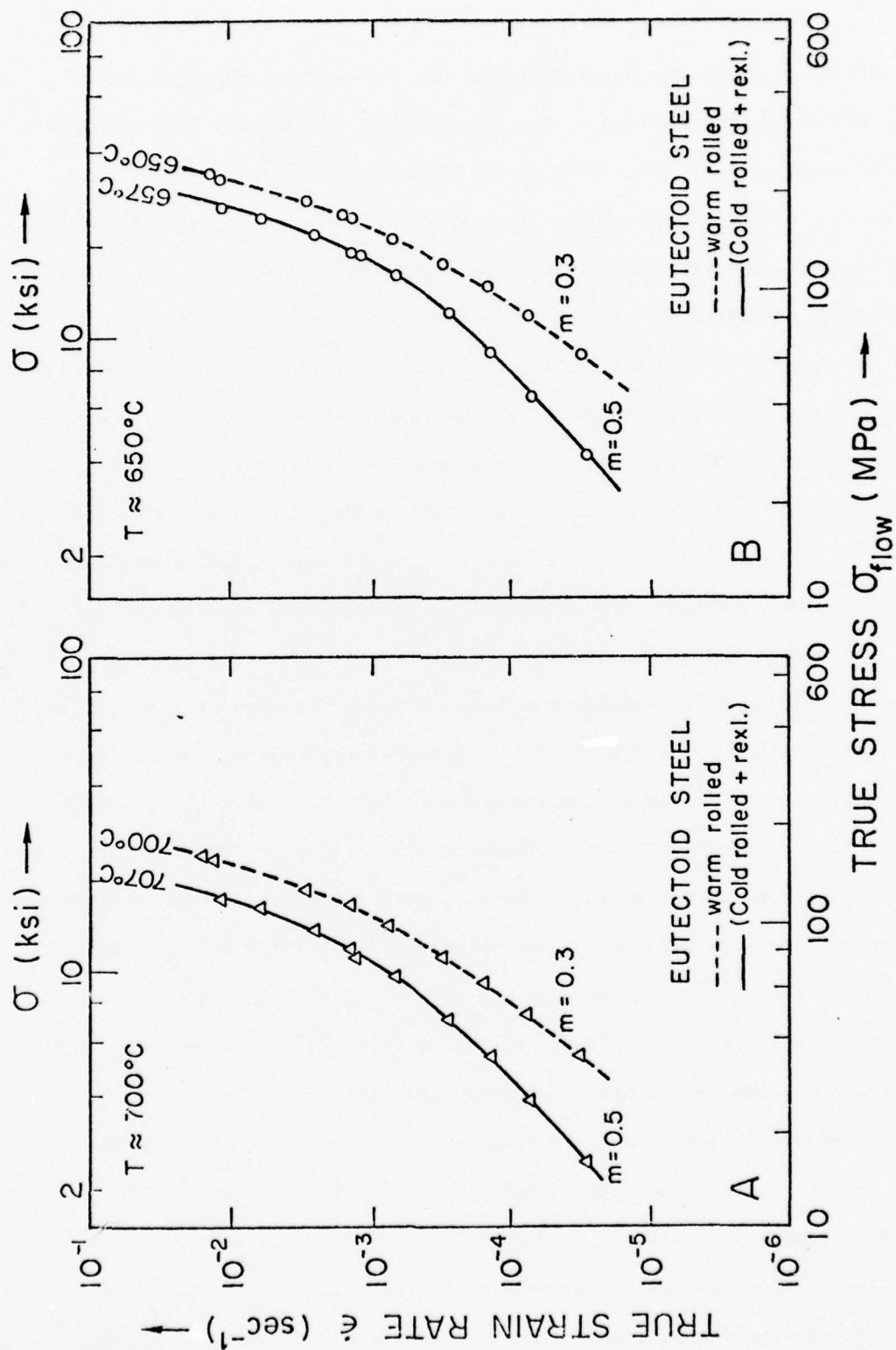
Figure 4. Flow stress-strain rate relationship for a eutectoid steel as warm rolled and as cold rolled then recrystallized. (A) at ≈ 700°C and (B) at ≈ 650°C.

ideally superplastic and the maximum strain rate sensitivity exponent (m) was about 0.3 for both materials at low strain rates (Figure 4). The maximum elongations observed were about 150% for the iron-0.8%C alloy and about 200% for the eutectoid composition steel. Fine spheroidized structures containing only high angle boundaries were obtained by a cold rolling and recrystallization process in both materials (Figure 3B illustrates an example for the eutectoid steel). The results of elevated temperature tests showed that these materials were superplastic and higher strain rate sensitivity exponents (m $\approx$ 0.5) and higher elongations (250%-400%) were achievable in recrystallized structures than in warm rolled structures (Figure 4). These results are related to the importance of the type of grain boundaries in fine grained equiaxed structures on superplastic deformation. Our consideration on the importance of the type of grain boundaries on superplastic flow is that superplastic deformation should become easier as the average misorientation angle increases since it is known that grain boundary sliding and grain boundary diffusivity both increase as the boundary angle increase from low angles (1-5°) to high angles ($\approx$ 20°). Our results seem to reveal convincing evidence that the nature of the grain boundary is an important variable in superplastic deformation and specifically that an increase in boundary angle enhances superplastic deformation. Figure 5 illustrates the influence of grain size and type of grain boundary on the resulting m value for the Fe-0.8%C alloy. The data of Marder is included in the correlation shown (A. R. Marder, Trans. AIME, 1969, 245, 1337).

Two mechanisms appeared to be involved in the elevated temperature deformation process of the fine grained eutectoid steel and the iron-0.8%C alloy studied. At low stresses ($\frac{\sigma}{E} < 4 \times 10^{-4}$) and low strain rates ($\dot{\epsilon} < 10^{-3} \sec^{-1}$), where the strain rate sensitivity exponents were high (m $\approx$ 0.3 to 0.5), the activation energy for the deformation process is similar to that for grain
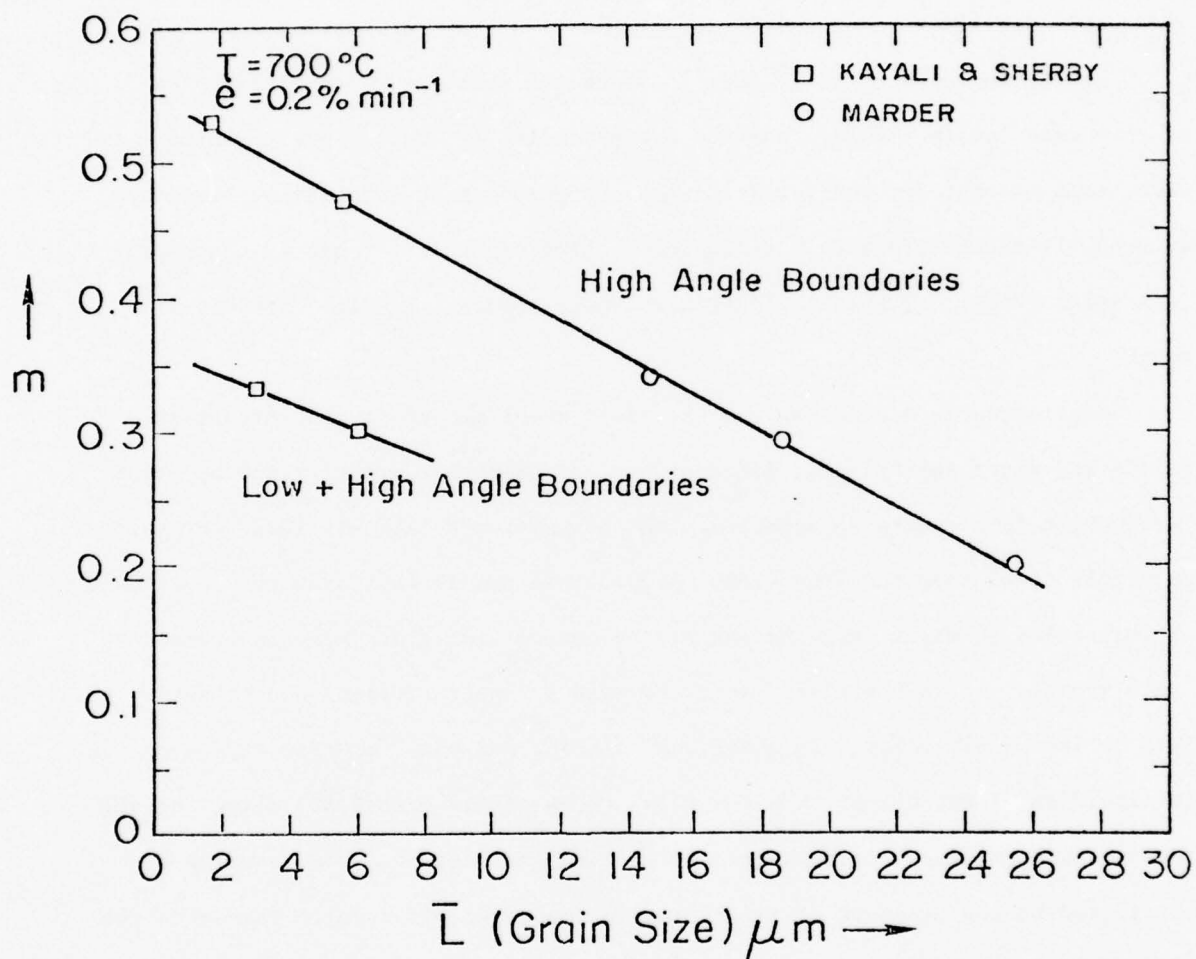
-17-

Figure 5. The effect of grain size on the strain rate sensitivity exponent in Fe-0.8%C alloys as influenced by the type of grain boundary present. High angle boundaries (obtained by a cold working and recrystallization treatment) reveal higher m values than a mixture of high and low angle boundaries (as obtained by warm working).

boundary diffusion. These high strain rate sensitivity exponent values and

corresponding grain boundary activation energy values suggest that the pre-

dominant deformation mechanism is grain boundary sliding, a mechanism which

apparently dominates superplastic deformation. At high stresses ($\frac{\sigma}{E} > 4 \times 10^{-4}$)

and high strain rates ($\dot{\varepsilon} > 10^{-3} sec^{-1}$), where the strain rate sensitivity ex-

ponents were low (m $\approx$ 0.15), and the corresponding activation energy values

were close to that for lattice diffusion the predominant deformation mechanism

is probably associated with a dislocation climb controlled recovery creep pro-

cess (slip creep). Figure 6 illustrates these observations in a graphical

sense.

Metallographic studies on the eutectoid steel and the iron-0.8%C alloy

before and after superplastic deformation indicated that grain growth occurred

during high temperature deformation. The grain growth rate was lower for the

eutectoid steel than the iron-0.8%C alloy. This result indicates the importance

of impurities in steel (e.g. Mn and Si) in controlling grain size and retarding

grain growth. It is therefore easier to make a eutectoid steel superplastic

than an iron-0.8%C alloy. An additional finding was that the flow stress of the

eutectoid steel was higher than the flow stress of the iron-0.8%C alloy for all

strain rates studied when compared at the same grain size. This result was

attributed to the presence of impurities in the eutectoid steel. The above two

observations lead to the following conclusions. Impurities in steel(such as

Mn, Si and Ni) extend superplastic behavior to a wider strain rate range in the

eutectoid steel than in the Fe-0.8%C alloy, and they retard grain growth during

high temperature deformation.

Superplasticity studies on hypereutectoid iron-carbon alloys (1.6 and 1.9%C)

containing no intentional impurities revealed that these alloys cannot be made

superplastic. A number of complex thermal-mechanical processing techniques were

-19-
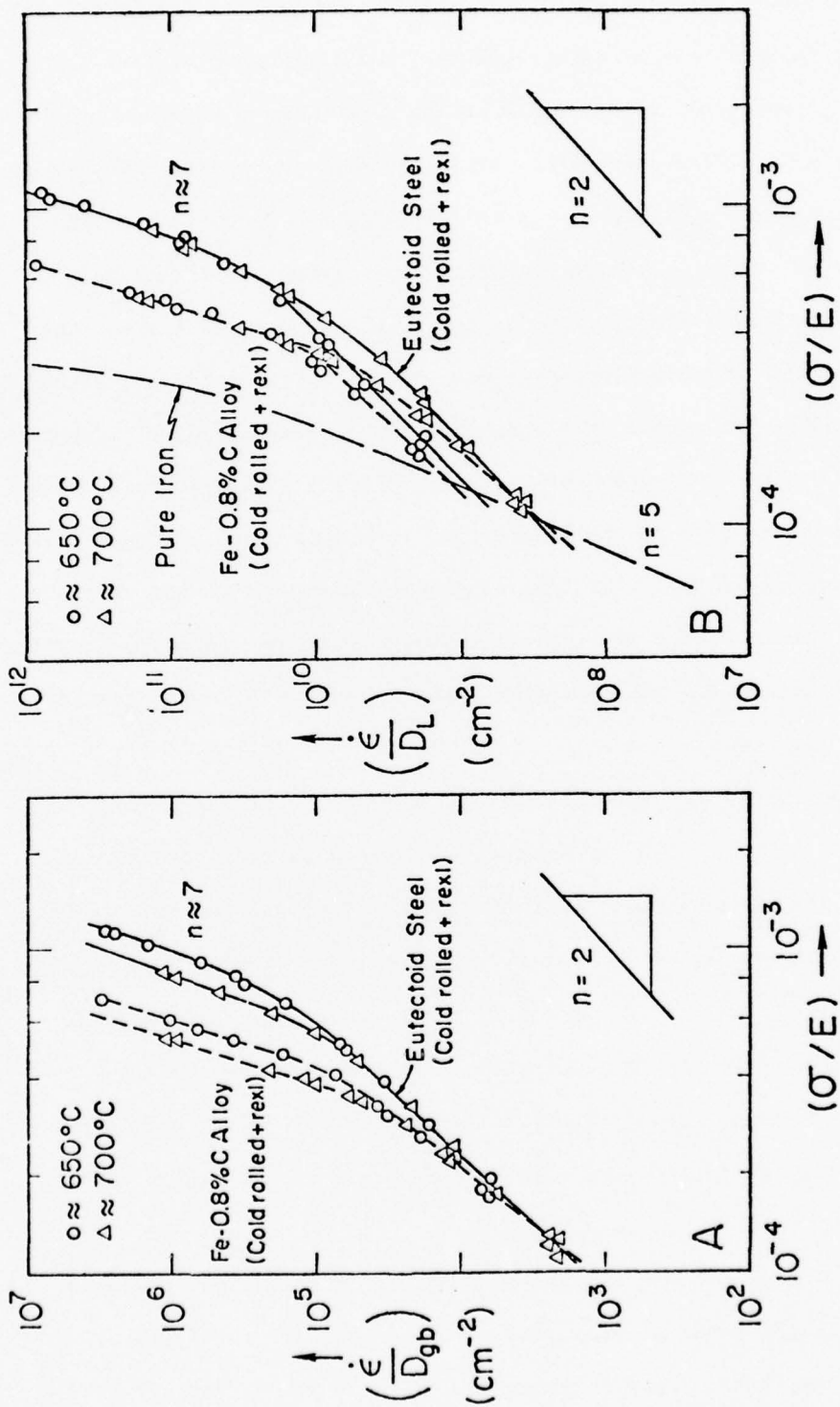
Figure 6. Comparisons of the creep data for the cold rolled and recrystallized Fe-0.8%C alloy and the eutectoid steel. Two different diffusivities (D_L and D_{gb}) were used in correlations of the data for these materials. This is because, at low stresses and strain rates, the activation energy of the deformation process is close to that for grain boundary diffusion while at high stresses and strain rates, the activation energy corresponds to that for lattice diffusion.

developed, none of which contributed to high strain rate sensitivity (m ≈ 0.15) or high ductility (elongations of about 50-75%). Metallographic studies revealed that these iron-carbon alloys could not be made to have fine equiaxed grains with fully spheroidized cementite particles under the thermal-mechanical processing conditions used (Figure 7). A cold rolling and recrystallization process could not be used on the hypereutectoid iron-carbon alloys, because it was not possible to roll them at room temperature due to their limited ductility.

In earlier studies on this program it was shown that fine equiaxed structures were obtained in ultrahigh carbon steels containing the same amount of cementite as those studied for the iron-carbon alloys. The ultrahigh carbon steels were superplastic whereas the high purity iron-carbon alloys were not. These results indicate the importance of Mn and Si (the principal impurities in the ultrahigh carbon steels) on obtaining fine structures during thermal-mechanical processing and in controlling grian size and retarding grain growth during superplastic deformation.

The activation energy for plastic deformation of the coarse-grained hypereutectoid Fe-1.6%C alloy was calculated to be close to that for the lattice diffusion of α-iron between 600°C and 700°C. The observed low strain rate sensitivity exponent (m ≈ 0.15 or n = 7) and corresponding lattice diffusion activation energy values suggest that the predominant deformation mechanism is slip creep for the hypereutectoid iron-carbon alloys in the strain rate-stress range studied. Figure 8 illustrates the difference in behavior of the ultrahigh carbon Fe-C alloys compared to the ultrahigh carbon steels.

An alternate heat-quench process was developed to produce fine equiaxed structures in ultrahigh carbon steels. This process consisted of multiple phase transformations, the purpose of which was to break up the cementite

-21-
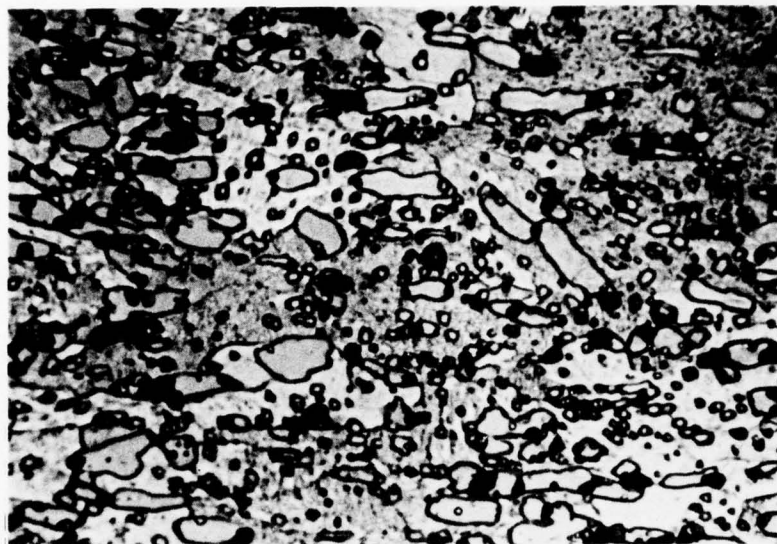
Fe – 1.6% C ALLOY

|10 μm|
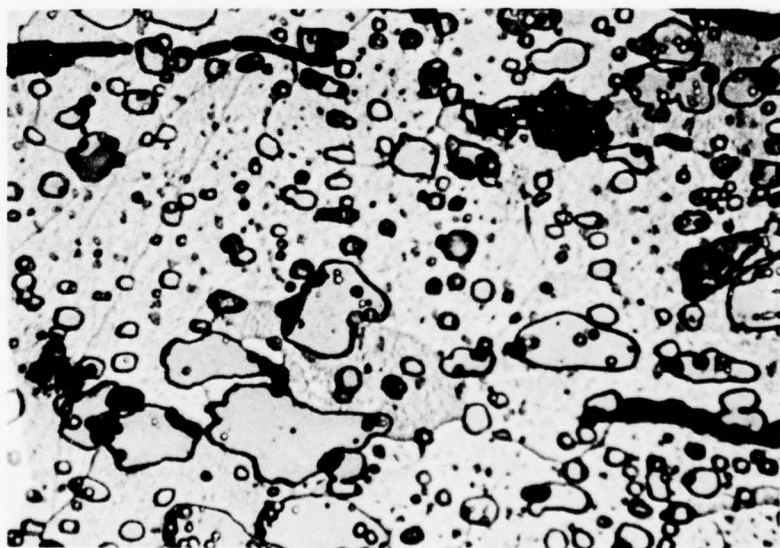
Fe – 1.9% C ALLOY

Figure 7. Optical micrographs of a warm worked Fe-1.6%C alloy and a warm worked Fe-1.9%C alloy. Note that cementite did not fully break up to a fine spheroidized form and ferrite grains are coarse and elongated.
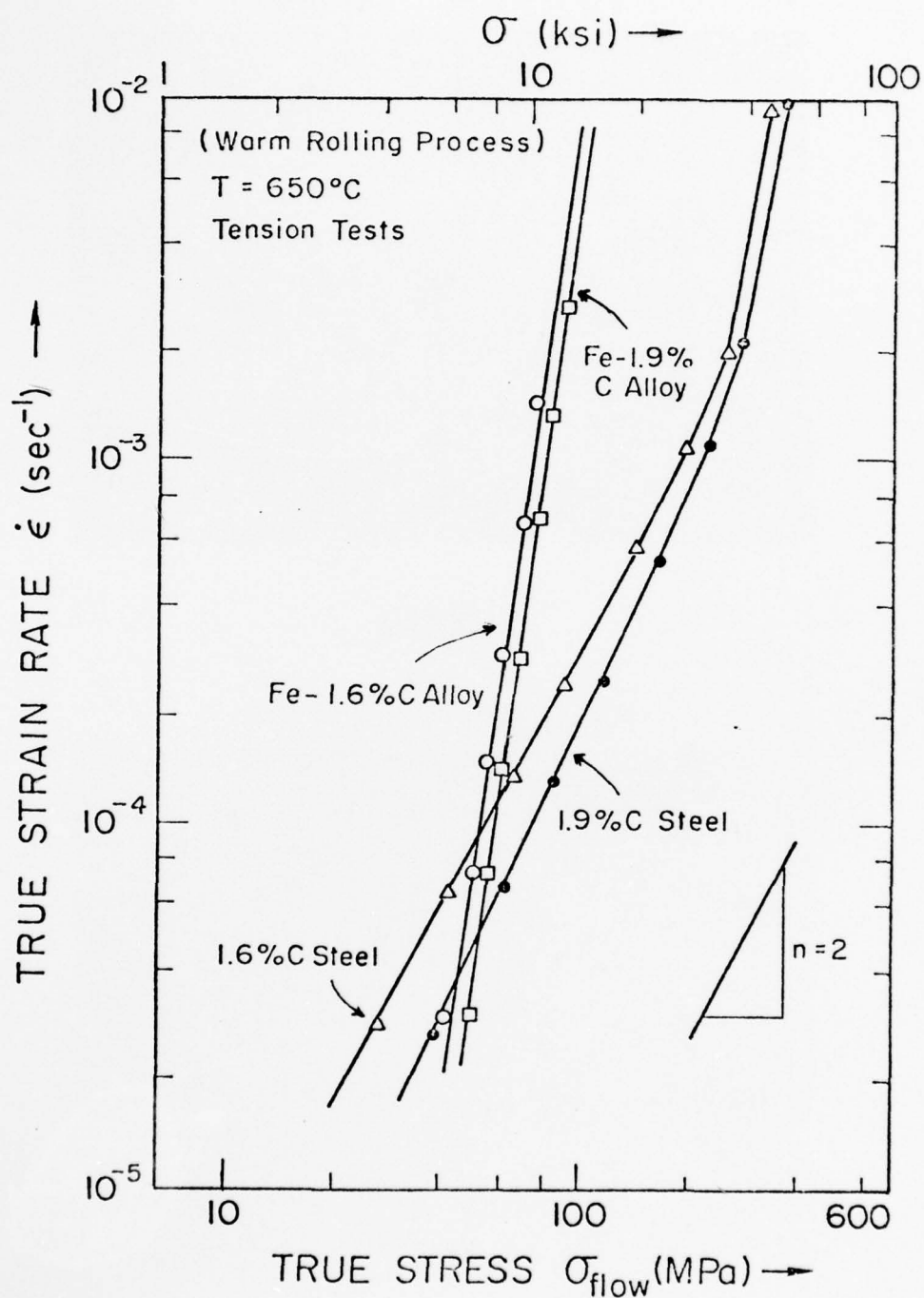
Figure 8. Strain rate-flow stress relations for extensively warm worked hypereutectoid iron-carbon alloys and ultrahigh carbon steels containing the same amounts of carbon (1.6 and 1.9%C). Strain rate-flow stress relations were obtained from strain rate change tests in tension.

structure through internal stresses from the volume changes upon transformation. It was shown that the structure is gradually refined as the number of thermal cycles is increased. Fourteen heat-quench cycles produced fine equiaxed ferrite grains ($\approx 3\mu m$) and spheroidized cementite particles; ultrahigh carbon steels with this fine structure showed an elongation of 330% and a high strain rate sensitivity exponent ($m \approx 0.5$). The change in the flow stress-strain rate relation with thermal cycling is shown in Figure 9. And, Figure 10 illustrates the enhancement in tensile ductility at 650°C as a function of thermal cycling.

C.) Influence of Heat Treatment on the Compression Strength of Fine-Grained, Ultrahigh Carbon Steels

H. Sunada and J. Wadsworth

Fine-grained ultrahigh carbon steels which are superplastic at warm temperatures have potentially unique room temperature properties in the heat treated condition. This is because the particulate structure of fine cementite ($0.1\mu m$) is fine grained ferrite ($\sim 1\mu m$), when taken to just above the A_1 temperature (723°C), should transform to fine grained austenite with cementite which, upon quenching, should produce an exceptionally fine martensite which contains cementite. This concept of the optimum heat treatment temperature for hypereutectoid steel is not new - it was suggested in 1926 by Sauveur who perceived that the ideal hardening temperature for these steels was the one described above.

In this section we describe the first results of experiments to determine the properties of heat-treated ultrahigh carbon steels. Two steels, one of carbon content 1.3% and the other of 1.6%, were chosen. Their full composition and thermo-mechanical history is shown in Table 1. Compression and hardness tests were carried out on specimens cut from the rolled strip.

Cylinders for compression tests were 3.175 mm in diam. and 4.83 mm in height whilst hardness samples were plates of dimensions 12.7 mm x 12.7 mm x 3 mm.

-24-
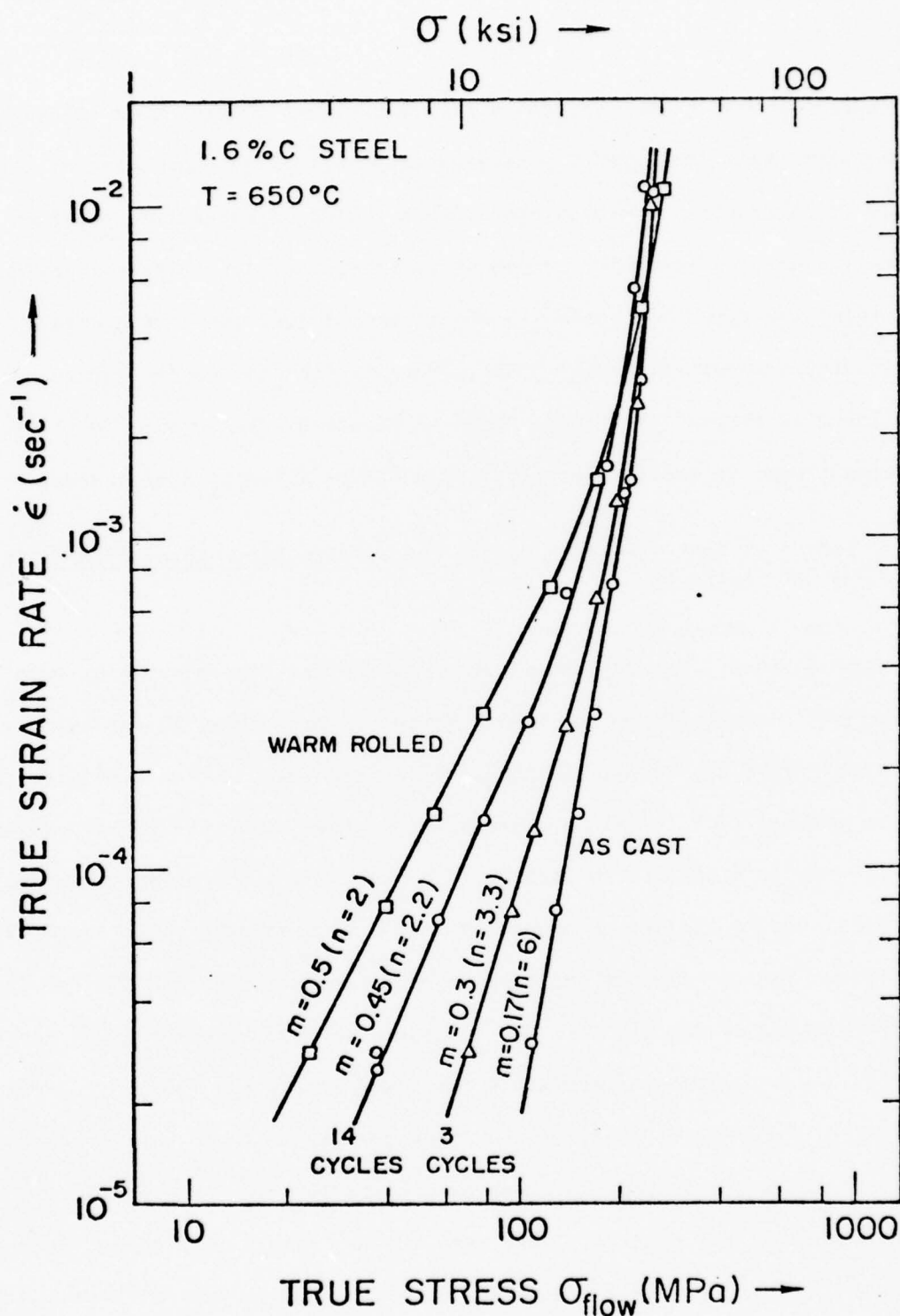
Figure 9. Strain rate-flow stress relations for a 1.6%C steel in the as cast state and after thermal cycling through the alpha-gamma phase transformation. Strain rate-flow stress relation of a warm rolled 1.6%C steel is also included. The data were obtained by strain rate change tests in tension.
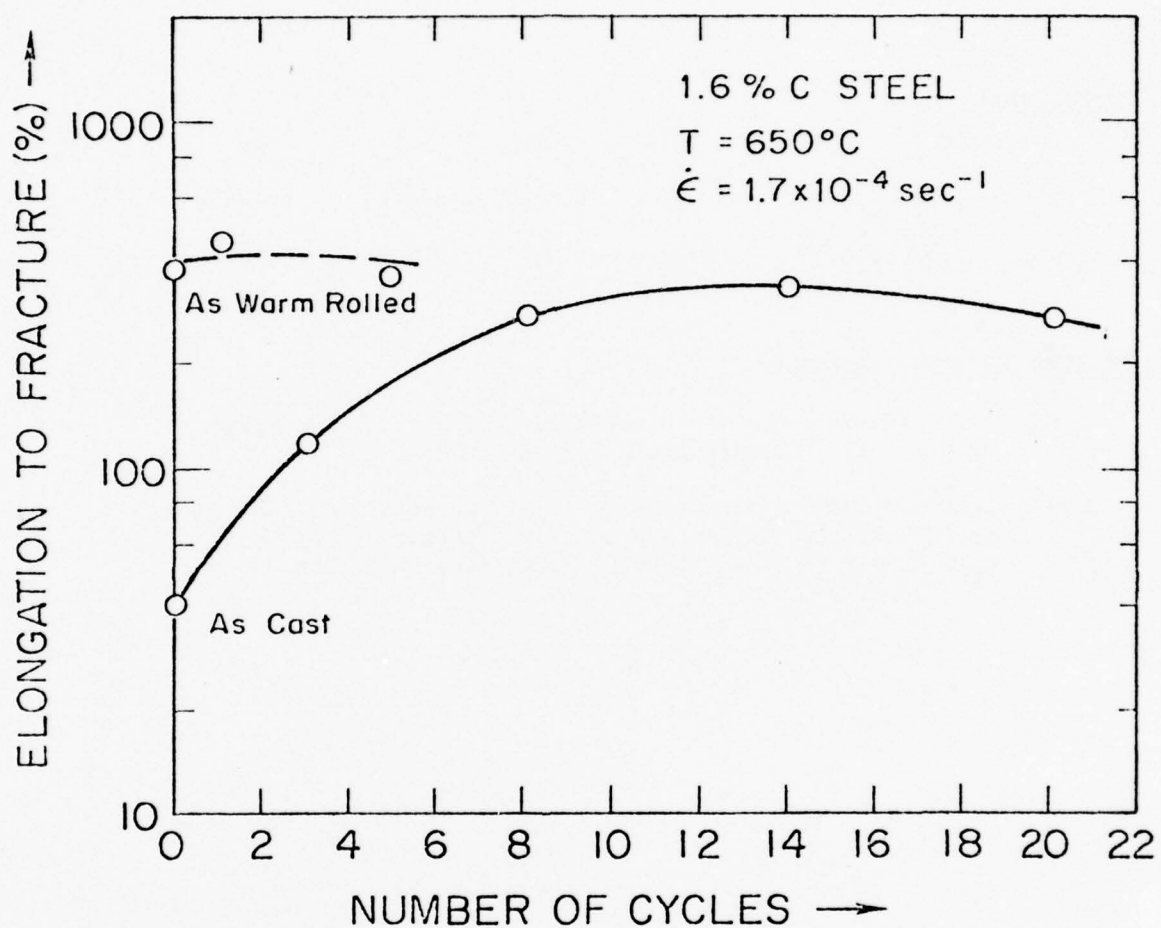
Figure 10. Effect of number of thermal cycles on the total elongations of a 1.6%C steel. The elongations to fracture of a cast 1.6%C steel and a warm rolled 1.6%C steel after various thermal cycles are shown as obtained at 650°C with an initial strain rate of 1.7×10^{-4} sec^{-1} (1% min^{-1}).

TABLE 1

a) COMPOSITION

	C	Mn	Si	Mn	S	Fe
1.3%C	1.25	0.65	0.10	0.016	0.024	Balance
1.6%C	1.57	0.73	0.28	0.015	0.020	Balance

b) THERMOMECHANICAL TREATMENT

1.3%C   1120°C/60 min. → oil Q → → 650°C, rolled to a true strain
of ε = 1.42.   Ferrite grain size about 2μm.

1.6%C   1100°C → 600°C during rolling to a true strain of 1.67 then
isothermally rolled at 595 to a true strain of 1.1
$\varepsilon_T = \varepsilon_\gamma + \varepsilon_\alpha$ = 2.77.   Ferrite grain size about 2μm.

With the exception of specimens quenched from 750°C (one-step austenitizing)
the specimens were two-step austenitized. This consisted of holding the specimen
at a temperature T_1 (850°C to 1150°C) for 30 min., cooling to a constant second
temperature T_2 (in this case 750°C) and holding for 30 min., quenching into water
and finally quenching into liquid nitrogen. An iron-carbon phase diagram with
an illustration of the one-step austenitizing treatment is shown in Figure 11.
The liquid nitrogen quench was added to transform any retained austenite at room
temperature and to stabilize the transformation products. The purpose of the
first austenitizing treatment is to grow the austenite grains to differing degrees.
The purpose of the second step (T_2) is to maintain a constant carbon content
in the matrix for each treatment thereby eliminating influences other than
prior austenite grain size on the room temperature properties.

After heat treatments (which were carried out in air), decarburized layers
were removed by chemically etching the quenched samples in 2% nital for times
of up to 3 hrs. Typically a thickness of ~0.08 mm. of material was removed
which is greater than the depth of decarburized material which results from
heat treatment.

Compression stress-strain curves were obtained using an Instron testing
machine and an initial true strain rate of $4.4 \times 10^{-4} \text{sec}^{-1}$. Homogeneous de-
formation of the specimens was achieved using a teflon film lubricant. The
specimens were periodically removed during testing to measure dimensional
changes and the usual chart recording of load versus crosshead extension was
also obtained.

A true stress-true strain plot (from actual specimen measurements) is
shown in Figure 12 for a 1.3%C steel in the 850°C → 750°C → W.Q. → LN_2Q..
condition*. The high fracture strength of 630 ksi obtained in this steel,

* Since final fracture often fragments the samples, the exact strain at
fracture is not always known and in these cases the value e_p is calculated
from a chart recording of the load - crosshead displacement or by an extra-
polation of the load-measured specimen extensions.
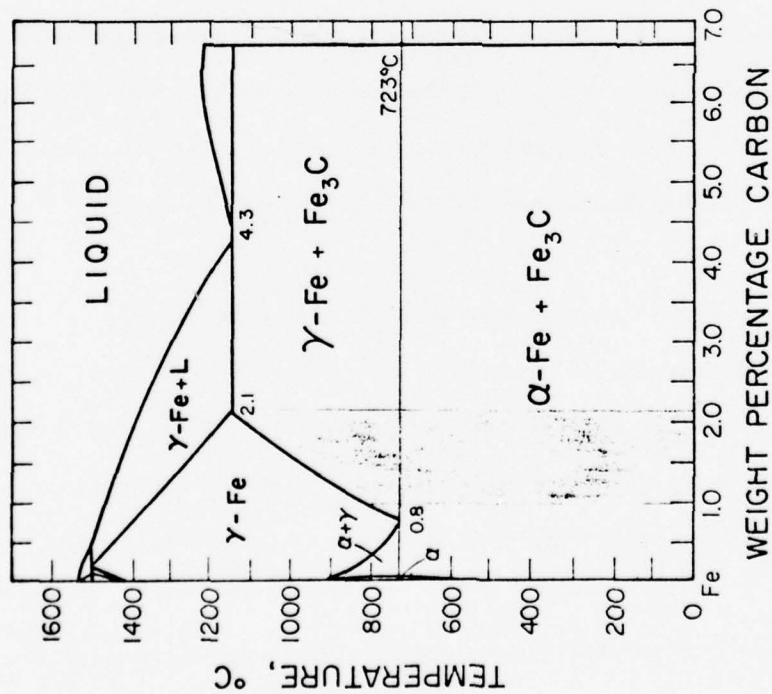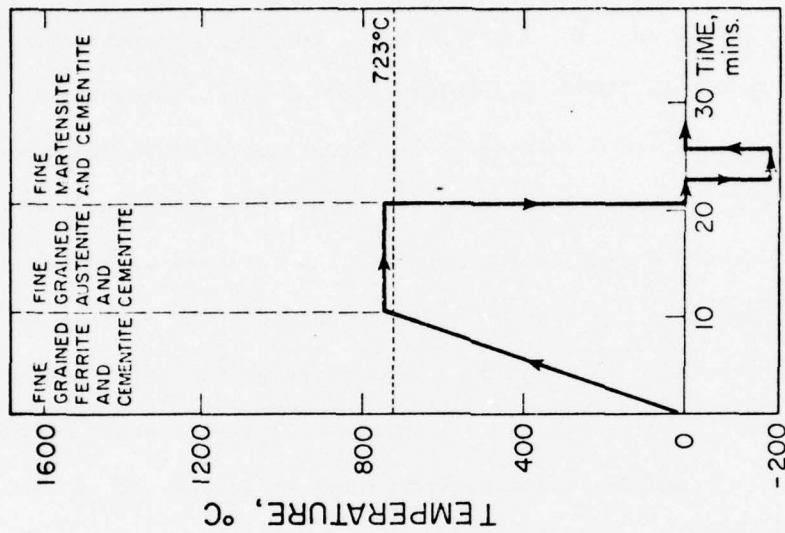
Figure 11. The shaded region in the iron-carbon phase diagram shown above depicts the region of ultrahigh carbon steel. Such steels can be processed to possess fine ferrite grains. The diagram on the right depicts the heat treating procedure used in this investigation to obtain ultrafine martensite by heating to just above the A₁ temperature followed by quenching in ice-water solution followed by liquid nitrogen quenching.
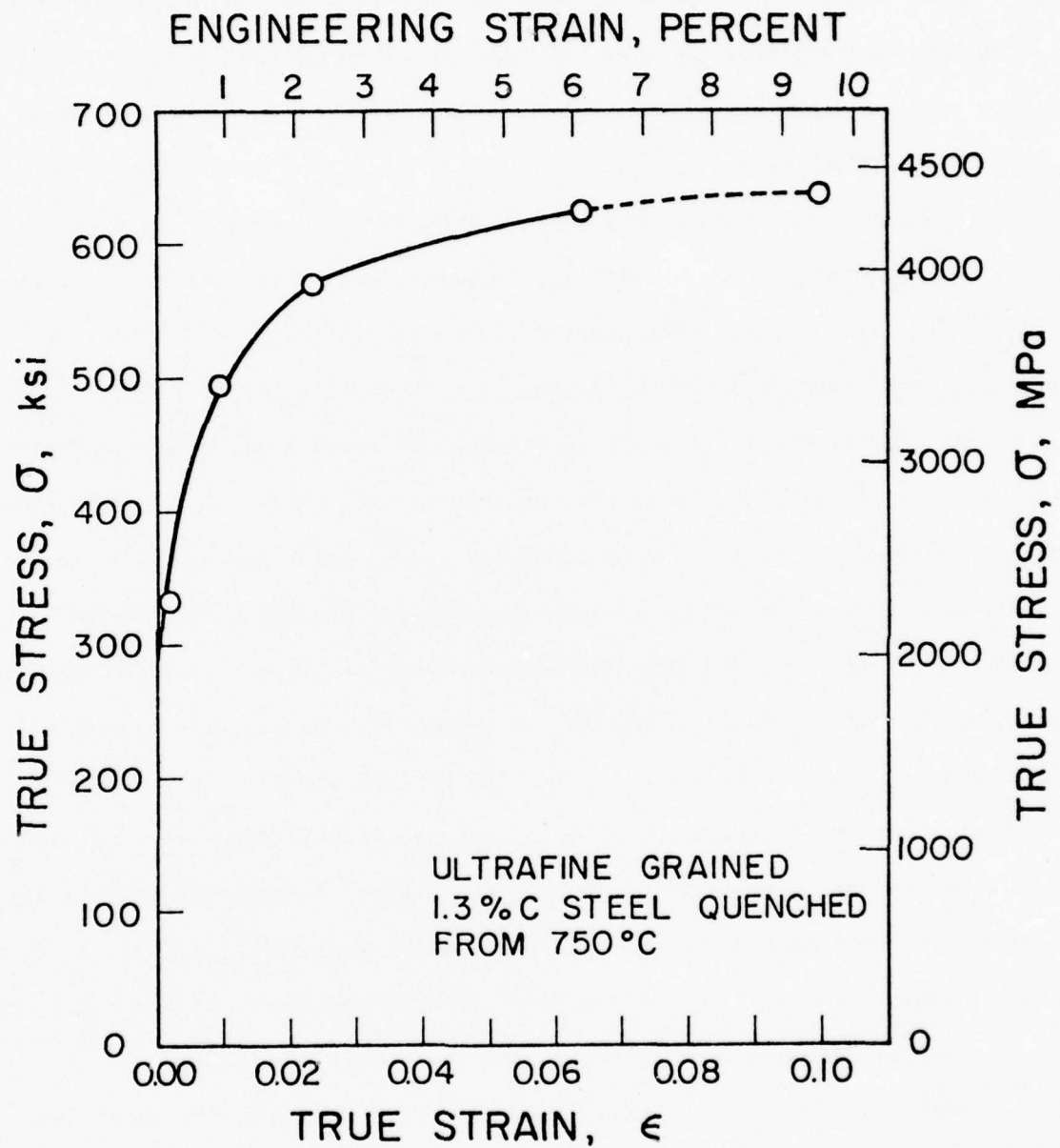
Figure 12. True stress-true strain curve for 1.3%C steel quenched from 750°C tested in compression at room temperature. Note the large fracture strain obtained in compression.

together with the large accompanying fracture strain ($\varepsilon \approx 0.10$) is typical of

the behavior of our low temperature annealed and quenched ultrahigh carbon steels.

Hardness measurements were carried out on a Kentrall hardness testing

machine using a Rockwell 'C' indentor and the arithmetic mean of four values

was used as a final value.

In Figure 13 the relationship between compression fracture strength and

hardness as a function of austenitizing temperature is shown for both steels.

The fracture strength after austenitizing at 1150°C (σ_f = 338 ksi) is

about half the fracture strength of that after austenitizing at 750°C

($\sigma_f \approx 600$ ksi) for the 1.6%C steel confirming the lucid prediction made by

Sauveur. This is in contrast to the hardness results where the austenitizing

temperature does not have a strong influence. A two-step austenitized sample

of 1.3%C steel was deformed to a compression stress exceeding 600 ksi without

fracturing (Figure 2). The large permanent deformation observed after testing

(a true strain of about 0.10)suggests the possibility of making ultra-hard

martensite with some ductility in these fine grained steels. One possible

explanation for the decrease in fracture strength with increase in austenitizing

temperature is the increase in martensite plate size (a parameter that is likely

to be directly proportional to the prior austenite grain size). This hypothesis

is given some credence by the microstructures shown in Figure 14 where the plate

size is seen to increase with increasing austenitizing temperature.

At 750°C the structure of these steels consists of cementite particles

in an austenite matrix of composition about 0.9%C which, upon quenching, should

form martensite. The structure of the 1.6%C steel in the 750°C austenitized

condition is of especial interest since martensite is not observed in the

usual needle-like form (Figure 14Λ). We are currently designating such

structures as "quasi - martensite". The strength of these 750°C quenched
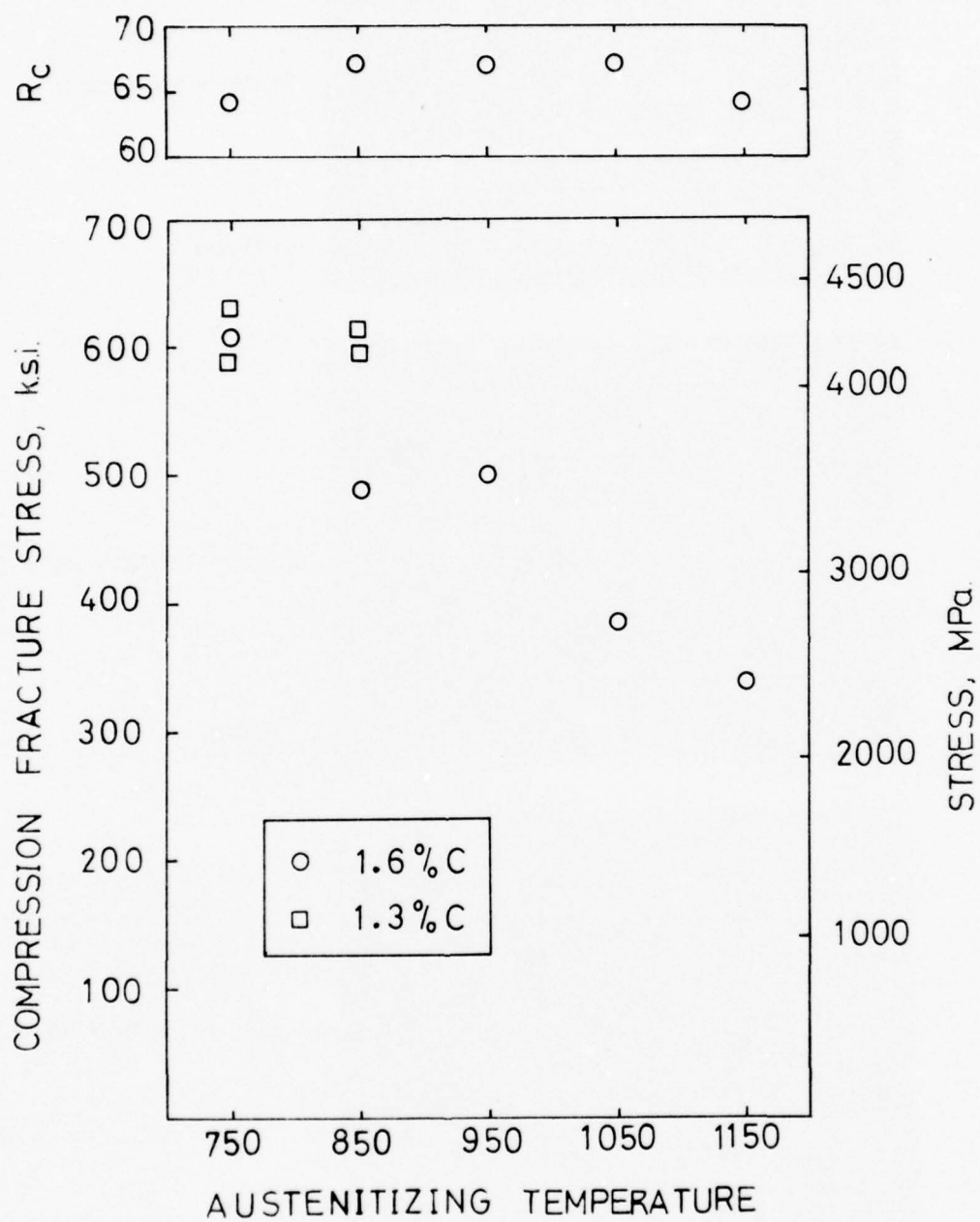
Figure 13. Influence of austenitizing temperature on compression fracture strength and hardness of quenched 1.3%C and 1.6%C steels.
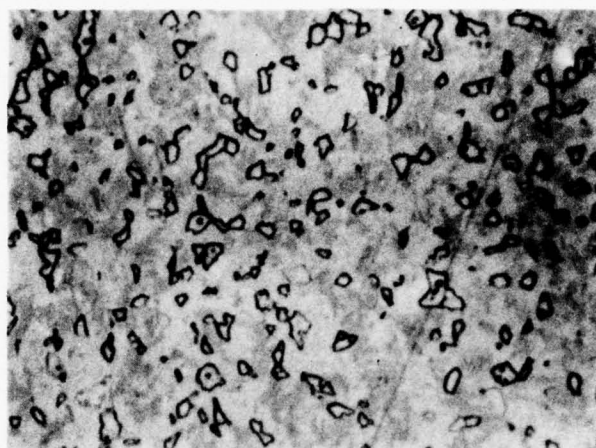
750°C → WQ → LN$_2$Q

10 μm
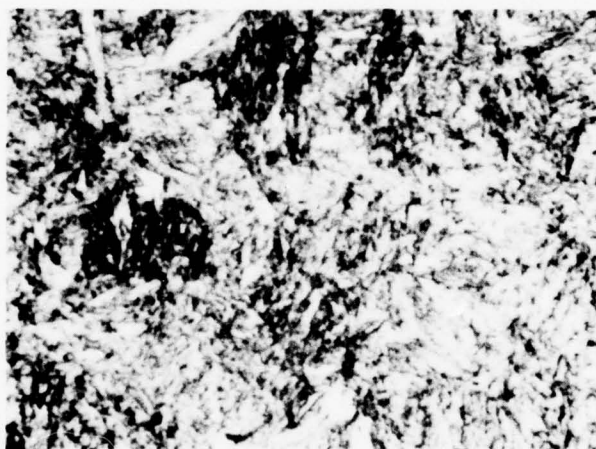
850°C → 750°C → WQ → LN$_2$Q

10 μm

1150°C → 750°C → WQ → LN$_2$Q

10 μm

Figure 14. Development of microstructure with increasing two-step austenitizing temperature for 1.6%C steel. Note the absence of the normally expected needle-like martensite structure in the sample quenched from 750°C.

-33-

samples are most impressive (σ_f exceeding 600 ksi) and clearly warrant a great deal of further study. It is hoped that electron microscope examination, especially through transmission, will shed light on these complex, particulate-composite microstructures.

It is well known that cycling through the $\gamma + Fe_3C$ region to the $\alpha + Fe_3C$ range can cause a grain refinement. Such tests were described in Section C. Although steels investigated here are already in the fine-grained condition (Table 1), an attempt was made to refine further the grains by repeated cycling between 750°C and liquid nitrogen temperature. In this study, however, it was found that cyclic transformations considerably reduced the compression fracture strengths at room temperature as shown in Figure 15 although the hardness was unaffected. From microstructural observations it is evident that the decrease in fracture strength is caused by an increase in the prior austenite grain size with cycling suggesting that this technique only refines grains that are initially of a sufficiently coarse size.

D) Superplastic Warm Pressing and Densification Kinetics of Ultrahigh Carbon Steel Powders.

   R. Caligiuri

This research is an outgrowth of the superplastic high carbon steels program. The early work showed that high carbon steels (1.0-2.0%C) could be stretched 500% in tension when pulled at slow strain rates and warm temperatures (around 650°C). The key to achieving such unheard of elongations in high carbon steel is achieving an appropriate microstructure; that is, a fine ferrite grain size stabilized by spheroidized cementite particles. Such a microstructure can be realized by appropriate warm rolling operations. For example, a 1.6%C commercial casting is first annealed at 1150°C to place all cementite into solution and then, as it air cools down to 600°C, it is continuously rolled to nucleate cementite in fine particle form. The material is then isothermally

-34-
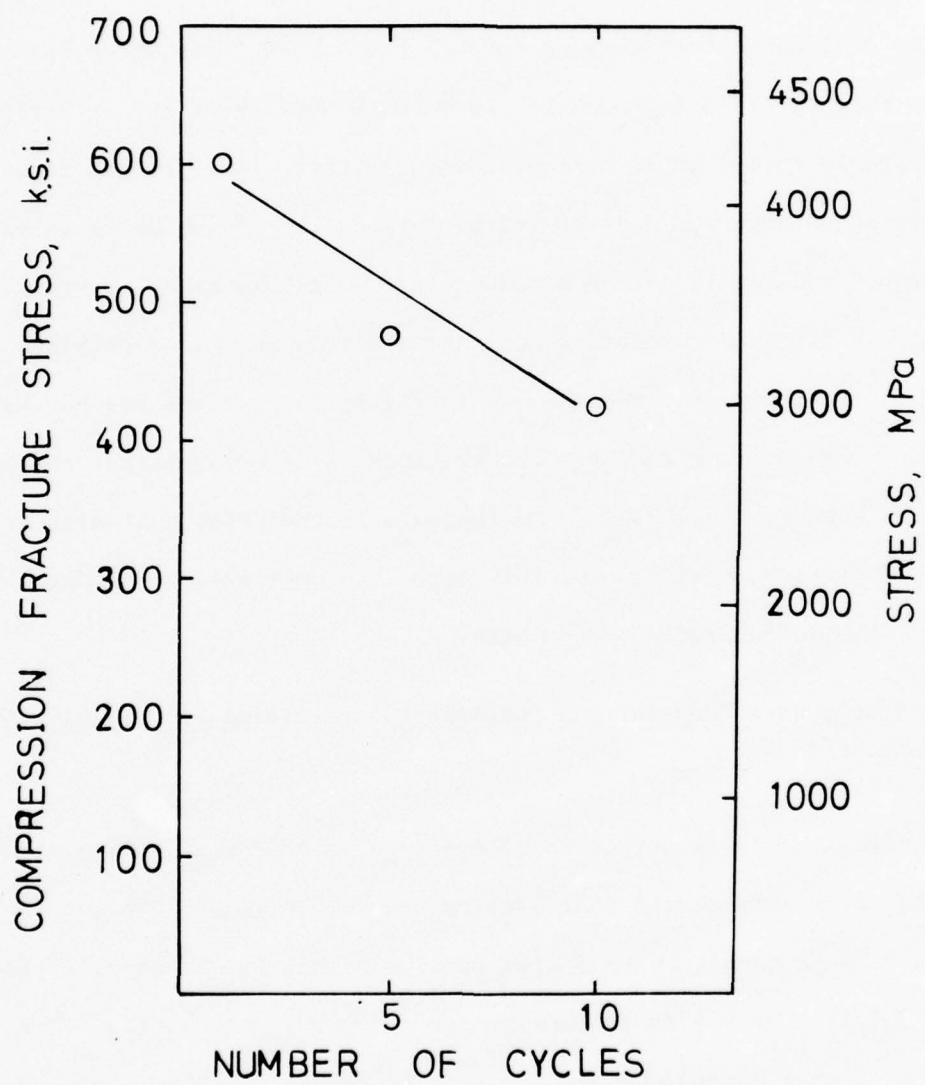
Figure 15. Influence of cyclic transformations on compression fracture strength in 1.6%C steel.

rolled at 650°C to refine the ferrite grain size. The final microstructure
thus consists of fine ferrite grains surrounded by small cementite particles.

The initial purpose of this research was to investigate the possibility
of using P/M techniques to produce the required fine structure as an alternative
to the rolling procedure. That is, liquid atomized high carbon steel powders,
which contain a fine needlelike martensitic structure due to the rapid cooling,
are heated to about 650°C. The fine martensite transforms to fine ferrite and
the cementite precipitates out at the grain boudaries. The powders are then
hot pressed to produce solid material. This technique not only produces a
superplastic material, but also offers the advantages of P/M (less machining,
lower costs, etc.). This portion of the research is proving to be very
successful, showing that superplastic high carbon steel can be produced by
hot pressing liquid atomized powders.

A second major aim of this research was to determine if these superplastic
structures in the powders enhanced the densification process itself. That is,
could fine structure powder reach higher densities than coarse structure powders
when compacted under identical conditions of temperature and pressure? Or, put
another way, could fine structure powders be compacted to high densities at much
lower pressures and temperatures than noramlly used? The answer is yes: 1.6%C
steel powders containing a fine structure reached densities of 95% of the
theoretical density when pressed at 650°C and 10,000 psi. Powders identical
in every way except that they contained a coarse structure reached only 85% of
the theoretical density when pressed at 650°C and 10,000 psi. These results
are illustrated in Figure 16. This led to the development of what we term a
"superplastic warm pressing technique" (pressing of powders at temperatures
around $0.5T_m$).

The above work raises the question: why do fine structure powders densify
more readily? Investigation of this question forms the core of this research.

-36-
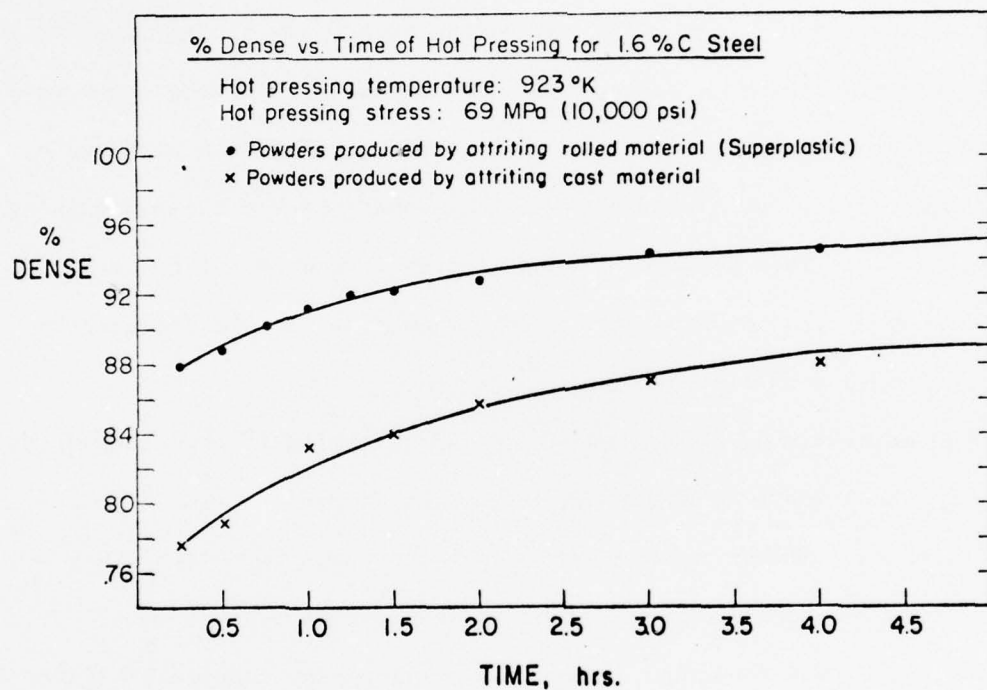
Figure 16. Density-time curves for the 1.6%C fine structure powders and 1.6%C coarse structure powders when compacted at 10,000 psi and 650°C. Both sets of powders were produced by attriting bulk material. The fine structure powders were obtained by attriting a superplastic warm rolled product and the coarse structure powders were obtained by attriting the original coarse grained casting. Both sets of powders were attrited identically and both had the same initial relative density. It is clear from this plot that the internal microstructure of the fine structure powders is enhancing the densification kinetics.

Experimental equipment was set up which enabled us to plot instantaneous density as a function of time. In this manner we were able to calculate densification rates as a function of density, compacting stress, and temperature. Compactions were first done on commercial grade iron powder and the densification rates thus calculated were compared to steady state creep rates determined from compression tests carried out on fully dense material. The correlation as shown in Figure 17 is quite remarkable. The densification rates ($\dot{\rho}$) gave a stress exponent and activation energy equal to the values determined from steady state creep tests: namely, n = 4.5 and Q = 60 kcal/mole. These values are the same as the values normally associated with slip creep through dislocation climb. These results led to the development of a phenomenological equation which predicts that the densification rate is directly proportional to the steady state creep rate. That is, the mechanisms which control steady state creep also control the warm compaction of metal powders. The proportionality constant is predicted to be a function of the current density, which we verified experimentally.

If this phenomenological prediction is correct, then grain boundary sliding, which is thought to be the deformation mechanism operative during superplastic flow, should control the densification of fine structure powders. Densification rates calculated from the warm pressing of high carbon steel fine structure powders should give a stress exponent of about two and an activation energy of about 40 kcal/mole, values normally associated with superplastic flow. Compaction of 1.74%C liquid atomized powders at warm temperatures gave these values as shown in Figure 18a. Thus it appears that the high carbon steel fine structure powders are densifying by a grain boundary sliding mechanism, and this is why they densify much more readily than coarse structure powders. Furthermore, steady state creep tests performed on fully dense 1.74%C material at warm temperatures also gave stress exponents of about two and activation energies of 40 kcal/mole in the low strain rate regime as shown in Figure 18b. This lends further

-38-
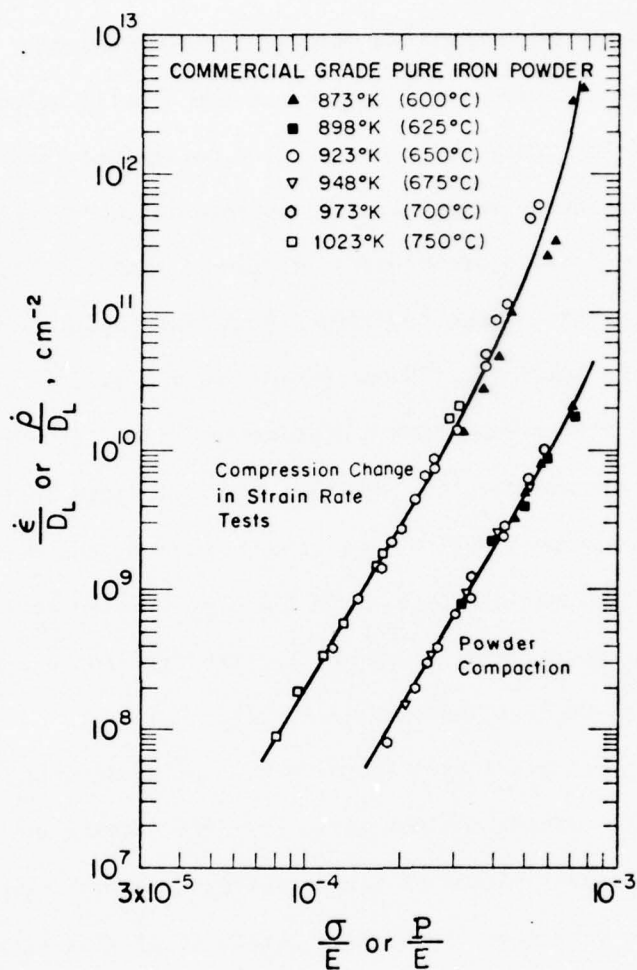
Figure 17. Plot of steady state creep rate ($\dot{\epsilon}$) or densification rate ($\dot{\rho}$) at a density of 85% compensated by the lattice diffusivity of iron against the true flow stress or applied pressure compensated by elastic modulus. The fact that creep tests and powder compaction tests at all temperatures fall on the distinct lines suggests D_L contains the correct temperature dependence. Both the creep tests and the compaction tests exhibit the same power law stress dependence with a slope of about 4.5. These results suggest that there is a proportionality between the steady state creep rate and the densification rate.
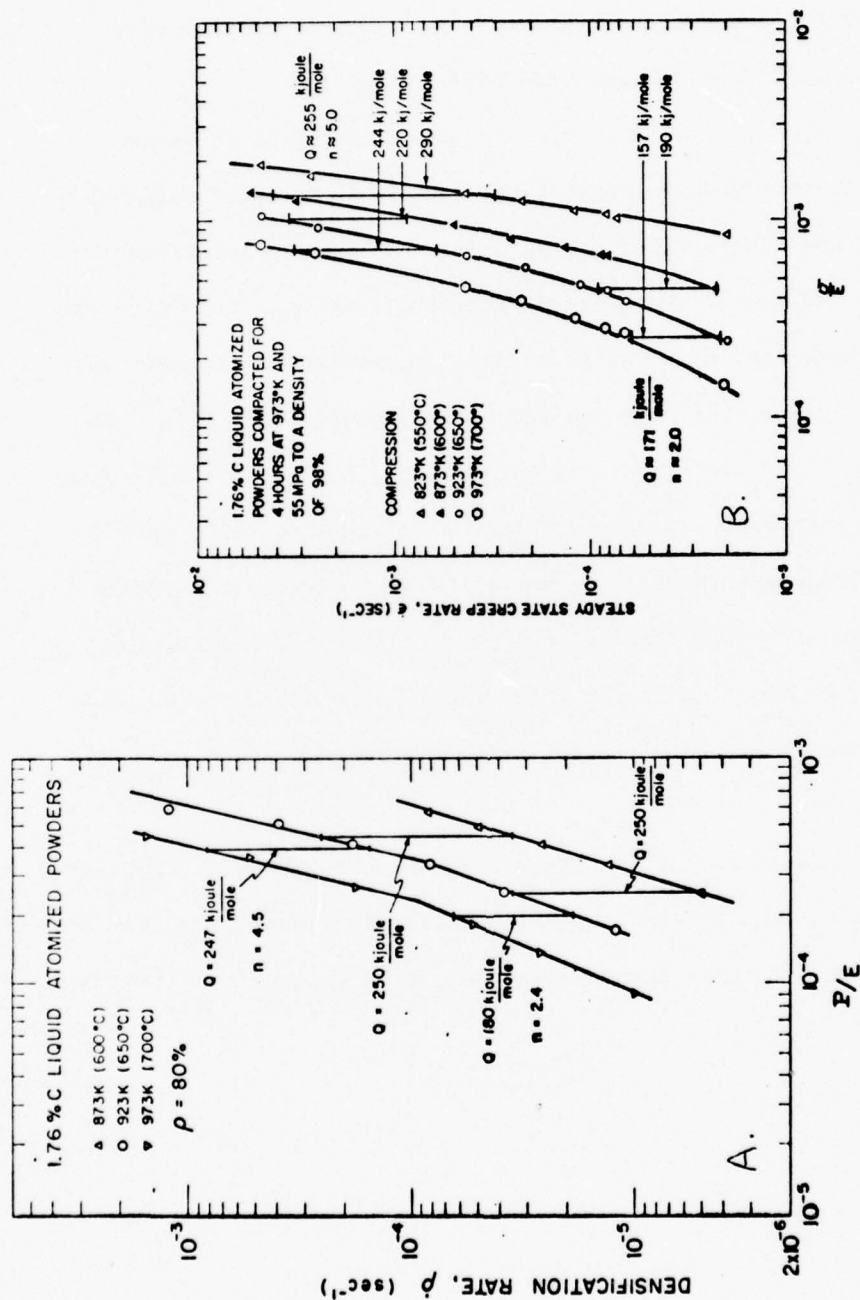
Figure 18. Densification and creep studies on 1.76%C liquid atomized powders. a) gives the log ρ̇-log P plots at various temperatures at a density of 80%. There is a change in slope and activation energy with increasing P/E at 700°C and 650°C. b) shows the creep data(as obtained by change in strain rate compression tests) on fully dense 1.76%C material. A change in slope and activation energy is also observed with increasing σ/E. In both cases, the stress exponent (slope changes from 2 to 5 and the activation energy from 40 kcal/mole to 60 kcal/mole. These data suggest that ρ̇ is also proportional to ε̇ for fine structure powders.

credibility to the phenomenological equation and suggests that bulk superplastic material can be produced by powder metallurgy methods. Similar results were achieved with studies on 1.22%C liquid atomized powders.

It is possible that the difference in density shown in Figure 16 is due simply to a difference in steady state creep rate: the fine structure material creeps much faster than the coarse structure material. Since the densification rate is proportional to the steady state creep rate, the fine structure material will therefore densify much faster. To circumvent this problem the powders must be compacted at a stress where they have the same steady state creep rate. As shown in Figure 19a, the 1.6%C fine structure material and the commercially pure iron material have the same steady state creep rate at a stress of 6250 psi. Furthermore, the plots intersect in a regime where the fine structure material is superplastic. The results of compacting both materials in powder form at 6250 psi is shown in Figure 19b. Again the fine structure powders are 10% more dense, suggesting that the proportionality coefficient between $\dot{\rho}$ and $\dot{\varepsilon}$ is mechanism dependent.

Finally, it might be noted that this research is one of the few attempts at correlating steady state creep data with powder consolidation data. Most researchers still attempt to fit their hot pressing data to a viscous type flow model.
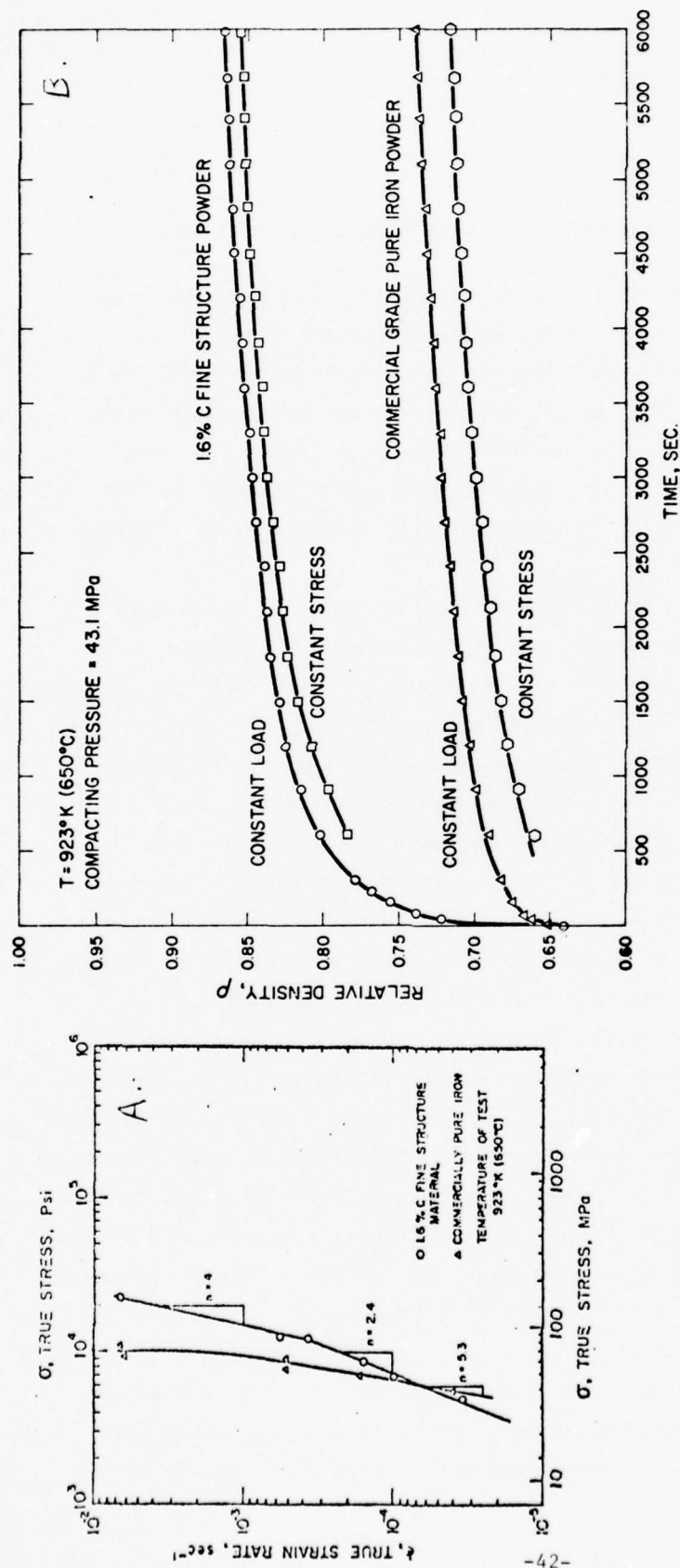
Figure 19. In a), the $\log \dot{\varepsilon} - \log \sigma$ behavior for the fully dense commercial grade pure iron material and for the fully dense 1.6%C fine structure material are shown. The two curves intersect at a stress of 6250 psi in the region where the fine structure material behaves superplastically. At 6250 psi and 650°C both materials exhibit the same steady state creep rate but creep by different mechanisms. b) shows the results of compacting these materials in powder form (screened to the same size range of 70-100μm) at 6250 psi and 650°C. Both sets of powders densified with the same initial density of about 64%. Compactions were done both under constant load conditions and under constant pressure conditions (correcting for the change in pressure due to the increase in density). In either case the result is the same - the 1.6%C fine structure powders are about 10% more dense thant the iron powders. This suggests that the relationship between σ and $\dot{\varepsilon}$ is mechanism dependent in such a way that superplastic 1.6%C fine structure material will densify much more readily than non-superplastic pure iron material.

E) Superplasticity in Metals and Alloys

O. D. Sherby

Presented at ARPA Workshop, La Jolla, California, July 14, 1976

The term superplasticity has been used to describe extraordinary elonga-
tions (several hundred percent) obtained during tensile deformation of poly-
crystalline materials. Although superplasticity was first observed over 50
years ago (Rosenhain, Haughton, Bingham 1920), active research in this field
began after Underwood's review paper on superplasticity in 1962. The term
superplasticity originates from the Russian word "Sverhplastichnost" (ultra
plasticity) first described by Bochvar when he studied the mechanical behavior
of aluminum-zinc alloys.

Considerable effort has been devoted to studies of superplastic metals
and alloys since 1962. This high research activity centers on attempts to
understand this type of plastic behavior and on attempts to put such unusual
characteristics to practical use in metal forming operations.

There are basically two different approaches to analyzing superplastic
behavior of materials. One approach is through applied mechanics. This
method emphasizes the importance of understanding nonuniform plastic flow
and the factors influencing the progression of a neck during tensile deforma-
tion. Factors such as strain rate sensitivity and strain hardening rate are
central to explaining the amount of ductility that can be attained in a given
material. This method points out clearly why superplastic materials are
invariably highly strain-rate sensitive. The other approach to analyzing
superplasticity is through materials science. Here, one attempts to understand
the structural features that are needed to obtain high strain rate sensitivity.
Two types of superplastic flow have been observed: internal stress superplasticity
and fine structure superplasticity. Internal stress superplasticity refers to
the extensive elongations that occur in certain metallic alloys under conditions
where high internal stresses occur concurrent with deformation. Fine structure
superplasticity refers to the extensive elongations that occur in metallic
alloys in which a fine grain structure exists. Most of the investigations
on the two types of superplasticity is described in recent reviews. (Chaudhari
1967, Sherby 1969, Burke and Weiss 1970, Johnson 1970, Davies, Edington, Cutler
and Padmanabhan 1970, Nicholson 1972, Mukherjee 1975, Alden 1975, Shorshorov
et al. 1973, Gittus, 1975)

In the following pages we outline the applied mechanics and materials science approach to studying superplasticity. Emphasis will be placed on fine structure superplasticity. The factors influencing this type of super-plasticity are now fairly well documented. This knowledge, coupled with advances made in understanding normal plastic flow in crystalline solids (slip creep), permits us to outline methods for enhancing and optimizing superplasticity in materials.

I. APPLIED MECHANICS ASPECTS OF SUPERPLASTICITY

As implied earlier all superplastic materials have one key characteristic in common - their resistance to plastic flow is a strong function of the strain rate. That is, they are highly strain rate sensitive. Phenomenologically, this can be seen in the following graph. Although high rate sensitivity is a necessary condition for superplasticity, it is not a sufficient one. Special structural changes occurring during plastic flow, such as internal cracking at interphase boundaries, cavitation or grain boundary separation can lead to premature failure.

Fig. 1
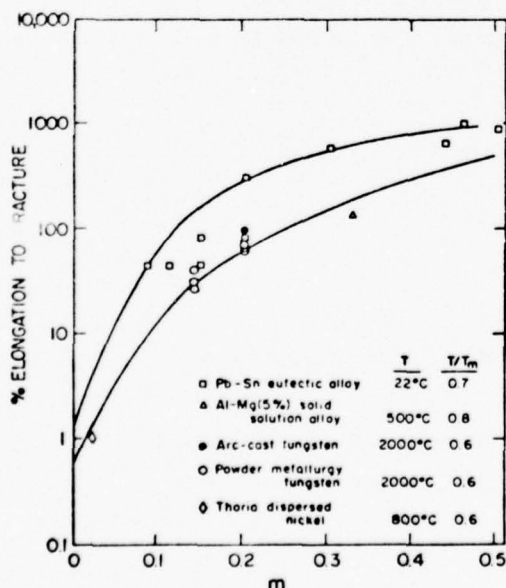
Metals and alloys show high strain rate sensitivity at high temperatures. This rate sensitivity is usually measured by the exponent m in the phenomenological equation $\sigma = K\dot{\varepsilon}^m$. The adjoining figure shows that the ductility (measured by elongation to fracture) increases as the strain rate sensitivity exponent increases. Superplastic metals and alloys generally exhibit strain rate sensitivity exponent (m) values in the range $m \simeq 0.5$ (0.4 to 0.6).

(Data from Avery and Backofen, 1965, Mullendore and Grant, 1954, Conway and Flagalla, 1969, Green 1959, Wilcox and Clauer, 1966).

The applied mechanics approach to explaining high plasticity can be best given by the following example. The true strain rate is given by $\dot{\varepsilon} = \frac{dl}{l\,dt} = -\frac{dA}{A\,dt}$. Thus, $\frac{dA}{dt} = -\dot{\varepsilon}A$. But $\dot{\varepsilon} = K\sigma^{1/m} = K\left(\frac{F}{A}\right)^{1/m}$ where F is the applied force. Substituting this expression, one obtains

$\frac{dA}{dt} = K'\left(\frac{1}{A^{1/m-1}}\right)$ where $K' = -KF^{1/m}$. This expression gives the rate change in area as a function of the area. For values of m less than unity, the magnitude of $\frac{dA}{dt}$ increases as A decreases (an expected result). However, as m approaches unity $\frac{dA}{dt}$ becomes a diminishing function of A and at m = 1, $\frac{dA}{dt} \neq f(A)$. The later result explains why Newtonian fluids (such as glass, well masticated chewing gum, molasses, etc.) have such high plasticity.
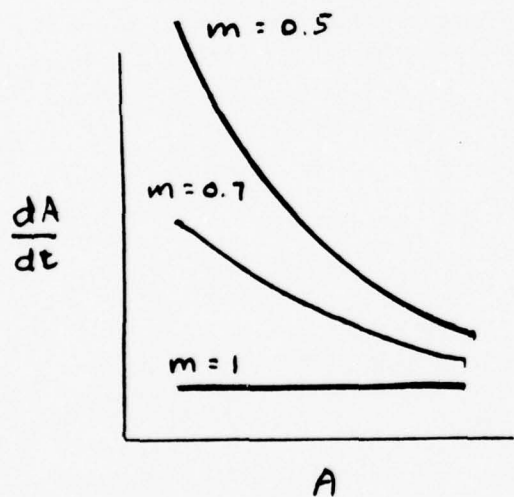
Schematic showing the change of $\frac{dA}{dt}$ with A for various values of m.

There are other theories based on mechanics that have been developed to describe ductility. Four of these are outlined below:

(a) Rossard (1966) has shown that the strain at the start of necking is given by $\varepsilon_{neck} = \frac{N}{1-2m}$, where N is the strain hardening exponent in $\sigma = K\varepsilon^N$. His theory would predict infinity plasticity at m = 0.5!!

-45-

(b) Morrison (1968) showed that the dimensions of the sample will dictate the total elongation observed and showed that

$$\% \text{ elongation to fracture} = bm^2 \left(\frac{do}{Lo}\right) \times 100$$

where b is a material constant, and do and Lo are the diameter and length of sample respectively.

(c) Avery and Stuart (1968) took into account the possible tapered shape of the sample. Their equation is given as

$$\% \text{ elongation} = \left\{ \left[\frac{1-\beta^{1/m}}{1-\alpha^{1/m}} \right]^m -1 \right\} \times 100$$

where α is the ratio of the minimum to maximum area at the start of the test and β is the same ratio at some arbitrary stage of the test at which the elongation is measured.

(d) Burke and Nix (1975), using a finite element approach, showed that the

$$\% \text{ elongation} = \left[\exp \left(\frac{2n}{1-m} \right) -1 \right] \times 100.$$

Fig. 2
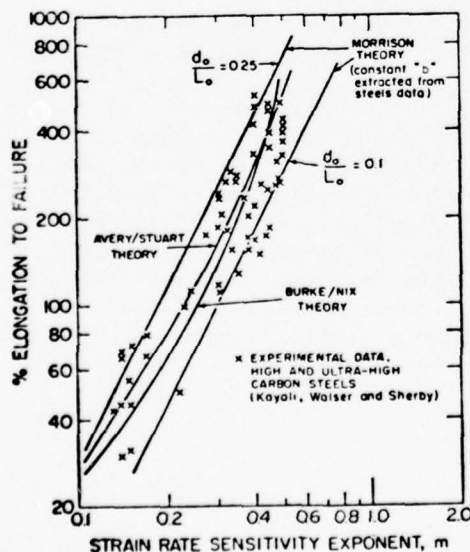
The predicted elongation to fracture is shown as a function of the strain rate sensitivity exponent, m, based on various analytical expressions (using applied mechanics arguments). The curves predicted by the Morrison relation were calculated using b = 100.

(Data from Walser and Sherby, 1975 and Kayali, 1976).

II. MATERIALS SCIENCE ASPECTS OF SUPERPLASTICITY

(a) Internal Stress Superplasticity

Fig. 3
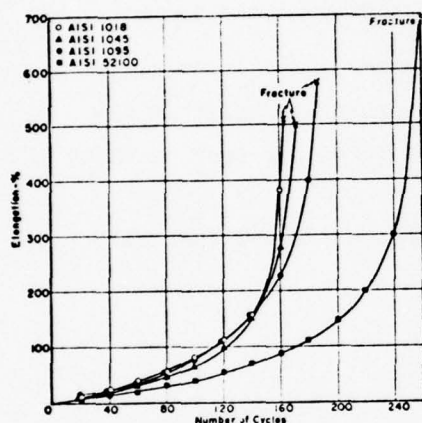
The adjoining graph illustrates internal stress superplasticity, through multiple phase transformations, in several steels. As can be seen the influence of thermal cycling through the phase transformation temperature yields high elongations to fracture for several steels. The applied stress was 2500 psi. (Data from Oelschlagel and Weiss, 1966).

Fig. 4
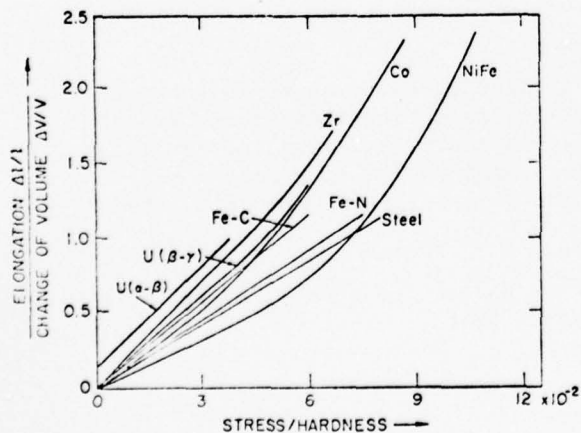
The adjoining graph illustrates that the strain obtained upon transformation can be written as

$$(\varepsilon_{transf.}) = K \left(\frac{\Delta V}{V}\right) \frac{\sigma}{\text{Hardness}}$$

Thus the transformation strain is seen to be approximately a linear function of the applied stress. Furthermore, it is seen to be proportional to the volume change upon transformation (a measure of internal stress) and inversely proportional to the hardness (a measure of creep strength without internal stress). (Data from de Jong and Rathenau, 1961, Johnson and Greenwood 1962, Greenwood and Johnson 1965, Chubb, 1955).

Fig. 5

◇ (◆) LOBB, SYKES and JOHNSON
○ ROBINSON et al, 653°C
△   "   604°C
□   "   554°C

$\frac{\dot{\epsilon}}{D_{AVE}}$ (cm^{-2})

ISOTHERMAL TESTS

THERMALLY CYCLED
(450 ⇌ 600°C)
$\frac{\sigma}{E} = \frac{\sigma_{applied}}{E}$

THERMALLY CYCLED
(450 ⇌ 600°C)
$\left(\frac{\sigma}{E} = \frac{\sigma_{applied} + \sigma_{internal}}{E}\right)$

5

1

$\frac{\sigma_i}{E} = 1.5 \times 10^{-4}$

$\frac{\sigma}{E}$
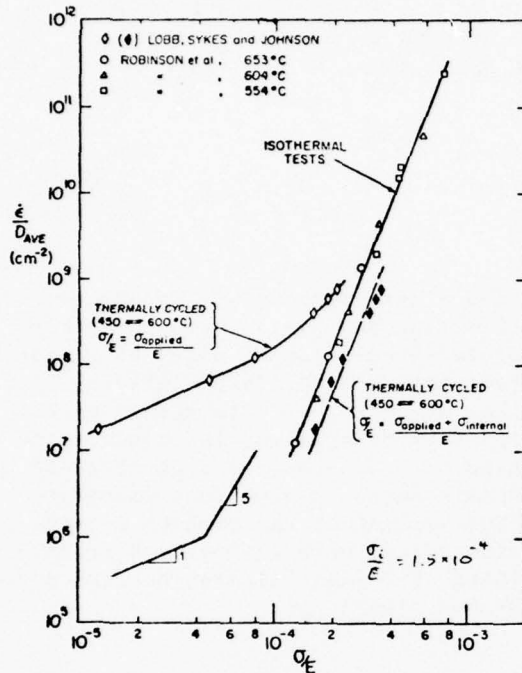
The adjoining graph illustrates internal stress superplasticity, through thermal cycling, in alpha uranium. The data are plotted as diffusion compensated creep rate versus modulus compensated flow stress. The high internal stress generated under thermal cycling leads to a high strain sensitive material (m ≃ 1 as can be seen in the figure). If the diffusion compensated creep rate is replotted as a function of $\left(\frac{\sigma + \sigma_i}{E}\right)$ where σ_i is the (proposed) internal stress then the data exhibits the normal power dependence observed in alpha uranium tested under isothermal conditions (n = 5 in the relation $\dot{\epsilon} = K\sigma^n$. [The high internal stress generated during thermal cycling arises from the high anisotropy of thermal expansion observed in alpha uranium; $\alpha_{[100]}$ is 60 x 10^{-6} per °C and $\alpha_{[100]}$ is - 18 x 10^{-6} per °C at 500°C].

Data of Lobb, Sykes and Johnson, 1972,
Robinson, Armstrong and Sherby, 1972,
Adda and Kirianenko, 1962
Armstrong, Eash and Hockett, 1972

Fig. 6

α - URANIUM

ISOTHERMAL
TENSILE TEST, 600°C (50% elong.)

UNDEFORMED SAMPLE

THERMALLY CYCLED
(450 - 600°C) (>500% elong.)
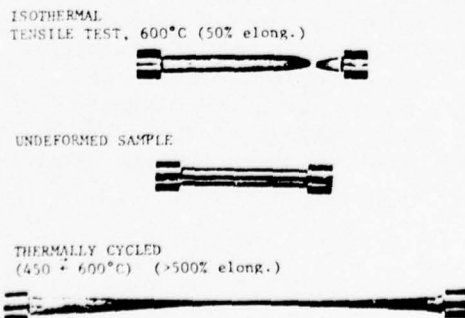
Thermal cycling of alpha uranium leads to a high strain rate sensitive material. This high strain rate sensitivity is manifested in high ductility as can be seen by the specimen at the bottom of the adjoining figure. Whereas creep deformation occurring under isothermal conditions leads to 50% elongation at 600°C, thermal cycling between 450° - 600°C leads to creep elongations exceeding 500%.
(Lobb, Sykes and Johnson, 1972)

(b) Fine Structure Superplasticity

A dominating feature of materials that exhibit fine structure superplasticity is that they have a fine grain size. Typically grains in the order of one to five microns are required in order to observe superplastic effects at reasonable strain rates. In contrast most technological materials have grain sizes in the order of 50 to 200 microns (.05 to .2mm).

Fig. 7
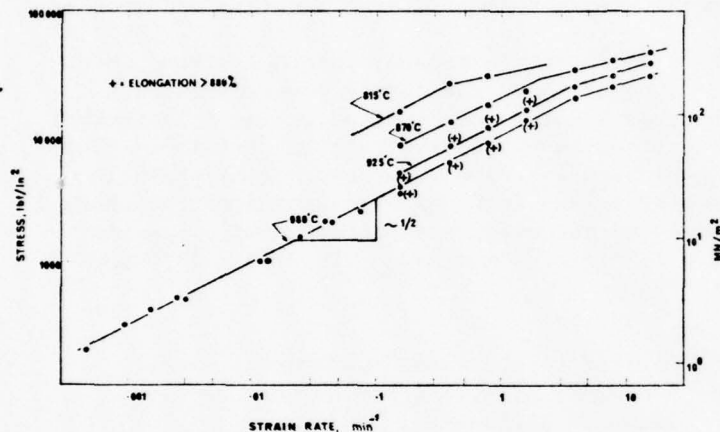
Flow stress-strain rate relationship (log-log plot) for a two phase nickel-iron-chromium alloy at elevated temperatures (39%Cr-10%Fe-1.75Ti-1%Al balance Ni). The strain rate sensitivity exponent is constant and high ($m \simeq 0.5$) over a wide range of strain rate. Elongations exceeding 880% (extent of the machine travel elongation) were commonly observed. [Data of Hayden, Gibson, Merrick and Brophy, 1967]

Fig. 8
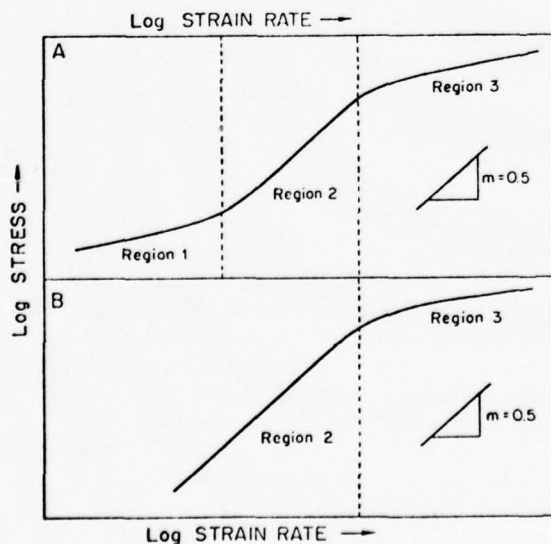
Many superplastic materials exhibit an S shaped behavior when plotted as logarithm of the flow stress versus logarithm of the strain rate (shown as A in the diagram at left). Each of the three regions (making up the S shaped curve) are often associated with specific mechanisms of plastic flow. Other materials exhibit only two regions, as shown in schematic diagram B; an example of this type of behavior is shown above for the nickel-chromium-iron alloy.

-49-

Fig. 9
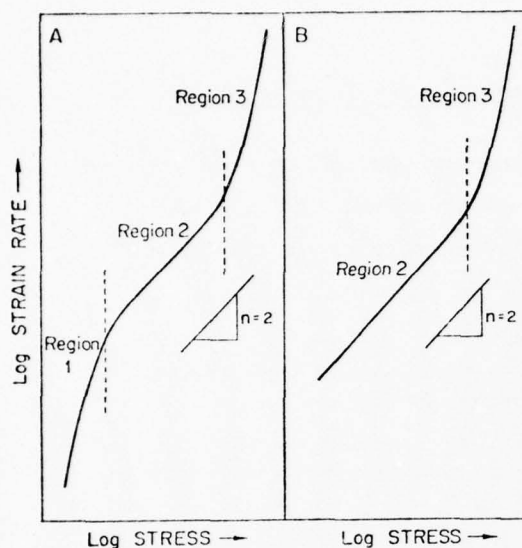
The data of Figure 8 is sometimes plotted as logarithm of strain rate as a function of the logarithm of the flow stress. The slope of such a plot yields the stress exponent n in the equation $\dot{\varepsilon} = K\sigma^n$. The value of n is equal to the reciprocal of m. Superplastic flow of fine grained materials, given as region 2 in the graph, is generally associated with a stress exponent of 2 (that is, m = 0.5)

Region 3, the high stress region, is generally associated with a slip creep (dislocation) mechanism. Some of the considerations given to region 2 and 1 are described below.

Microstructural Characteristics of Superplastic Deformation

Microstructural investigations on superplasticity revealed that the small grains associated with superplastic deformation (region 2) remain equiaxed and grain boundaries are smooth and curved. (Packer and Sherby 1967, Alden 1967, Alden and Schadler 1968, Dingley 1970). Few dislocations are observed in the grains and no subgrain boundaries are formed. (Hayden, Gibson, Merrick and Brophy 1967, Dunlop and Taplin 1971, Nicholson 1972). Slip lines are not seen on polished surfaces (Dingley 1970, and Geckinli 1973) and extensive grain boundary sliding and grain rotation are observed indirectly by displacements of surface scratches (Holt 1968, Lee 1969) and directly during deformation in the scanning electron microscope (Dingley 1970, Geckinli 1973). It is, therefore, generally believed that the deformation in region 2 is associated with grain boundary sliding.

There is very little experimental data available for region 1. However, it has been reported that there is less grain boundary sliding in region 1 than in region 2 (Holt 1968) and some evidence of grain elongation (Holt and Backofen 1966). In accord with observations of this type, Hart (1967a) and Alden (1969) suggested that dislocation climb may control the deformation rate in region 1. Ashby and Verrall (1973) consider that region 1 is associated with a threshold stress (involving grain boundary tension), developed a theory to explain the sigmoidal shape observed. Rai and Grant (1975) consider that grain growth of the very fine grains during high temperature deformation will lead to an increase in strength and will result in region 1; thus, they conclude that it is a false region associated with grain growth. Conflicting data exist with respect to evidence for region 1 based on studies in the same system. For example, Mohamed and Langdon (1975) show sigmoidal behavior of the type depicted in Figure 8 for creep of monotectoid composition Al-Zn; on the other hand, Vaidya, Murty and Dorn (1973) and Misro and Mukherjee (1972) show no region 1, and in fact, show m increasing in region 1 approaching m values of unity which they attribute to Coble creep. Although there is controversy on the interpretation of region 1 we believe it is likely associated with a strengthening effect from grain growth and not with a grain boundary tension threshold stress effect.

-50-

<u>Summary of conditions, including microstructural aspects, for fine structure superplasticity.</u>

In addition to the requirement that fine grains are needed for fine structure superplasticity, it appears that a number of other prerequisites usually need to be fulfilled. We list the following as a guide to obtaining maximum superplasticity:

(1) ultrafine grain size (typically 1 to 5μm)

(2) usually a two phase material is required. The purpose of the second phase is to prevent grain growth of the matrix phase.

(3) Second phase should have about the same strength as matrix phase. If the second phase is much stronger than matrix phase cracks may form at interphase boundary (e.g. alumina in copper).

(4) $T \simeq 0.4$ to $0.7T_m$. If above $0.7T_m$, grain growth can occur, minimizing superplastic effect. If below $0.4T_m$, dislocation mechanisms may dominate plastic flow leading to non-superplastic behavior.

(5) $\dot{\varepsilon}$ is typically low ($\dot{\varepsilon} = 10^{-6}$ to 10^{-4} sec^{-1})

(6) m should be high (0.4 to 0.6)

(7) the grain boundaries should be high angle (disordered) boundaries. See example for eutectoid composition steel given below.

(8) grain boundaries should be mobile (minimize stress concentration) and should not be prone to ready tensile separation (e.g. polycrystalline ceramics).

(9) equiaxed grains.

When a eutectoid composition steel is warm worked a fine structure of ferrite grains and cementite particles is developed. The ferrite grain boundaries, however, consist of a mixture of high and low angle boundaries. Such a material is not superplastic; the m values are typically about 0.3 and only 100% elongation is obtained. If the steel is cold worked and recrystallized, high angle boundaries are obtained and the material is superplastic (m = 0.5 and elongations exceeding 400% are readily achieved).
(from Kayali, 1976)

Fig. 10

-51-
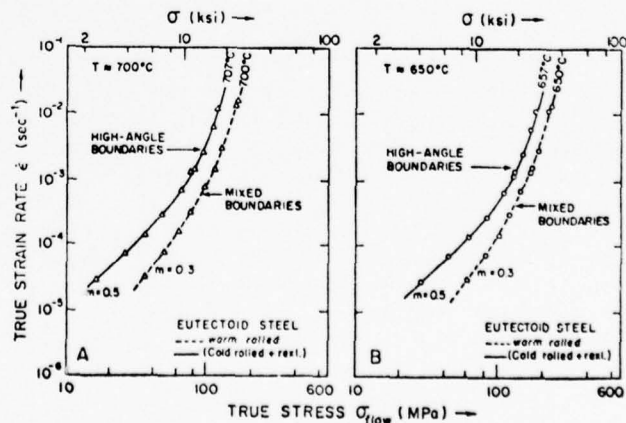
Fig. 11
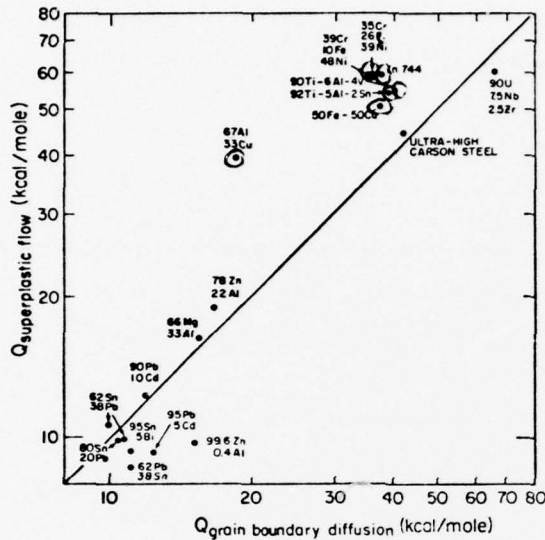
The data given on the left illustrate that the activation energy for superplastic flow of many fine structure materials is equal to the activation energy for grain boundary diffusion. As can be seen, some fine structure materials, (given by open symbols), however, exhibit an activation energy for superplastic flow which is higher than that for grain boundary diffusion suggesting that lattice diffusion may be controlling the plastic flow process in these cases (Data from White, 1976).

Phenomenological equations for superplastic flow and for slip creep flow.

Data from various investigators suggest that the creep rate of many fine structure superplastic materials obey the following constitutive relation:

$$\dot{\varepsilon} = 10^8 \frac{D_{gb} \cdot b}{L^3} \left(\frac{\sigma}{E}\right)^2 \tag{1}$$

Here, D_{gb} is the grain boundary diffusion coefficient, b is burgers vector. L is the grain size, σ is the flow stress and E is the elastic modulus.

Since some superplastic materials exhibit activation energies for plastic flow that are nearly equal to those for lattice diffusion (see Figure 11 above), it is tempting to suggest that an effective diffusion coefficient should be used to correlate all the superplasticity data. Thus,

$$D_{eff} = D_L f_L + D_{gb} f_{gb} \tag{2a}$$

-52-

where f_L and f_{gb} are the fraction of atoms associated with the lattice and grain boundary respectively. f_L is about unity and f_{gb} is equal to $\frac{\pi w}{L}$ where w is the grain boundary width. Equation (2a) can thus be rewritten as

$$D_{eff} = D_L + D_{gb}\frac{\pi w}{L} \tag{2b}$$

If the concept of an effective diffusion coefficient is valid then equation (1) and (2) can be combined to yield

$$\dot{\varepsilon} = \frac{10^8}{\pi}\frac{D_{eff}}{L^2}\left(\frac{b}{w}\right)\left(\frac{\sigma}{E}\right)^2 \tag{3}$$

We have found equation (3) to fit virtually all of the fine-structure superplasticity data provided the grain boundary width is assumed to be a function of the melting temperature of the material [namely $w \propto (T_m)^{-2}$] which is not an unreasonable assumption.

The use of equation (1) with the known constitutive relation for plastic flow by slip creep permits us to determine the various factors that can be utilized to optimize the range of stress, strain rate and temperature over which superplastic mechanisms will dominate the plastic flow process.

The constitutive equation for slip creep is given as

$$\dot{\varepsilon} = \frac{K}{\alpha^5}\frac{D_L}{b^2}\left(\sinh \alpha \frac{\sigma}{E}\right)^5 \tag{4}$$

where α is a constant about equal to the reciprocal of the value of σ/E where power law breakdown occurs. K is a constant equal to 10^{11} for many bcc and fcc meterials with high stacking fault energies; it is also a function of stacking fault energy and of texture (especially with hcp materials).

In the following we illustrate how we can use equation (1) and (4) to enhance the range where superplastic flow predominates.

Fig. 12
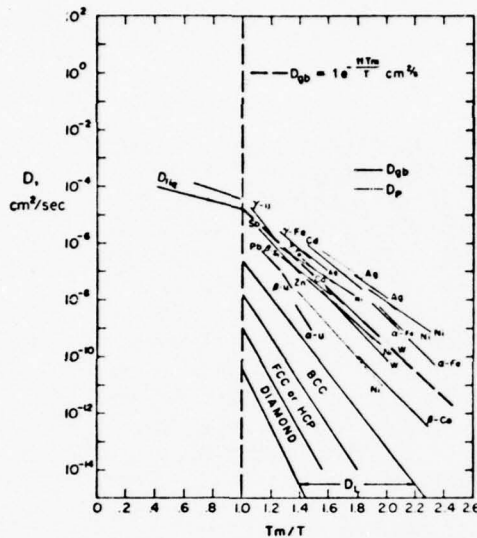
The grain boundary diffusion coefficient for various metals is plotted as a function of the reciprocal homologous temperature. It can be seen that D_{gb} is uniquely a function of the absolute melting temperature, T_m, and can be described by the equation

$$D_{gb} = 1 \exp - \frac{11 T_m}{T} \text{ (in cm}^2/\text{sec)}.$$

The lattice diffusion coefficient, D_L, on the other hand, is a function of crystal structure as well as of T_m.
(Data from Bly, 1973)

Fig. 13
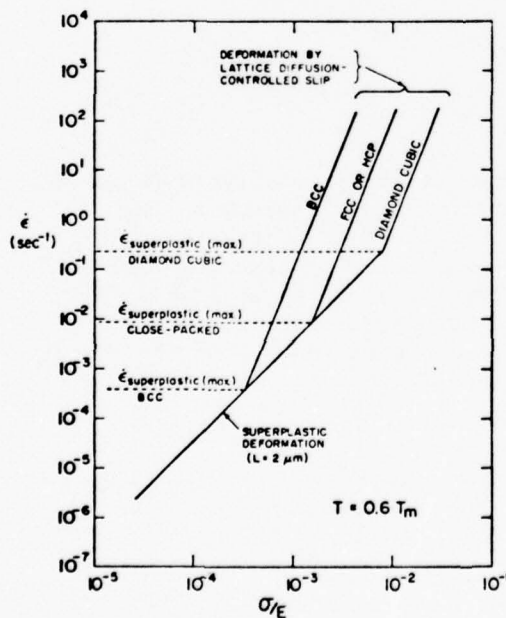
Crystal structure can influence the extent of superplastic flow since $\dot{\epsilon}$ slip creep is a function of crystal structure (equation 4) where as $\dot{\epsilon}$ superplastic is not for many materials (equation 1). The correlation shown was made at $T = 0.6 T_m$ and for a grain size of 2 μm.

Fig. 14
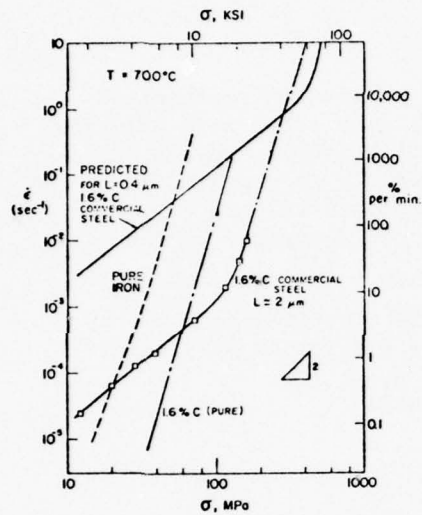
Grain size is the most important single factor influencing the range of superplastic flow since $\dot{\varepsilon}$ superplastic is proportional to L^{-3} (equation 1) whereas $\dot{\varepsilon}$ slip creep is not a function of grain size. The graph on the left illustrates the strain rate-flow stress relationship for a 1.6%C steel at 700°C. For a grain size of $L = 2\mu m$ superplastic flow is expected up to a strain rate of 10% per minute; if the grain size is decreased to 0.4μm superplastic flow can be expected to occur up to strain rates as high as 5000% per minute. (Data of Walser and Sherby, 1975)

Fig. 15
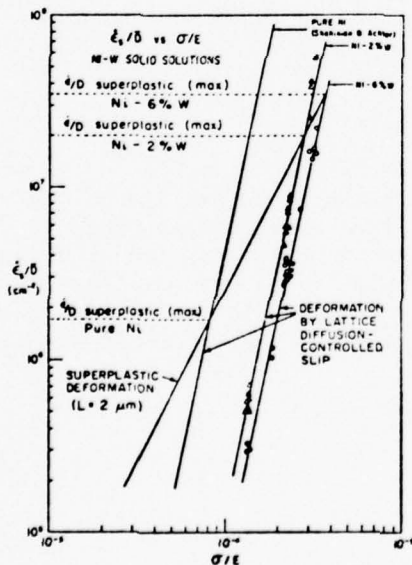
Tungsten enhances the creep resistance of nickel in the slip creep region by decreasing the stacking fault energy. On the other hand, $\dot{\varepsilon}$ superplastic is unaffected by stacking fault energy. Thus, the extent of superplastic flow may be broadened by solute additions which decrease the stacking fault energy of the matrix. (Data from Johnson, Barrett and Nix, 1972)

Fig. 16
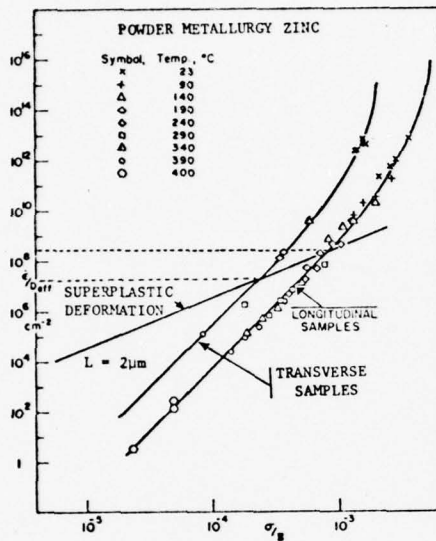
Texture can be an important variable in influencing the creep rate in the slip creep region. This is shown for textured polycrystalline zinc which exhibits large differences in creep rates when tested in a longitudinal and transverse sense. If superplastic flow is not affected by texture then the extent of superplastic flow can be altered by this variable.
(Data from Edwards, McNelley and Sherby, 1974)

Fig. 17
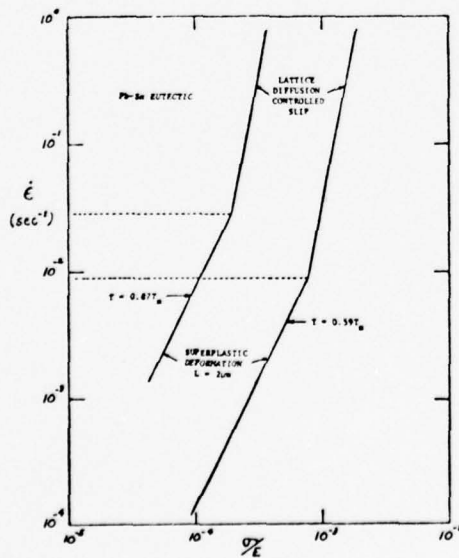
D_{gb} is less strongly influenced by temperature than D_L (Figure 12). Thus, temperature will influence $\dot{\varepsilon}$ superplastic in a different way from $\dot{\varepsilon}$ slip creep. Increasing the temperature will increase the strain rate for maximum superplastic flow but will decrease the stress range over which high plasticity can be expected.

REFERENCES

Adda, Y. and Kirianenko, A., 1962, J. Nuc. Mat., 6, 130

Alden, T. H., 1967, Acta Met., 15, 469.

Alden, T. H., 1968, ASM Trans. Quart., 61, 559.

Alden, T. H., 1969, J. Aust. Inst. Metals, 14, 207.

Alden, T. H., 1975, in Treatise on Materials Science and Technology, Vol. 6, ed. R. J. Arsenault, Academic Press, New York, p. 225.

Armstrong, P. E., Eash, D. T. and Hockett, J. E., 1972, J. Nuc. Mat., 45, 211

Ashby, M. F., and Verrall, R. A., 1973, Acta Met., 21, 149.

Avery, D. H., and Stuart, J. M. 1968, in Surfaces and Interfaces II, Physical and Mechanical Properties, ed. J. J. Burke, N. L. Reed and V. Weiss, Syracuse University Press, Syracuse, New York, p. 371.

Bly, D., Ph. D. Dissertation, Department of Materials Science and Engineering, Stanford University, 1973

Bochvar, A. A. and Seiderskaya, Z. A., Izvestia Acad. Nauk, USSR, OTN, 1945, 9, 821.

Burke, J. J., and Weiss, V., 1970, Ultrafine Grain Metals, Syracuse University Press, Syracuse, New York.

Burke, M. A., and Nix, W. D., 1975, Acta Met., 23, 793.

Chaudhari, P., 1967, Acta Met., 15, 1777.

Chubb, W., 1955, Trans. AIME, 203, 189.

Conway, J. B. and Flagella, P. N., 1969, Creep-Rupture Data for the Refractory Metals to High Tempertures, Nuclear Systems Programs Technical Report GEMP-685 [R-69-NSP-9], General Electric Company

Davies, G. J., Edington, J. W., Cutler, C. P., and Padmanabhan, K. A., 1970, J. Mater. Sci., 5, 1091.

de Jong, M., and Rathenau, G. W., 1961, Acta Met., 9, 714.

Dingley, D. J., 1970, in Proc. of the 3rd Annual Scanning Electron Microscope Symposium, Chicago, p. 329.

Dunlop, G. L., and Taplin, D. M. R., 1972, J. Mater. Sci., 7, 84.

Edwards, G. R., McNelley, T. R., and Sherby, O. D., 1974, Scripta Met., 8, 475

REFERENCES (contd)

Geckinli, A. E., 1973, Ph.D. Thesis, Dept. of Materials Science, Stanford
     University, Stanford, California.

Gittus, John, Creep, Viscoelasticity and Creep Fracture in Solids
(Chapter II), Applied Science Publishers Ltd., London, 1975, 509.

Green, W., 1959, Trans. AIME, 215, 1057

Greenwood, G. W. and Johnson, R. H., 1965, Proc. Roy. Soc., A283
403.

Hart, E. W., 1967a, Acta Met., 15, 1545.

Hayden, G. W., Gibson, R. C., Merrick, H. F., and Brophy, J. H.,
     1967, Trans. ASM, 60, 3.

Holt, D. L., 1968, Trans. AIME, 242, 25.

Holt, D. L., and Backofen, W. A., 1966, ASM Trans. Quart., 59, 755.

Johnson, R. H., 1970, Met. Rev., 15, 115.

Johnson, R. H. and Greenwood, C. W., 1962, Nature, 195, 138.

Johnson, W. R., Barrett, C. R., and Nix, W. D., 1972,
Met. Trans., 3, 963

Kayali, E. S., Ph. D. Dissertation, Department of Materials
Science and Engineering, Stanford University, 1976

Lee, D., 1969, Acta Met., 17, 1057.

Lobb, R. C., Sykes, E. C. and Johnson, R. H., 1972,
Met. Sci. J., 6, 33

Misro, S. C., and Mukherjee, A. K., 1972, in Proceeding of John Dorn
     Memorial Symposium. Amer. Soc. Metals, Metals Park, Ohio (to
     be published).

Mohamed, F. A., and Langdon, T. G., 1975, Acta Met., 23, 117.

Morrison, W. B., 1968, Trans. ASM, 61, 423.

Mukherjee, A. K., 1975, in Treatise on Materials Science and Technology,
     Vol. 6, ed. R. J. Arsenault, Academic Press, New York, p. 163.

Mullendore, A. W. and Grant, N. J., 1954, Trans. AIME,
200, 973

Nicholson, R. B., 1972, in Electron Microscopy and the Structure of
     Materials, ed. G. Thomas, R. M. Fulrath, and R. M. Fisher, Univ.
     of California Press, Berkeley, p. 689.

Oelschlagel, D. and Weiss, V., 1966, Transactions ASM, 59, 143.

REFERENCES (contd)

Packer, C. M., and Sherby, O. D., 1967, Trans. ASM, 60, 21.

Rai, G., and Grant, N. J., 1975, Met. Trans., 6A, 385.

Robinson, S. L., Armstrong, P. F. and Sherby, O. D., 1972,
J. Nuc. Mat.,46, 293

Rosenhain, W., Haughton, J. L., and Bingham, K. E., 1920, Journal
    Inst. of Metals, 23, 261.

Rossard C., 1966, Rev.Met., 63, 225

Sherby, O. D., 1969, Science Journal, 5, 75.

Shorshorov, M. H., Tichonov, A. S., Bulat, C. I., Gurov, K. P.,
Nadirashvili, N. I. and Antipov, V. Z., Superplasticity in Metallic
Materials, Uzdatelsvo, "Nauk", Moscow, 1973.

Stewart, M. J., 1976, Met. Trans., 7A, 399

Underwood, E. E., 1962, J. Metals, 914, 919.

Vaidya, M. L., Murty, L. K., and Dorn, J. E., 1973, Acta Met., 21,
    1615.

Walser, B., and Sherby, O. D., 1975, Second Annual Progress Report to
    Advanced Research Projects Agency, Center for Materials Research,
    Stanford University, Stanford, California.

White, R., Ph. D. Dissertation, Department of Materials
Science and Engineering, Stanford University, 1976

Wilcox, B. A., and Clauer, A. H., 1966, Trans. AIME,
236, 570

IV. SYNTHESIS OF NEW TYPES
OF CATALYST MATERIALS

J. P. Collman
Professor of Chemistry

and

M. Boudart
Professor of Chemical Engineering
and Chemistry

A.   Synthesis of New Types of Catalyst Materials;

"Face-to-Face Porphyrins"

James P. Collman

1. Introduction

The reductions of O_2 to H_2O_2 or H_2O, and N_2 to N_2H_4, are multielectron reductions of exceptional scientific and economic interest. Because sequential single electron reductions of O_2 or N_2 produce energetically unfavorable intermediates, rapid and reversible reaction will require direct multielectron reduction. Such reduction should be facilitated by simultaneous action of two or more metal sites. It has recently been our goal to synthesize binuclear systems with well defined distances between the metal sites, and test this hypothesis.

In the previous technical report[1], we outlined several possible approaches to so-called "face-to-face" porphyrins, and discussed results obtained from the first prototype ligand 1 which we refer to as the "clamshell" porphyrin. In this report,

1
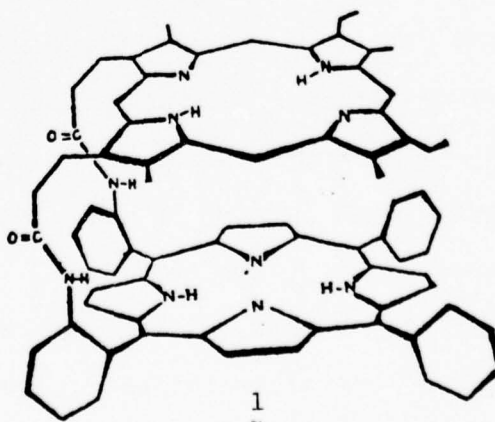
Figure 1

we will describe further ESR and electrochemical work on 1,
including results which have led to the cessation of work on this
compound. We will then go on to report the synthesis,
characterization and preliminary study of two related, but more
sophisticated binuclear ligands, including the first true "face-
to-face" porphyrin.

2.   ESR Studies on Metal Derivatives of Clamshell Porphyrin (1)

a. Cu(clamshell)

Further ESR investigations into the previously observed
metal-metal interactions exhibited by Cu(clamshell) reveal they
are intermolecular in origin. This was demonstrated by a dilution
study where the [Cu(clamshell)] in a 30% CH_2Cl_2, 60% toluene,
10% N-MeImidazole solvent was varied from 4.05 x 10^{-3} to 3.69 x
10^{-4} M. Signals at -160°C attributable to metal-metal interactions
decrease in intensity upon dilution. Further, solutions
containing both Cu(TPP) and Cu(mesoPIXDME) at the same concentration
show similar spectra to solutions containing Cu(clamshell) at
the same concentration. By studying separate solutions containing
only Cu(TPP) and Cu(mesoPIXDME) it is found that only the latter
dimerizes in solution.

The species giving rise to metal-metal interactions in the
Cu(clamshell) is a dimer, i.e. {Cu(clamshell)}$_2$. This species
is in equilibrium with the monomer in solution, hence the change
upon dilution. In view of the dimerization tendencies of the

monomeric Cu(II) porphyrins studied, it is likely the
{Cu(clamshell)}$_2$ dimer is associated through the Cu(mesoPIX)
"halves".

ESR signals due to monomeric Cu(clamshell) molecules
exhibit no intramolecular metal-metal interactions. One can
conclude, therefore, that under the conditions employed, the Cu(II)
centers must be at least 8-10 $\overset{\circ}{A}$ apart.

b. Co(clamshell)

The ESR of a Co(clamshell) solution in 40% o-dichloro-
benzene, 60% toluene solvent at -160°C is independent of
concentration. The spectrum does not exhibit features due to
metal-metal interactions, and has the appearance (Table I) of a
four-coordinate Co(II) porphyrin with the unpaired electron
residing in $d_z{}^2$. Solutions containing Co(TPP) and Co(mesoPIXDME)
at equal concentration do not exhibit identical spin Hamiltonian
values (Table I) to those of Co(clamshell) as was the case with
the Cu(II) analogs. Since $d_z{}^2$ contains the unpaired electron in
these four coordinate Co(II) compounds, the ESR is very sensitive
to the immediate environment along the z axis. The small A(Co)
values in Co(clamshell) relative to Co(TPP) and Co(mesoPIXDME) are
indicative of a slightly larger amount of covalency involving
$d_z{}^2$. This extra covalency is likely due to a weak axial inter-
action of each Co(II) in the Co(clamshell) with the porphyrin
π-system of the other "half".

Table I

ESR of Metalloporphyrin and Metalloclamshell
Derivatives at -160°C

Compound[1]	$g_{\parallel}$	$g_{\perp}$	$A_{\parallel}$ (Cu)[4]	$A_{\perp}$ (Cu)[4]
Co(mesoPIXDME)	2.00	2.81	146	223
Co(TPP)	1.99	2.76	142	215
Co(clamshell)	2.02	2.44	103	74

Compound[2]	Base	$\Delta\nu_{\frac{1}{2}}$[3]	$g_{\parallel}$	$g_{\perp}$	$A_{\parallel}$ (Co)[4]	$A_{\perp}$(Co)[4]	$A_{\parallel}$ (^{14}N)[4]
Co(TPP)	N-MeIm	9	2.03	2.30	76	$\geq$10	16.0
Co(mesoPIXDME)	N-MeIm	9	2.03	2.30	75	$\geq$10	16.0
Co(clamshell)	N-MeIm	9	2.03	2.31	75	$\geq$10	16.0
Co(TPP)	pyridine	9	2.03	2.32	77	$\geq$10	15.5
Co(mesoPIXDME)	pyridine	9	2.03	2.32	77	$\geq$10	15.5
Co(clamshell)	pyridine	9	2.03	2.31	78	$\geq$10	15.5
Co(clamshell)[5]	pyrazine	12	2.02	2.31	81	$\geq$10	14.5

[1]Solvent is 60% toluene, 30% CH_2Cl_2, 10% N-MeIm.

[2]Solvent is 60% toluene, 40% o-dichlorobenzene.

[3]$\Delta\nu_{\frac{1}{2}}$ = full width at half height of ΔM_I = 5/2 cobalt hyperfine line in parallel region, ΔM_I = +1 nitrogen line. Units are 10^{-4} cm^{-1}.

[4]Units are 10^{-4} cm^{-1}.

[5][Co(clamshell)] = [pyrazine] = 4.34 x 10^{-3} M.

In the presence of excess axial base, Co(clamshell) forms a 2:1 adduct (one equivalent of base per Co center) similar to the 1:1 Co(TPP) and Co(mesoPIXDME) base complexes. These five coordinate complexes exhibit very similar spin Hamiltonian and linewidth data with a variety of axial bases (Table 1). In the presence of pyrazine where [pyrazine] = [Co(clamshell)], a spectrum is observed where both cobalt centers exhibit five coordinate spectra with one nitrogen donor coordinated axially. Such a result implies pyrazine bridging of two cobalt atoms, though differentiation between inter- or intramolecular bridging cannot be made.

Five coordinate Co(II) clamshell 2:1 base derivatives will react with dioxygen at low temperatures in a manner similar to that of five coordinate monomeric Co(II) porphyrins forming six coordinate paramagnetic dioxygen adducts. Figure 2a shows the ESR spectrum at $-160°$ of $Co(TPP) \cdot py \cdot O_2$. Figure 2b shows the spectrum derived from $Co(clamshell) \cdot (py)_2 \cdot (O_2)_n$. The similar appearance of Figures 2a and 2b, i.e. small g value anisotropy and small A(Co) values suggest each cobalt atom in the Co(clamshell) has bound its own dioxygen. Furthermore, the spectral similarities suggest the unpaired electron in each of the two $Co-O_2$ units resides on the dioxygen moiety as it does in the analogous $Co(TPP) \cdot py \cdot O_2$ complex. A distinguishing feature of Figure 2b is the lack of detailed hyperfine features. Such a

-65-

Figure 2

2a

2b

3200G

3050G

-66-
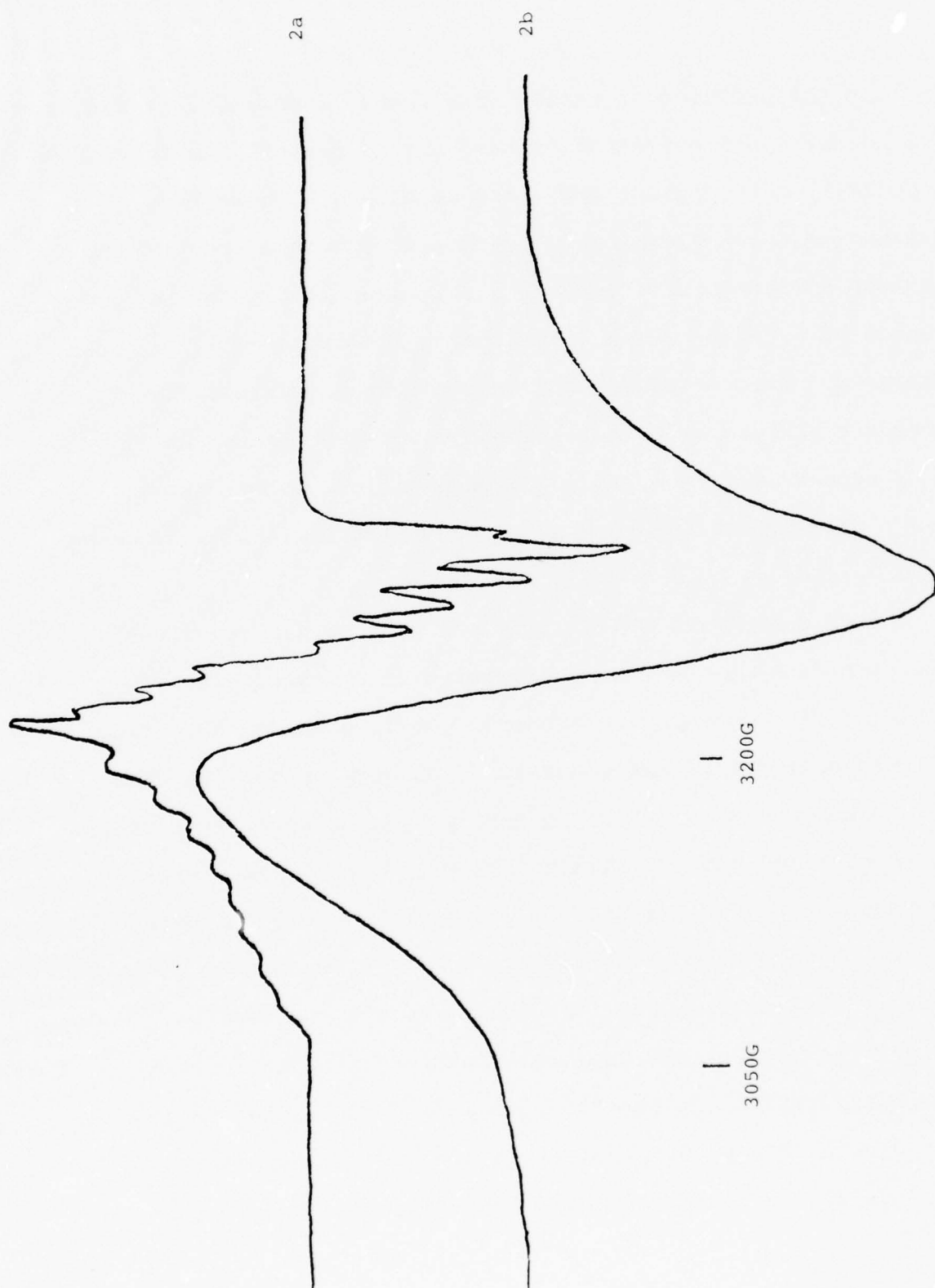
broadening of the ESR signal is not observed in the parent five coordinate $Co(clamshell)\cdot(B)_2$ adducts (see Table 1). A plausible explanation for this behavior is that both dioxygen molecules in the $Co(clamshell)\cdot(B)_2\cdot(O_2)_2$ derivative are coordinated on the "inside", the two base molecules on the "outside" of the clamshell unit, i.e.:
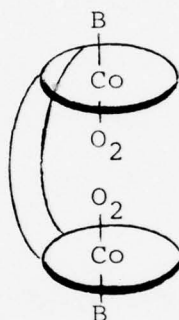
Since the unpaired electron associated with each $Co-O_2$ unit resides on dioxygen, the dipolar electron spin relaxation between the two unpaired electrons is enhanced relative to the five coordinate parent compounds by virtue of the smaller distance separating them.

In summary, the Cu(II) and Co(II) derivatives of the clamshell porphyrin show no metal-metal interactions in the ESR under any conditions. One case, the six-coordinate dioxygen adduct of the Co(II) clamshell, shows a dipolar interaction between the two unpaired electrons. This result suggests the coordinated dioxygen molecules are in close proximity to one another, i.e. coordinated on the "inside" of the clamshell.

3.   Electrochemical Studies on Clamshell Porphyrin (1).

When two or more electroactive centers are chemically bound
to one another it is often possible to observe a mutual influence
on the electrochemical behavior of the centers. This influence
is manifested as a shift in potential of the voltammetric waves
corresponding to reductions or oxidations of the centers.

This shift in potential may come about by either a "through
space" or "through bond" interaction. The observed presence of
potential shifts provides "a priori" qualitative evidence of
electronic interaction.

The metal free clamshell porphyrin (1) and its Co^{+2}
derivative were studied by cyclic voltammetry. The oxidation of
the metal free ligand proved to be too complex for interpretation
because of rapid chemical reactions which follow the production
of the radical cation (a problem which exists with the oxidation
of most o-amidophenylporphyrins). Reduction of the metal free
and Co^{+2} porphyrins, on the other hand, appears to be very straight
forward. In brief, the electrochemical behavior of both free
ligand and Co^{+2} clamshell porphyrin upon reduction appears to be
identical to what is observed in a solution containing an equimolar
mixture of the corresponding monomeric porphyrin halves. No
potential shifts are observed in any case studied.

By employing an optically transparent gold "mini grid" thin
layer electrode, simultaneous visible spectra of various electro-

chemically generated species were obtained. As with the voltammetric experiments, the spectro-electrochemical data proved virtually identical with that obtainable from solutions containing an equimolar mixture of the two independent monomeric halves of the clamshell porphyrin.

In that the two porphyrin halves are joined by two, four-atom, non-conjugated chains, "through bond" electronic interactions would not be expected. On the other hand, if the clamshell existed in solution in the closed "face-to-face" configuration, some observable "through space" interaction should be evident. This is particularly true for the Co^{+2} porphyrin where overlap should exist for the metal d_z2 orbital in addition to the porphyrin π system. The complete lack of any electrochemical evidence for "through space" electronic interaction for any clamshell species suggests that, at least under the conditions employed for the electrochemical experiments, the clamshell and Co^{+2} clamshell porphyrin exist in an "open" configuration.

4. Synthesis of DUC (2), DUFTF (3) and DUAC (4) Porphyrins.

The evidence presented in the previous sections made it clear that a more rigidly held "face-to-face" system would be needed to produce metal-metal interaction. Two compounds suggested by study of CPK molecular models were 2 (DUC, or di-urea clamshell) and 3 (DUFTF, or di-urea face-to-face). Both 2 and 3 were available from the condensation of the corresponding previously reported[1] diamino porphyrins and phosgene.
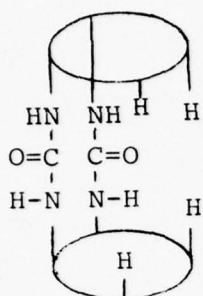
$\underset{\sim}{2}$

DUC
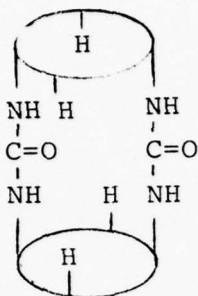
$\underset{\sim}{3}$

DUFTF
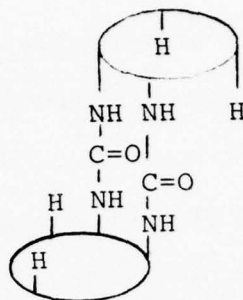
$\underset{\sim}{4}$

DUAC
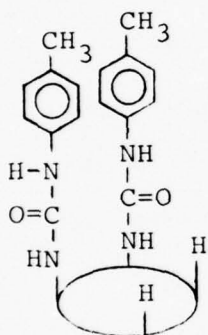
$\underset{\sim}{5}$

DUTM
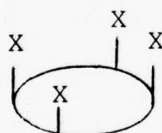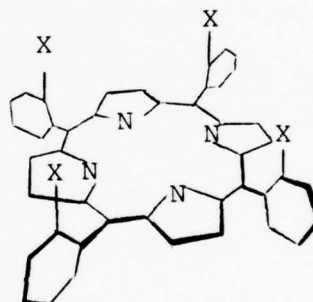
To synthesize $\underset{\sim}{2}$, cis α, β diaminotetraphenylporphyrin is employed as a starting material. Likewise cis α, γ diaminotetraphenylporphyrin is utilized as a starting material to synthesize $\underset{\sim}{3}$.

An amount of the appropriate diaminotetraphenyl porphyrin is initially dissolved in dry oxygen-free benzene containing about 1% pyridine. The solution is treated with a large excess

-70-

of phosgene producing the dicarbamoyl chloride (or diisocyanate). Excess phosgene is removed by distilling the reaction mixture to dryness under vacuum. The dicarbamoyl chloride is then redissolved in benzene--1% pyridine and a benzene solution containing an equimolar amount of diaminotetraphenylporphyrin is added. The reaction is allowed to stir under nitrogen for 12 to 16 hours in order to reach completion. The resulting product is a bisporphyrin bound by two urea linkages.

Only one dimeric porphyrin can form in the case of cis α,γ diaminotetraphenylporphyrin, and experimentally only one major product is obtained, 3. Utilizing cis α,β diaminotetra-phenylporphyrin, however, there are two possible products, 2 and 4. In 4, the diurea anticlamshell (DUAC), the porphyrin halves are not geometrically disposed above one another as in 2. The factor which determines whether 2 or 4 will be produced is the formation of the first of the two urea linkages. There appears to be no preference in the two possible initial reactions as 2 and 4 are produced in approximately equal amounts. In no preparation was there a significant amount of polymeric material formed.

The desired products are separated by column chromatography on TLC grade silica gel, using 2% EtOAc in benzene as the eluent. Compound 2 is stable to light and air, however 3 is rapidly decomposed in solution under similar conditions.

Elemental analyses of 2 and 3 were unsatisfactory.
Difficulty in obtaining satisfactory analyses has been encountered
commonly in porphyrin synthesis, and is probably due to some
combination of tenacious solvation, hygroscopic nature, and
incomplete combustion. In order to help characterize 2 and 3 in
the absence of elemental analysis data, molecular weight and mass
spectral studies were carried out. The molecular weights obtained
for 2 and 3 were 1308 and 1327 respectively (calculated: 1341 for
both 2 and 3). No molecular ion was observed in the mass spectrum
of 2 or 3, but fragments observed for the cleavage of the phenylurea
bonds were as expected[2].

In order to better relate physical properties of these
dimeric porphyrins, a monomer model porphyrin was prepared as
follows. The procedure involving cis α,β diaminotetraphenyl
porphyrin and phosgene was employed as above, however p-toluidine
was added to the dicarbamoyl chloride producing 5 (abbreviated as
DUTM), a model monomeric diaromatic-diurea-tetraphenylporphyrin.

5. Spectroscopic Studies of 2, 3, and 4 and their Co and Cu
Derivatives.

a. Visible Spectra

The symmetric nature of the new porphyrins, 2, 3, and 4,
makes their visible spectra less complicated. Table 2 contains
some pertinent spectral data. Large shifts in the Soret peak
are observed for 2 and 3 relative to 4, 5, and their monomeric

Table 2

Electronic Spectra

Porphyrin	Soret (Å)	Visible (Å)
cis α,β diNH$_2$TPP	422	515, 549, 590, 647
cis α,γ diNH$_2$TPP	422	515, 549, 590, 647
DUTM (5)	422	514, 549, 588, 645
DUAC (4)	417	515, 549, 587, 643
clamshell (1)[2]	422	--
DUC (2)	405	517, 554, 586, 642
DUFTF (3)	407	517, 554, 586, 644
Cu(TPP)	417	537
Cu(clamshell)[2]	417	537
Cu(DUAC)	415	537
Cu(DUC)	412	538
Cu(FTF)	412	538
Co(TPP)	412	528
Co(clamshell)[2]	413	528
Co(DUAC)	411	528
Co(DUC)	408	528
Co(FTF)	408	528

[1] Solvent in all spectra is benzene.

[2] Peak due only to tetraarylporphyrin "half".

predecessors. Soret peaks are known to arise from the $\pi-\pi^*$ transition within the porphyrin moiety. In a configuration where the porphyrins are rigidly held in close proximity (such as in 2 and 3), interactions between these π and π^* orbitals which extend out of the plane of the two porphyrins are possible. It is now evident from the visible spectra that interaction between porphyrin halves in 1 is negligible as the Soret peaks of the two "halves" are unshifted from their respective monomer values.

The Co(II) and Cu(II) derivatives of 2 and 3 also exhibit Soret peak shifts to lower wavelength relative to their monomeric counterparts, though to a smaller extent. Possible metal-metal interactions cannot be assessed by visible spectra as the metal d-d transitions are obscured by the intense visible peaks due to the porphyrin ligands.

B. Nuclear Magnetic Resonance Spectra

NMR spectra of 2 and 3 provide further evidence for the close approach of the two porphyrin halves. In Table 3 are listed the chemical shifts of the internal pyrrole protons in the metal-free porphyrins. In all cases, the resonances lie upfield of TMS due to the ring current associated with the aromatic porphyrin. The monomeric porphyrin chemical shifts lie in the region $\delta-2.5 \rightarrow$ -2.9 depending on solvent. The internal pyrrole protons in 1 due to the TPP "half" occur at $\delta-2.92$, hardly shifted from the value in the corresponding monomer.

Table 3

NMR Chemical Shifts for Internal Pyrrole Protons of Various Monomeric and Dimeric Porphyrins

Porphyrin	Solvent	δN-H	Temp(°C)
cis α, β diNH$_2$TPP	CDCl$_3$	-2.67	25
DUTM	CDCl$_3$	-2.90	25
DUTM	C$_6$D$_6$	-2.50	25
clamshell	CDCl$_3$	-2.92	25
DUC	CDCl$_3$	-4.22	25
DUC	C$_6$D$_6$	-4.80,-6.07	25
		-4.82	60
		-4.35	80
DUFTF	CDCl$_3$	-4.22	25

[1]Chemical shift in PPM relative to TMS.

Similarly, 4 exhibits a resonance shifted little from the monomeric models. The dimers 2 and 3, however, show large upfield shifts due to the added ring current effect of the second porphyrin. In C_6D_6 solution, 2 exhibits a peak splitting at 25°C, which coalesces to a single resonance at higher temperatures. This splitting at lower temperature is likely due to a slow exchange (on the NMR time scale) between chemically distinguishable internal pyrrole sites in this asymmetrically substituted porphyrin.

At this point, NMR chemical shifts of the aromatic and pyrrole regions do not supply further information, as ring current effects due to the second attached porphyrin are at a minimum at these positions. These ring current shifts vary with position as $3\cos^2 \theta - 1$ where θ is the angle between a vector at the center of the porphyrin perpendicular to the plane and a vector joining the position in question with the center of the porphyrin. Crude geometric calculations on a CPK molecular model show $\theta \sim 50°$ for the outer pyrrole hydrogens, consequently $3\cos^2 \theta - 1$ is very small.

c. Electron Spin Resonance

The theory pertaining to the ESR of two coupled $S = \frac{1}{2}$ metals in a dimeric stacked arrangement has already been outlined[1]: Figure 3 shows the ESR at -160°C in a 10% N-MeIm (N-methyl-imidazole), 60% toluene, 30% CH_2Cl_2 solution of Cu(DUAC) (Figure 3a) and Cu(DUC) (Figure 3b). The spectrum and spin

Figure 3

3b

3a

$g_{||}$

|← D →|

2700G   3000G
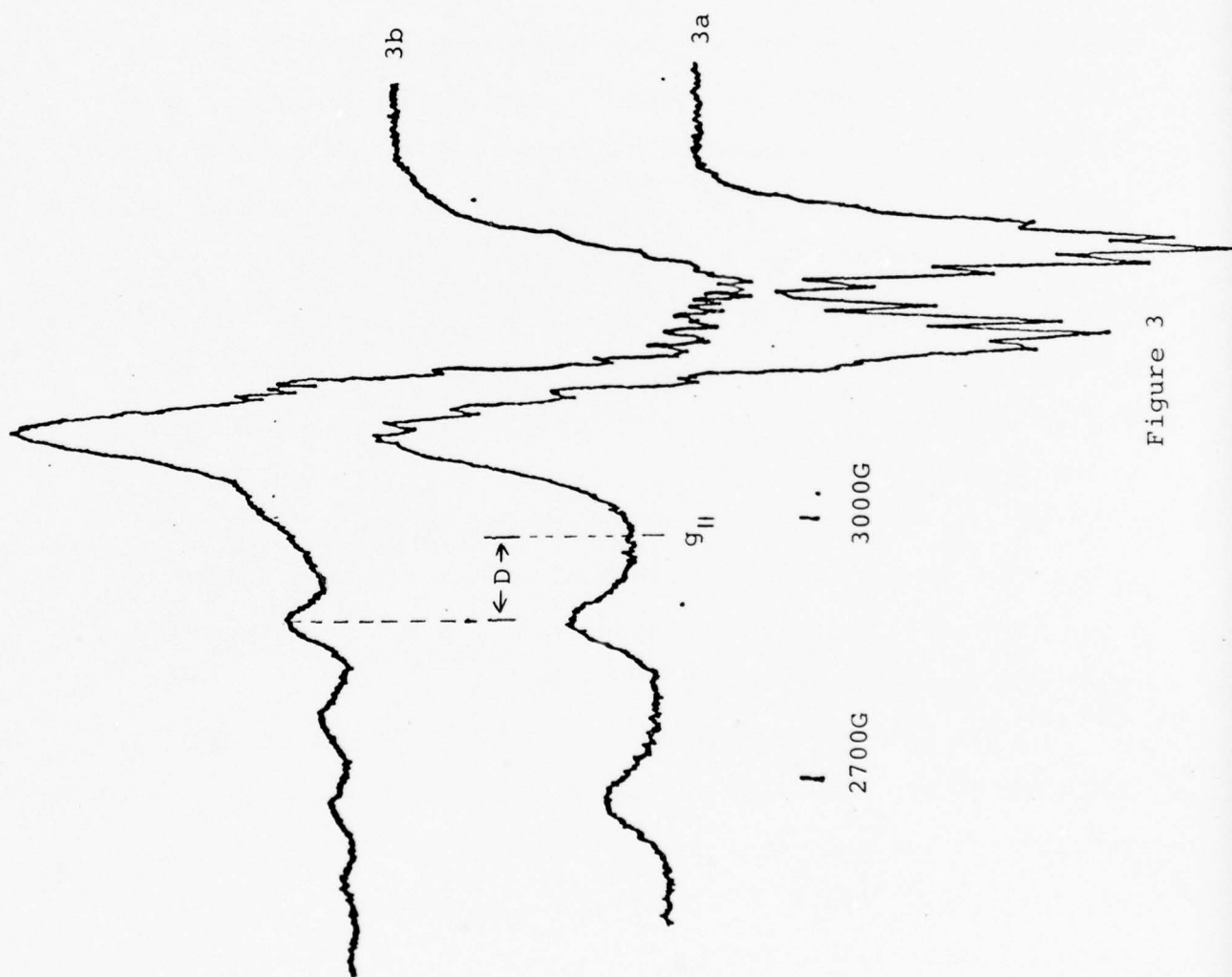
Hamiltonian parameters for the Cu(DUAC) are typical for those of a monomeric Cu(II) porphyrin (Table 4). The Cu(DUC) shows strong evidence for intramolecular copper-copper interactions. At least *five hyperfine lines are observed in the* $\Delta M_S = -1 \rightarrow 0$ *parallel* region. Overlap between the $\Delta M_S = 0 \rightarrow +1$ parallel multiplet and the perpendicular region prevents assignment of more of the fourteen expected parallel lines. Zero field splitting in the perpendicular region cannot be discerned due to the combination of copper and nitrogen hyperfine present. It should also be noted that theory predicts $A_{||}$ for the Cu(DUAC), 4 to be exactly twice that of Cu(DUC), 3. Figure 3 shows this clearly to be true. Spectra similar in appearance to those in Figure 3b are observed for Cu(DUFTF), indicating a similar copper-copper inter-action in this complex.

The zero field splitting parameter, D, which contains information pertaining to metal-metal distances is estimated as shown in Figure 3. Table 4 lists zero-field splitting parameters and copper-copper distances derived from them.

A set of ESR for the five coordinate Co(DUAC)(N-MeIm)$_2$ and Co(DUC)(N-MeIm)$_2$ complexes are shown in Figures 4a and 4b, respectively. Expansion of Figure 4b allows assignment of 16 of the expected 30 parallel peaks. Additionally, zero field splitting of the perpendicular region into the $\Delta M_S = -1 \longrightarrow 0$ and $0 \longrightarrow +1$ components is evident, due to the small interference of nitrogen

Table 4

ESR of Metal Containing Symmetric Dimeric Porphyrins

Complex	Base	$g_\parallel$	$g_\perp$	$A_\parallel$ (M)[1]	$A_\perp$ (M)[1]	D[1]	R(Å)[2]
Cu(TPP)[3]	--	2.19	2.03	210	30	--	--
Cu(DUAC)[3]	--	2.19	2.03	208	30	--	--
Cu(DUC)[3]	--	--	--	105	--	94	6.92
Cu(FTF)[3]	--	--	--	106	--	101	6.76
Cu(TPP)[4]	N-MeIm	2.22	2.04	190	30	--	--
Cu(DUAC)[4]	N-MeIm	2.22	2.04	193	30	--	--
Cu(DUC)[4]	N-MeIm	--	--	97	--	90	7.08
Cu(DUFTF)[4]	N-MeIm	--	--	97	--	96	6.94
Co(DUAC)[5]	N-MeIm	2.03	2.29	76	10	--	--
Co(DUC)[6]	N-MeIm	--	--	39	--	96	6.53

[1] In units of 10^{-4} cm^{-1}.

[2] R is metal-metal distance, in angstroms.

[3] Solvent is 60% toluene, 40% CH_2Cl_2.

[4] Solvent is 60% toluene, 30% CH_2Cl_2, 10% N-MeImid.

[5] [Co(DUAC)] = 3×10^{-4}M, [N-MeImid] = 1.7×10^{-3}M, only five coordinate cobalt present.

[6] [Co(DUC)] = 1.3×10^{-3}M, [N-MeIm] = 2.7×10^{-3}M.
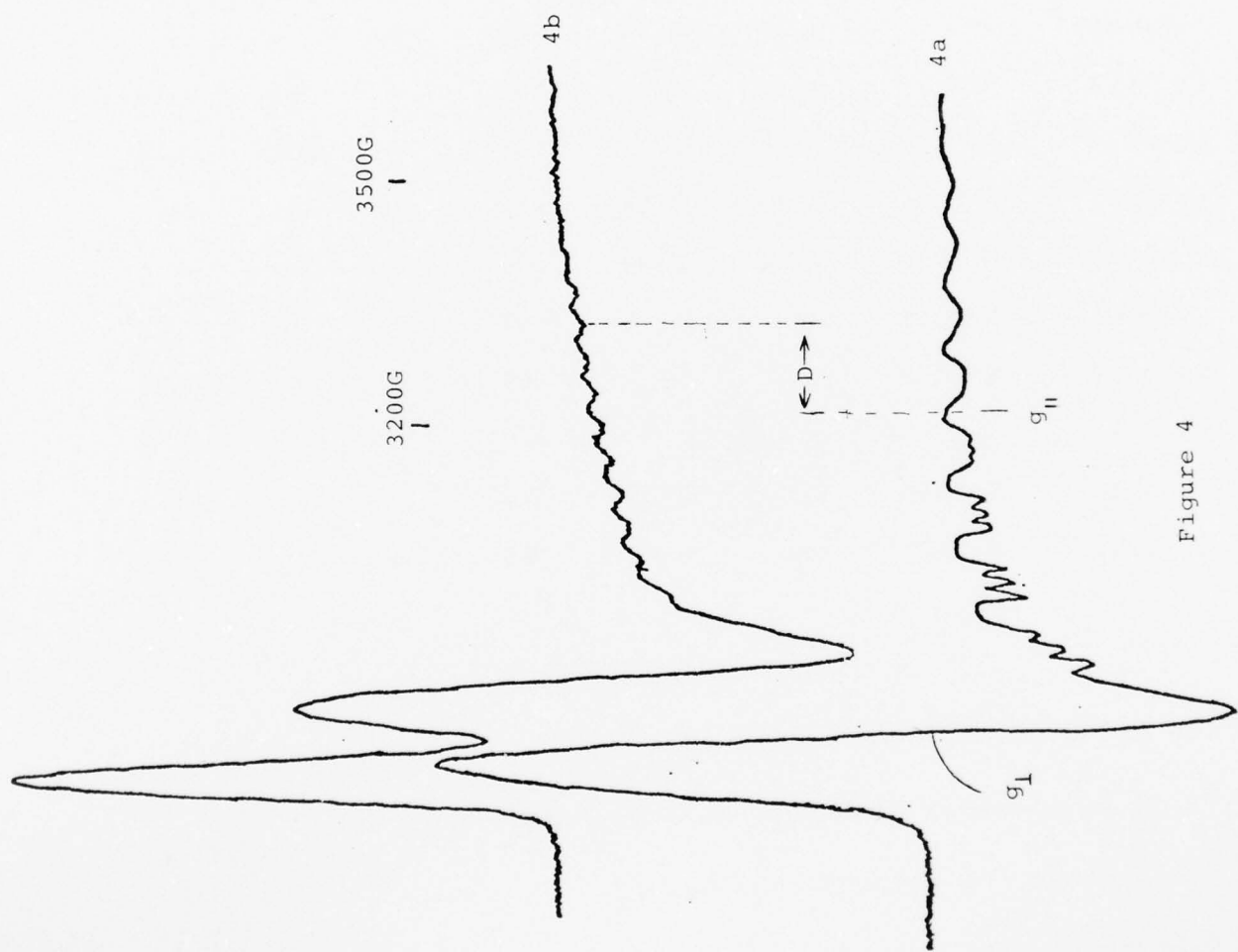
Figure 4

and cobalt hyperfine relative to Figure 3b. Included in Table 4
are the spin Hamiltonian parameters and cobalt-cobalt distances
describing these systems. Spectra of four coordinate Co(DUC)
solutions are extremely broad due to an apparent large cobalt-
cobalt interaction. The poor resolution precludes good
characterization of the spectral features.

The spectra observed in Figures 3b and 4b are not dependent
on the concentration of M(DUC) (also for corresponding M(DUFTF)
solutions). This observation, coupled with the fact that monomeric
Cu(TPP) and Co(TPP) species show no tendencies to aggregate
under the conditions employed, demonstrates that the observed metal-
metal interactions are intramolecular.

d. Infrared Spectra

The infrared spectra of 2, 3, 4 and 5 were obtained in KBr pellets. The distinguishing feature of these spectra is the carbonyl stretching frequency of the diurea moiety. This stretch is found at 1705 cm^{-1}, 1715 cm^{-1}, 1705 cm^{-1}, and 1675 cm^{-1} for compounds 2, 3, 4 and 5 respectively. Literature values for carbonyl stretches in N,N'-diarylureas are ~1640 cm^{-1}. The higher values found in the porphyrins studied may be due to the fact that the rigid phenyl rings impose a constrained geometry on the carbonyl segment, altering the stretching frequency.

e. Electrochemical Studies

As pointed out previously, voltammetric studies of 1 revealed no electronic interaction between the two porphyrin halves. In a similar manner, no potential shifts or splitting of peaks were observed in cyclic voltammetric studies of either 4 and 5 or their Co(II) derivatives. This is not surprising since the porphyrins are geometrically ill-disposed in 4 to allow through space interactions and in 5 the molecule is only a monomeric porphyrin.

Upon the reduction to the radical anion, 2 gives two nonresolved waves appearing at approximately the same potential as the reduction in 5, (-1.21v vs. SCE). The reduction of 3 yields two partially resolved waves with $E_{\frac{1}{2}}$ of -1.16 and -1.25 v. vs. SCE respectively. The absence of a split voltammetric wave for

5 and the increasing splitting in moving from 2 to 3 demonstrate
the existence of a through space electronic interaction between
the two porphyrins in 2 and 3. The observed peak separation is
an apparent manifestation of the overlap of the π systems of the
porphyrin halves.

Data for the voltammetric reduction of the Co(II)
derivatives of 2, 3, 4, and 5 give qualitatively similar results
to those found in the metal-free porphyrins. The peaks
corresponding to the Co(II) $\rightarrow$ Co(I) reduction in the Co(DUC)
and Co(DUFTF) were split to a much greater degree than were the
peaks for the reduction to the π radical of the same metal-free
porphyrin. The largest peak splitting occurred for the
Co(II) $\longrightarrow$ Co(I) reduction in Co(DUFTF) where the $E_{\frac{1}{2}}$'s are
separated by .125 volts. The larger apparent degree of inter-
action in the Co(II) derivatives of 2 and 3 likely results from
the overlap of Co(II) d_z2 orbitals acting in addition to the
interaction of the porphyrin   systems.

6.   Summary

Further studies on the previously reported clamshell
porphyrin, 1, do not indicate interaction between porphyrin
halves in either the metal-free porphyrin or metal containing
derivatives. Two new dimeric porphyrins, 2 and 3, have been
synthesized, the latter of which is the first example of a
"face-to-face" porphyrin. All physical studies conducted on 2
and 3 as well as their corresponding Co(II) and Cu(II) derivatives

demonstrate intramolecular interactions between the porphyrin halves. Physical techniques utilized include electronic, infrared, NMR, and ESR spectroscopy. Voltammetric data are in accord with the spectroscopy data in demonstrating intramolecular interactions.

These results suggest that the two halves of such dimeric porphyrins can act together in two-center multielectron processes. The spatial characteristics of 2 and 3 are suitable for molecules such as dioxygen and dinitrogen to simultaneously interact with both metal centers. Such interactions can help facilitate multielectron reductions and prevent the accumulation of partially reduced products, which can be a problem with mono-nuclear reductants.

References

(1) J. P. Collman, "Synthesis of New Types of Catalyst Materials", Semi-Annual Technical Report, Long Range Materials Research, ARPA order No. 3018, January, 1976. Center for Materials Research, Stanford University, Stanford, California.

(2) H. Budzikiewicz, C. Djerassi, and D. H. Williams, Mass Spectrometry of Organic Compounds, Holden-Day Inc., San Francisco, pp. 503-506, 1967.

B. Genesis of Small Au-Pd Alloy Particles on Silica

M. Boudart

1. Introduction

The method of ion-exchange has been successfully used to prepare very small particles of Pt and Pd on SiO_2 (1,2). This method makes use of the exchange of tetramine platinum(II) or tetramine palladium(II) cations with surface protons of SiO_2 to form precursors. Small particles of Pt or Pd are formed after controlled treatment of the precursors.

In order to extend this method to the preparation of supported Au and Au-Pd alloys, an amine complex of Au which is stable in the same conditions for optimum exchange of tetramine palladium(II) with the surface protons must be employed. Though complexes such as $[Au(NH_3)_4]^{3+}$ have been reported(3,4), they are unstable in aqueous alkaline solution. Hydrolysis of the complex cation to yellowish brown $Au(OH)_3$ readily occurs at room temperature. In contrast, complexes of Au(III) with multidentate ligands are stable to hydrolysis. In particular, $[Au(en)_2]^{3+}$, where (en) stands for the bidentate ethylene diamine, a relatively simple complex, is stable from pH of 3 to 12, and is readily prepared from $HAuCl_4 \cdot 3H_2O$ and ethylene diamine solutions.

The following experimental and results sections are each subdivided into four parts.

The first part describes the use of the Au amine complex to prepare the precursors. Sulcek et. al. had studied the optimum exchange conditions for amines of Pd, Au and Pt with protons on the surface on SiO_2, examining factors such as the temperature, the pH and the amine concentration of the solution (5). Such conditions were employed to prepare precursors of highly dispersed Pd (2). Though the details for the decomposition of the precursors are given in the first part, their rationale is the result of a study described in the second part. This study determined the minimum decomposition temperatures of the precursors in dioxygen and dihydrogen.

The third part reports x-ray characterization (diffraction patterns) of the samples after reduction or after oxidation. This technique conveniently ruled out preparative methods that yielded large metallic particles or alloys with compositions greatly differing from the desired composition.

The fourth part reports data of volumetric adsorption of dihydrogen, carbon monoxide, and dioxygen, and of dihydrogen titration on oxygen preadsorbed surfaces. From these data, the qualitative evidence for Au-Pd associative interaction and the estimation of the particle size of the alloys are obtained.

2 Experimental

Catalyst Preparation

The catalyst preparation consists of three consecutive steps:

a) Preparation of $[Au(en)_2]Cl_3$

This complex salt was prepared by the method of Block and Bailer(6).

b) Ion-exchange

A weighted amount of silica (Silica Gel Grade 950 from Davison, specific area 700 M^2 g^{-1}, specific pore volume 0.4 cm^3 g^{-1}) was warmed to 343 K in aqueous ammonia of pH about 11. The amount of solution was adjusted to 20 cm^3 per gram of silica. The appropriate amount of $[Au(en)_2]Cl_3$ was dissolved in a calculated amount of 0.01 M solution of $[Pd(NH_3)_4]Cl_2$, to give the desired alloy composition. The concentration of $[Au(en)_2]Cl_3$ was never allowed to exceed 0.01 M. Aqueous ammonia solution was added where dilution was necessary.

The well mixed solution of complex salts was added dropwise into the slurry of silica at a rate of approximately 6 cm^3 per minute. At this rate, the temperature of the slurry never fell below 335 K. After the addition of the solution, the slurry was maintained at 343 K to 335 K for one hour and then cooled to room temperature. The treated silica, hence designated as the precursor, was filtered and thoroughly washed with at least three portions (5-6 cm^3 per g of silica) of doubly distilled water.

c) Drying and Controlled Reduction

A weighted amount of the precursor was loaded into a Pyrex glass cell and evacuated by a diffusion pump at 333 K overnight. After the

cell was cooled down to room temperature, dihydrogen which had been purified by passing through a palladium thimble (Surfass) was passed over the precursor at a space velocity of about 5 s^{-1}. The precursor was slowly heated to 423 K and then maintained at that temperature for three more hours before cooling down to room temperature in flowing dihydrogen. After evacuation at room temperature for 0.5 h, the sample was slowly exposed to air and then stored. A portion of such sample was submitted to elemental analysis by atomic absorption.

Minimum Decomposition Temperatures in Dihydrogen and in Dioxygen

In Dihydrogen

The minimum reduction temperature of adsorbed $[Au(en)_2]^{3+}$ on SiO_2 was determined by a static volumetric method described elsewhere(7). In brief, a weighted amount of the precursor containing only Au amine but not Pd amine was dried by evacuation at 333 K overnight and a known amount of dihydrogen was allowed to contact the sample at room temperature. A dihydrogen adsorption isotherm was then obtained. The sample was maintained at temperature T for 2 h. It was then cooled to room temperature and an adsorption isotherm was obtained. The amount of dihydrogen taken up was determined by extrapolation to zero pressure. This process was repeated using a number of progressively increasing temperatures.

In Dioxygen

The minimum decomposition temperature in dioxygen was observed by infrared spectroscopy.

A sample wafer of thickness 10-12 mg cm^{-2} was placed in a stainless steel cell designed for in-situ study of study of catalysts (8). After 2 h of evacuation at room temperature, dioxygen which had been purified by passing through a molecular sieve trap at 195 K was introduced at a space velocity of about 5 s^{-1}. The sample was heated to a temperature T. The sample was kept at this temperature for 2 h, and then cooled down to toom temperature at which an infrared spectrum was obtained. This process was repeated at several higher values of T.

X-ray Diffraction

X-ray diffraction patterns were obtained by a Picer X-ray diffractometer. Nickel-filtered Cu radiation was collimated by 1 - 2° Soller slits. For samples that gave defined diffraction patterns, x-ray line broadening was studied. To calculate the linewidth (or width at half maximum intensity), instrumental broadening was corrected for with crystalline α-quartz at $2\theta = 26.66°$ and the Warren's method of instrumental broadening correction. The X-ray particle size was calculated from the Scherrer equation using a shape factor of 0.9 (9).

Adsorption

Apparatus and Materials

The apparatus was a conventional high vacuum manifold connected to a high precision pressure gauge (Texas Instruments). The apparatus has been described in detail elsewhere (10). The purification of all gases used is presented in Appendix II.

Procedure

All samples had been previously reduced according to the schedule described above. Prior to a characterization, each sample was re-reduced at 573 K for 3 h and then evacuated to about 10^{-7} kPa for 1 h at 573 K. It was then cooled to room temperature for about 0.5 h and then a adsorption isotherm was obtained. Then, the sample was evacuated at room temperature for 0.5 h and a backsorption isotherm was obtained.

Titration by dihydrogen of preadsorbed oxygen was performed after adsorption of dioxygen. The sample was evacuated for 1 h at room temperature at about 10^{-7} kPa. Dihydrogen was then allowed to contact the sample. Dihydrogen backsorption was also carried out as after a dihydrogen adsorption experiment.

3. Results

Catalyst Preparation

Table 2.1 summarizes the results of atomic analysis for the samples prepared in this study. For convenience these samples are coded. This nomenclature will be used throughout whenever appropriate.

A sample is designated as $L(x:y)$ or $H(x:y)$ or $ME(x:y)$, where $x:y$ represents the mole ratio of Au to Pd in the starting complex solution for exchange. The letters L, H and ME show that the metal loading is approximately 125, 250 and above 380 μ mol g^{-1} respectively.

Except for $L(80:20)$, the results of the elemental analysis are in good agreement with the nominal Au to Pd mole ratios.

A possible explanation for the deviation between the nominal and the determined composition for $L(80:20)$ is as follows. Instead of using freshly prepared Au amine salt, the amine salt used had been prepared for 10 days before exchange. It was dissolved in water and filtered to remove possible photodecomposed Au salt. Filtration loss or photodecomposition of the Au complex to Au metal might have occurred. Hence the Au complex solution was diluted. Such a deviation from nominal composition was circumvented in later preparations by using freshly prepared complexes for exchange (within one or two days).

Minimum Decomposition Temperature

The observed minimum decomposition temperatures are best represented by temperature ranges which are summarized in Table 2.2.

In Dihydrogen (by volumetric method)

Figs. 2.3a and 2.3b illustrate typical plots of the uptake of dihydrogen as a function of temperature by precursors of samples that contain 2.0 wt % Au on SiO$_2$.

Table 2.1   Sample Specification

Sample Designation	Mole ratio Au:Pd	Metal contents/μmol g^{-1}			Au wt. %
		Au	Pd	total	
L(0:100)	0 : 100	0.0	131.1	131.1	0.00
L(20:80)	19.4:79.6	25.4	99.1	124.5	0.50
L(40:60)	40.2:59.8	45.7	67.9	113.6	0.90
L(60:40)	54.2:45.8	66.0	55.7	121.7	1.30
L(80:20)	66.7:33.3	88.8	44.3	133.1	1.75
L(100:0)	100 : 0	121.8	0.0	121.8	2.40
H(0:100)	0 : 100	0.0	227.2	227.2	0.00
H(20:80)	20.8:79.2	51.8	197.2	249.0	1.02
H(40:60)	42.1:57.9	114.7	157.5	272.3	2.26
H(60:40)	59.0:41.0	133.0	92.5	225.4	2.62
H(80:20)	79.7:20.3	188.3	48.1	236.4	3.71
H(100:0)	100 : 0	216.8	0.0	216.8	4.27
ME(20:80)	23.0:77.0	169.5	566.0	735.6	3.34
ME(52:48)	53.1:46.9	244.7	216.0	460.7	4.82
ME(100:0)	100 : 0	380.7	0.0	380.7	7.50
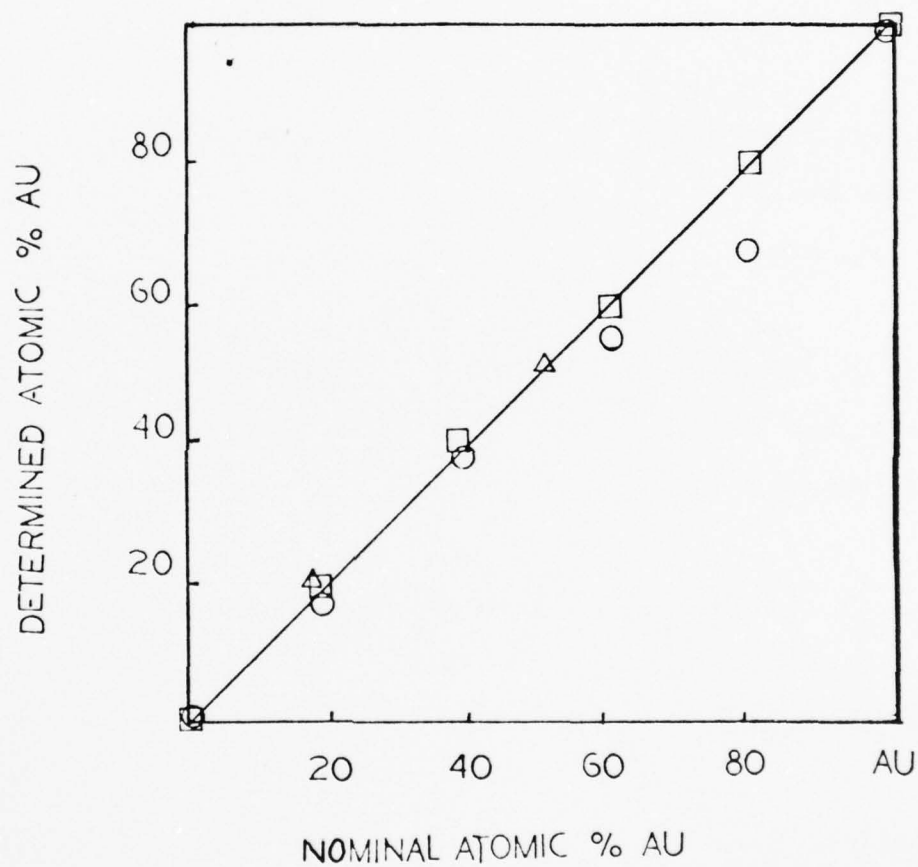
Fig. 2.1 Atomic analysis of Au–Pd/SiO$_2$

☐ H(x:y)

◯ L (x:y)

△ ME(x:y)

Table 2.2 Minimum decomposition temperature

Sample	In O_2	In H_2
1. 2.0 wt. % Au/SiO$_2$ from HAuCl$_4$ impregnation	---	443-468 K
2. 2.0 wt. % Au/SiO$_2$ from ion-exchange of $[Au(en)_2]^{3+}$	413-440 K	413-453 K
3. 4.0 wt. % Au/SiO$_2$ from ion-exchange of $[Au(en)_2]^{3+}$	413-440 K	413-453 K
4. sample 2, pre-oxidized	---	446-473 K
5. sample 3, pre-oxidized	---	446-473 K

Fig. 2.3 Minimum reduction temperatures of
$[Au(en)_2]^{3+}$/SiO_2 and $HAuCl_4$/SiO_2

$[Au(en)_2]^{3+}$ /SiO_2

$HAuCl_4$/SiO_2

REDUCTION TEMP/K

UPTAKE / μMOLE g^{-1}
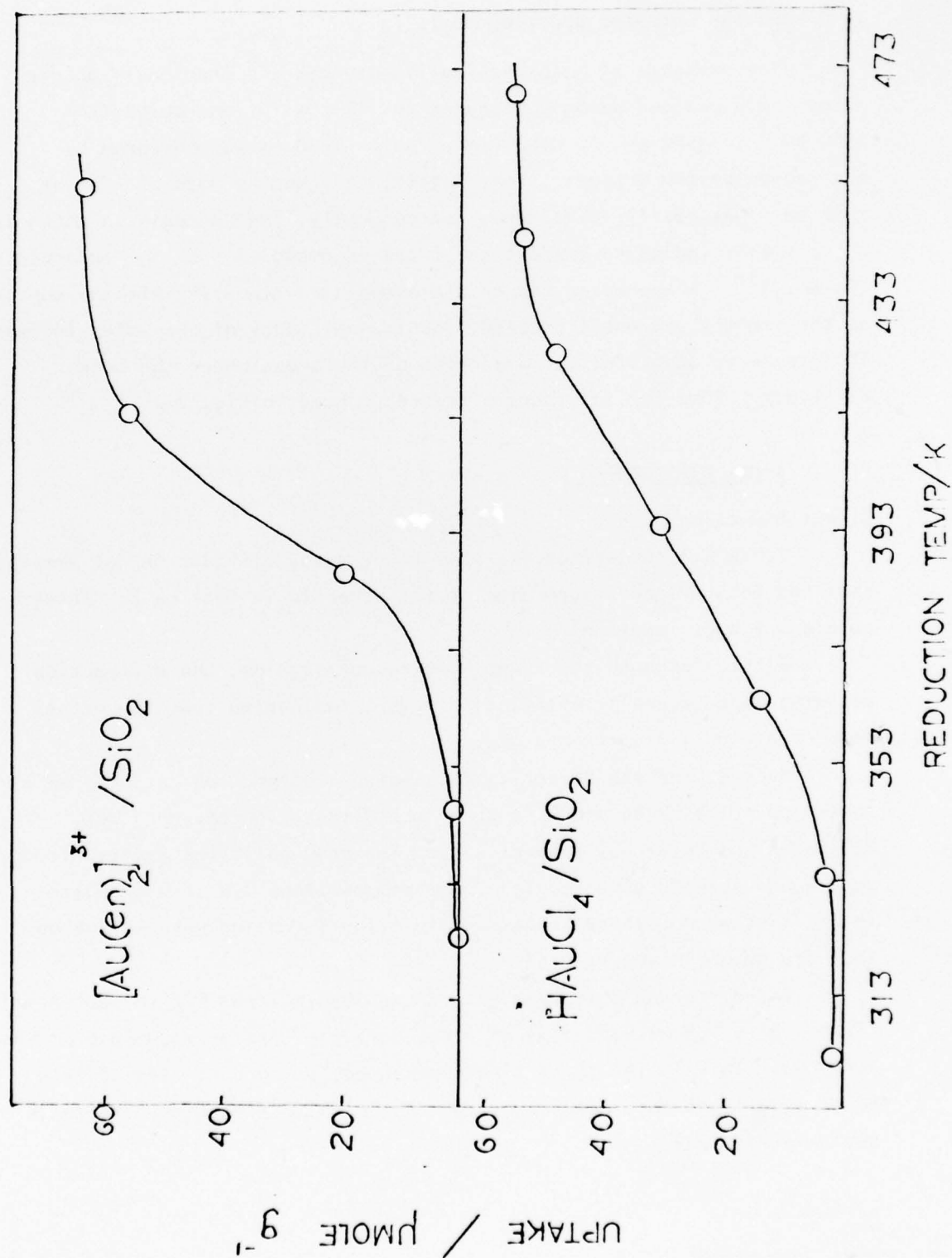
In Oxygen (by infrared spectroscopy)

The presence of both physically adsorbed and chemically bonded water and exchanged ammonia obscured the IR absorption region from 2400 cm^{-1} to 3600 cm^{-1}. The region below 1200 cm was obscured by absorption by the support. Fortunately, the bending mode of $-CH_2$ at 1455 cm^{-1} was easily identified. Consequently, the decrease in intensity of this band indicated the extent of the decomposition of the adsorbed $[Au(en)_2]^{3+}$. Since water vapour and ammonia continously left the support as the temperature was increased, the transmittance of the wafer increased. This rendered quantitative comparison of the areas under the peaks difficult. Some typical spectra are reproduced in Fig. 2.2.

X-ray Diffraction

Direct Reduction

Table 2.3 summarizes the results of X-ray diffraction for samples that had been prepared according to the schedule in Section 2. Three points are worth mentioning.

First, for both the L and H series of samples, the diffraction patterns were generally extremely diffuse, indicating that the metals were in a highly dispersed state.

Second, for the ME series of samples, diffraction patterns were observed. Figs. 2.4a and 2.4b show the diffraction patterns for ME(20:80) and ME(52:48) respectively. The peak positions shifted from pure Au or pure Pd expected for their compositions. With a graphite internal standard, these shifts due to alloy formation were estimated. They are shown in the figures.

Third, for Au only samples with Au loading from 122 to 380 μ mol g^{-1} (from 2.4 to 7.5 wt percent), an x-ray particle size of about 3.0 nm was obtained. This is the first time that supported Au particles of this small size range have been reported. A typical diffraction pattern is shown in Fig. 2.5.

-94-
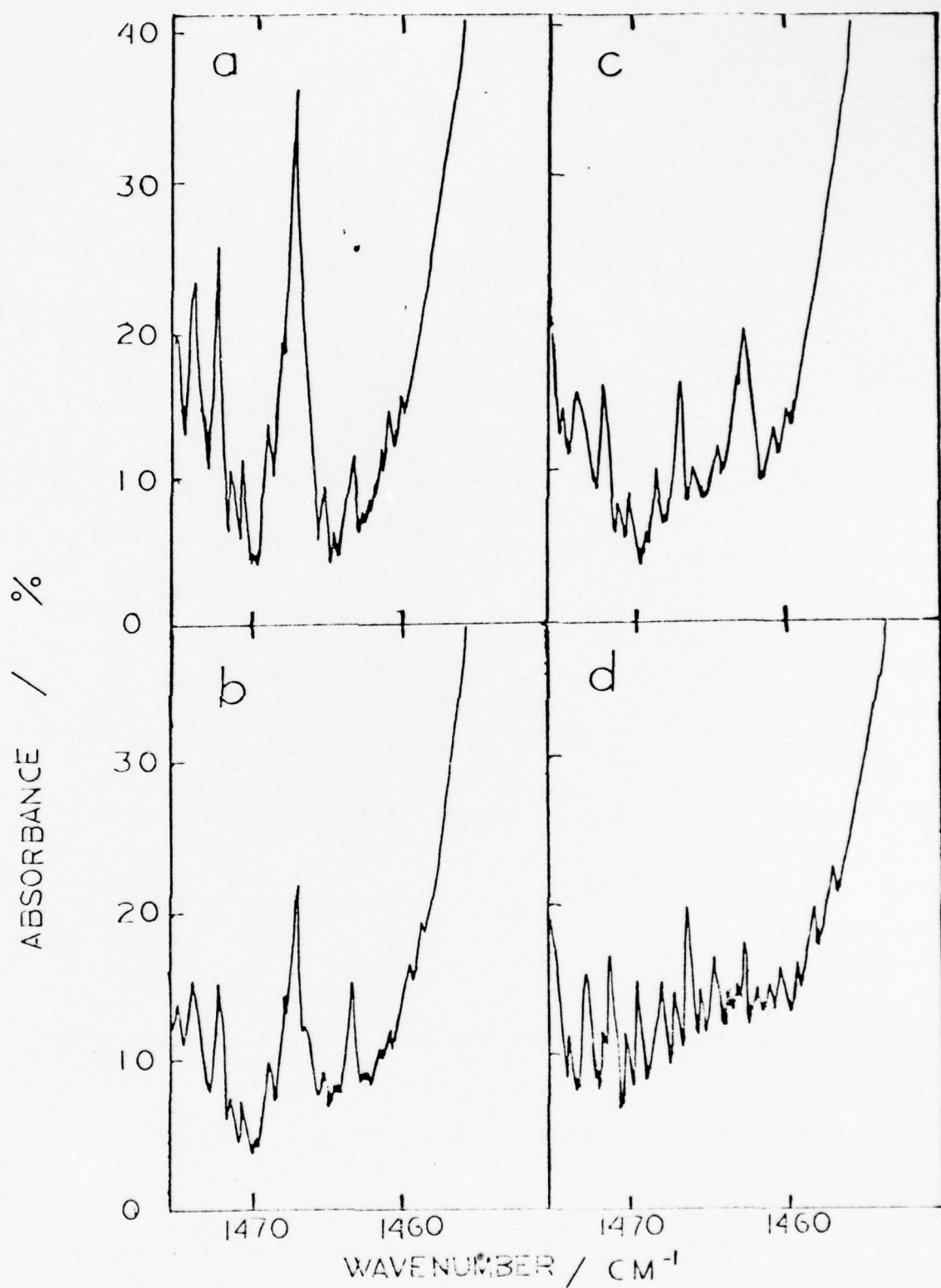
Fig. 2.2 Infrared spectra of $[AU(en)_2]^{3+}/SiO_2$ and NH_4^+/SiO_2

$[AU(en)_2]^{3+}/SiO_2$ decomposed in O_2 :

a: at 373 K   c: at 440 K
b: at 413 K   d: NH_4^+/SiO_2

-95-

Table 2.3 X-ray Diffraction Data

Composition Au:Pd = x:y	Series L(x:y)	H(x:y)	ME(x:y)
0:100	A	A	--
20:80	A	A	S; (1.5) <1.9>
40:60	A	A	--
52:48	--	--	S; (2.9) <2.3>
60:40	D	D	--
80:20	D	S; (4.1) <4.7>	--
100:0	(2.8)	(3.2)	(3.0)

A : X-ray amorphous;   D : Diffuse pattern;   S : alloy shift observed

(xx) : Particle size estimates, in nm, by X-ray line broadening

<xx> : Particle size estimates, in nm, by CO adsorption; assumptions: 1, surface composition = bulk composition, 2, CO/Pd(surface) = 1.

INTENSITY (ARB. UNITS)

Pd (III) 2.246 2.355 Au (III)

2.27

ASSUMED LINEAR BASELINE

(a)

DIFFRACTION ANGLE 2θ / °
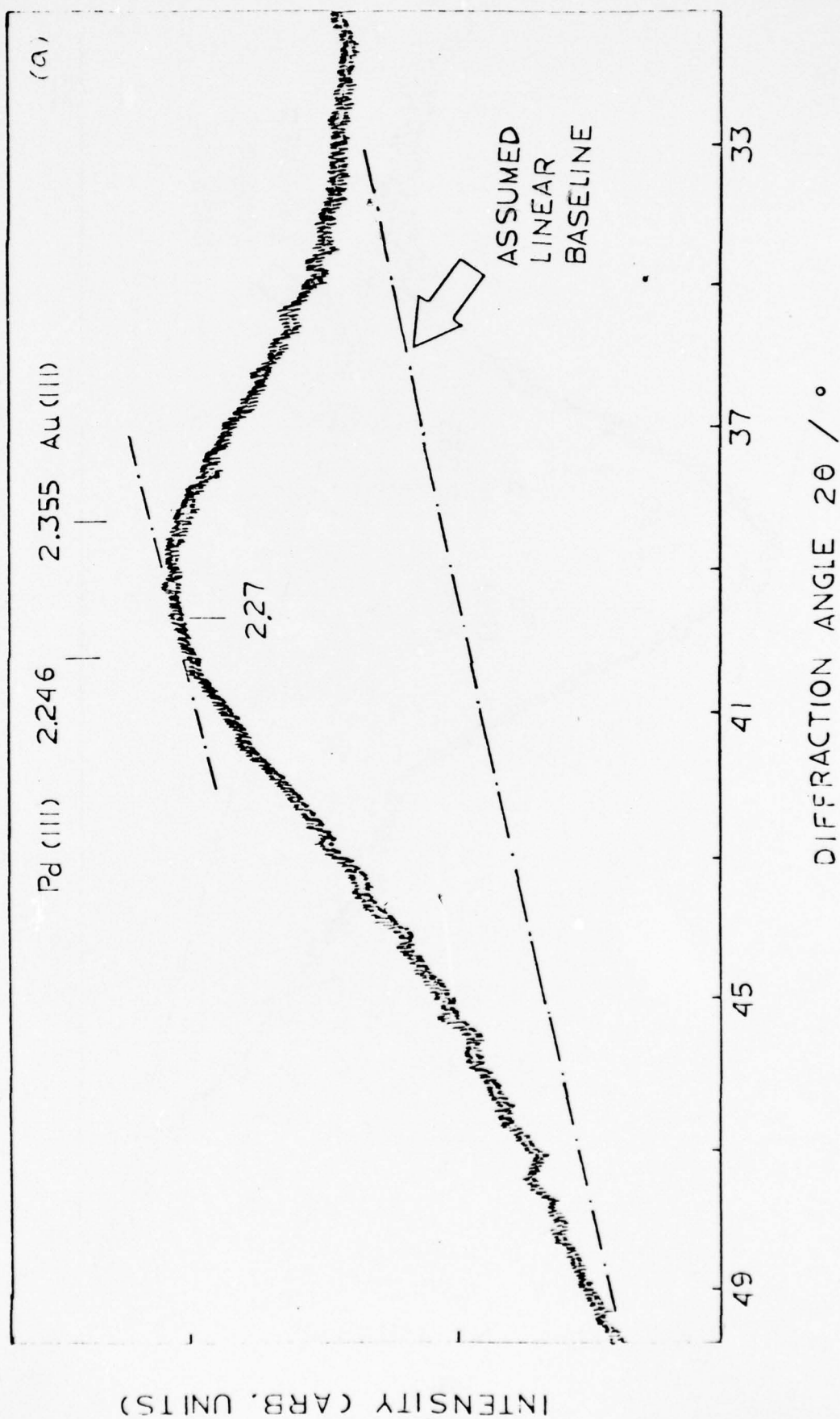
Fig. 2.4 X-ray diffraction patterns (a) ME(20:80)

-97-

Fig. 2.4 X-ray diffraction patterns   (b) ME(52:48)

(b)

ASSUMED
LINEAR
BASELINE

2.30

Pd   Au
(111)   (111)
2.246   2.355

RELATIVE INTENSITY (ARB. UNITS)

DIFFRACTION ANGLE 2θ / °

33   37   41   45   49
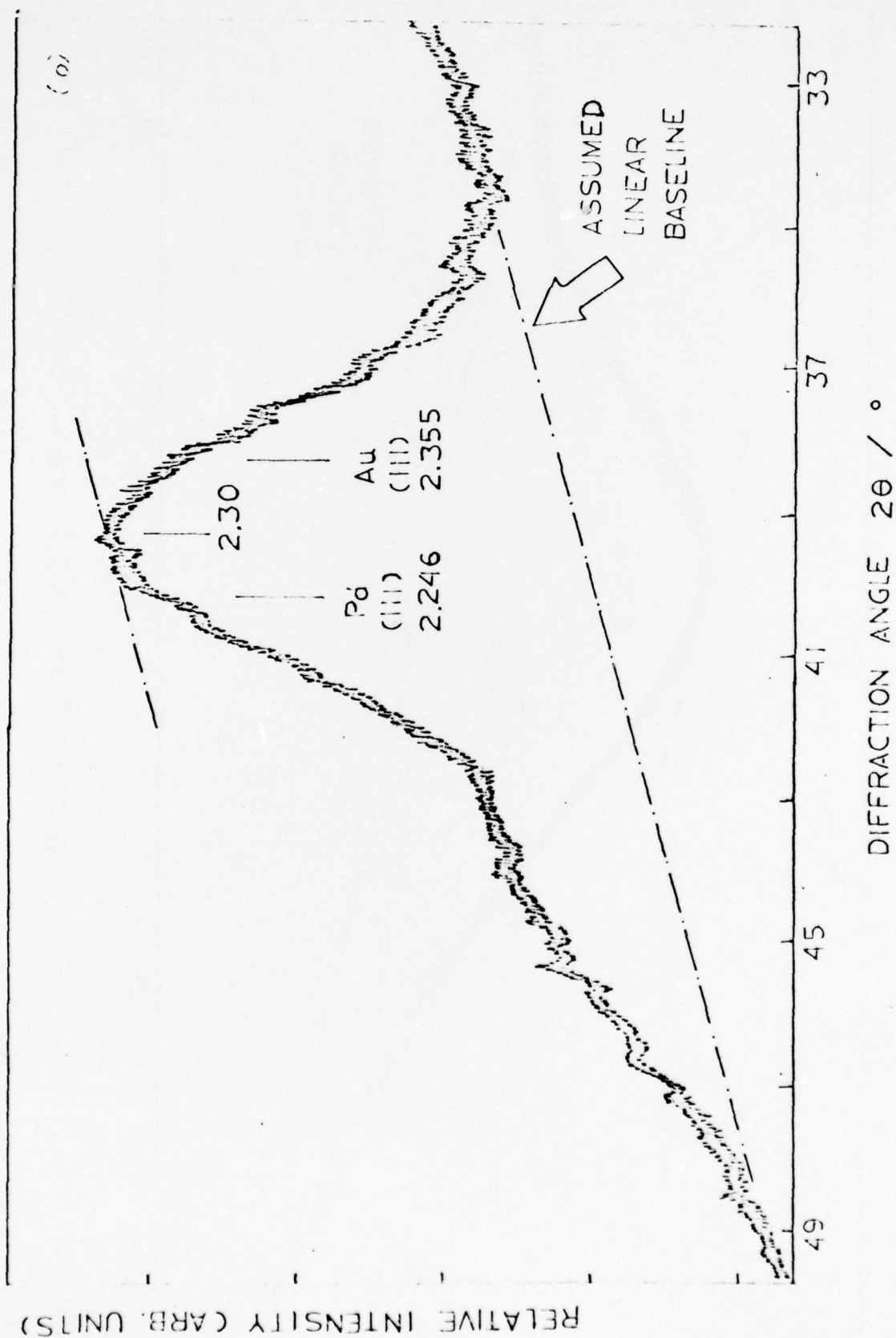
Fig. 2.5 X-ray diffraction pattern for
ME(100:0), 7.5 wt.% Au/SiO$_2$

DIFFRACTION ANGLE 2θ / °

INTENSITY (ARB. UNITS)
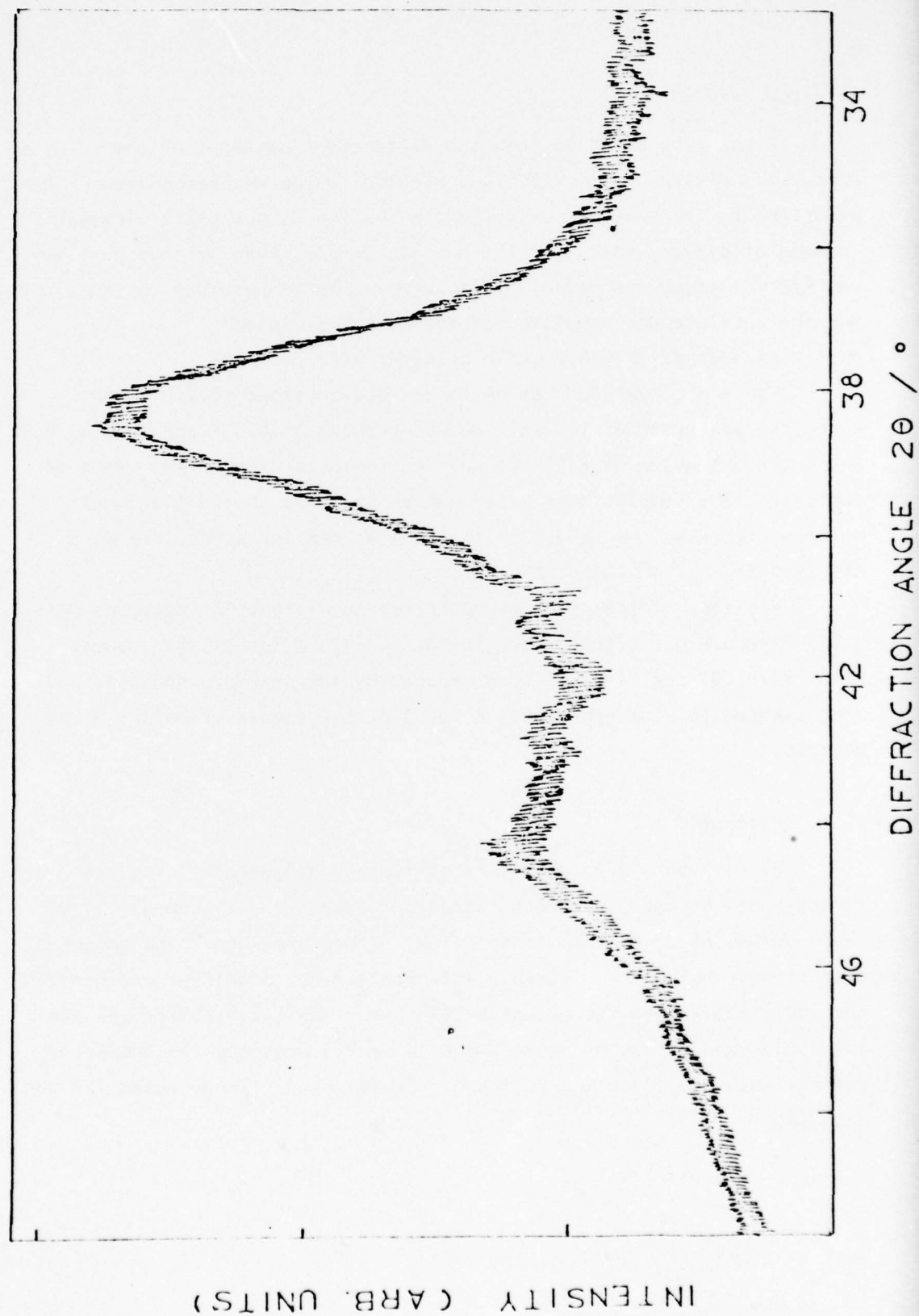
Oxidized Samples

Figs. 2.6a and 2.7a show the diffraction patterns of the precursors of 1.3 wt % Au/SiO_2 and H(40:60) which was decomposed according to the schedule described in Section 2, but using dioxygen instead of dihydrogen. (For the Au only sample, the final temperature was 473 K instead instead of 573 K, since this temperature was sufficient for the complete decomposition of the adsorbed $[Au(en)_2]^{3+}$. Gold particles greater than 6.0 nm in diameter were observed.

These observations can be contrasted to those of Fig. 2.6b where the precursor of 1.3 wt % Au was reduced at 473 K and to Fig. 2.7b where the precursor of H(40:60) was reduced according to the standard schedule. The samples were x-ray amorphous. The same differences between oxidation and reduction (by similar heating schedules) were observed for L(20:80) and H(20:80).

For the oxidized samples, distinct Au diffraction patterns were still observed on further reduction at 573-773 K for 3-5 h. However, after H(20:80) and H(40:60) were reduced by the standard schedule and then exposed to dioxygen at 573 K for 3 h, the samples remained x-ray amorphous.

Adsorption

Figs. 2.8a - 2.8d show sets of typical dihydrogen, dioxygen, carbon monoxide and dihydrogen titration isotherms. The amount of gas taken up was obtained by extrapolation to zero pressure. The amount of gas strongly held on the surface was obtained by the difference between the total uptake and the amount backsorbed. Table 2.4 summarizes the adsorption and titration data, while Table 2.5 presents the uptake of gas per mole of Pd and the ratios of uptakes of different gases for the same sample.

-100-
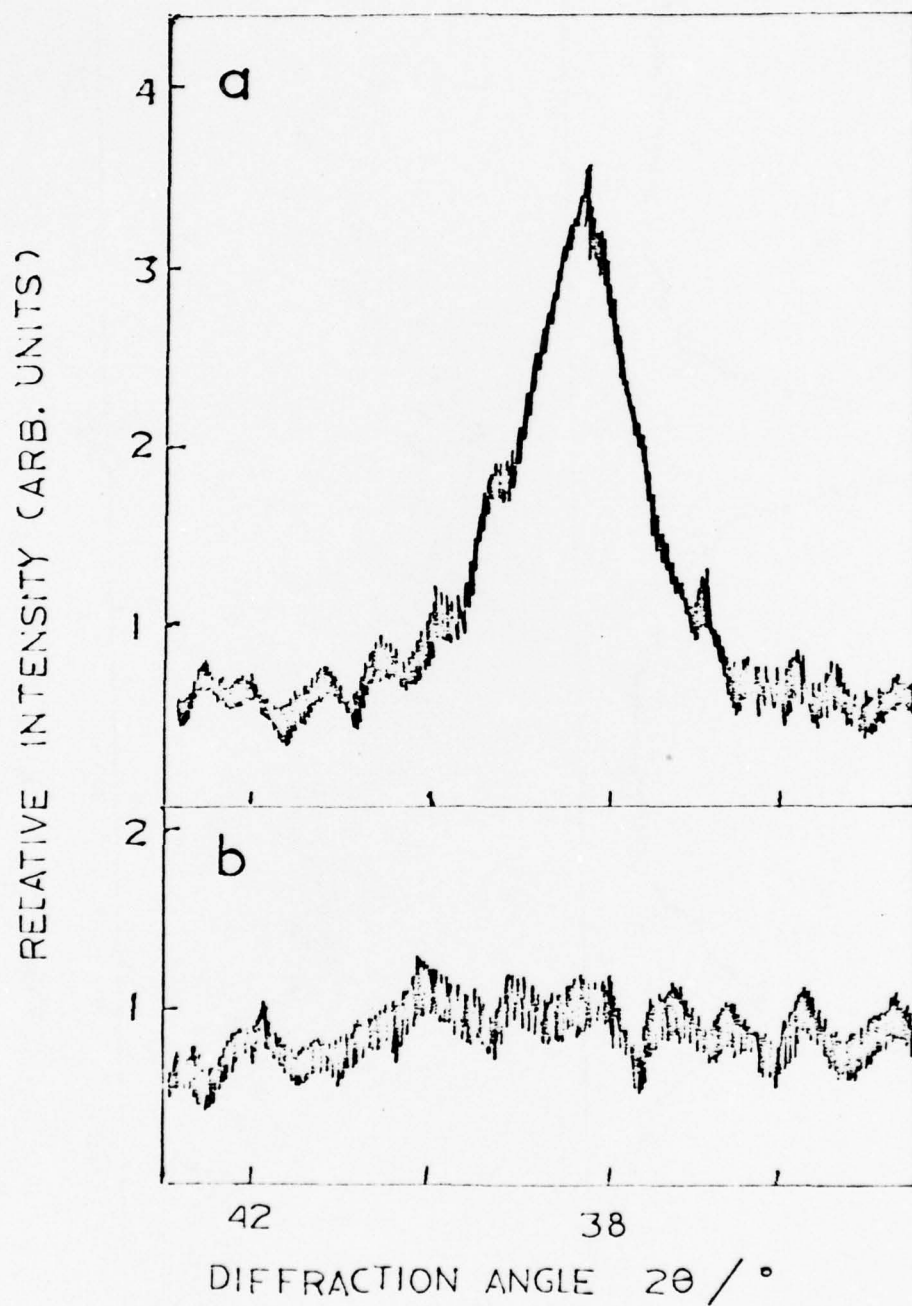
Fig. 2.6   X-ray diffraction patterns for 1.3 wt. % Au/SiO$_2$

a: precursor decomposed by O$_2$ at 473 K

b: precursor decomposed by H$_2$ at 473 K

Fig. 2.7   X-ray diffraction patterns for H(40:60)

a: precursor decomposed in O_2 at 573 K

b: precursor decomposed in H_2 at 573 K
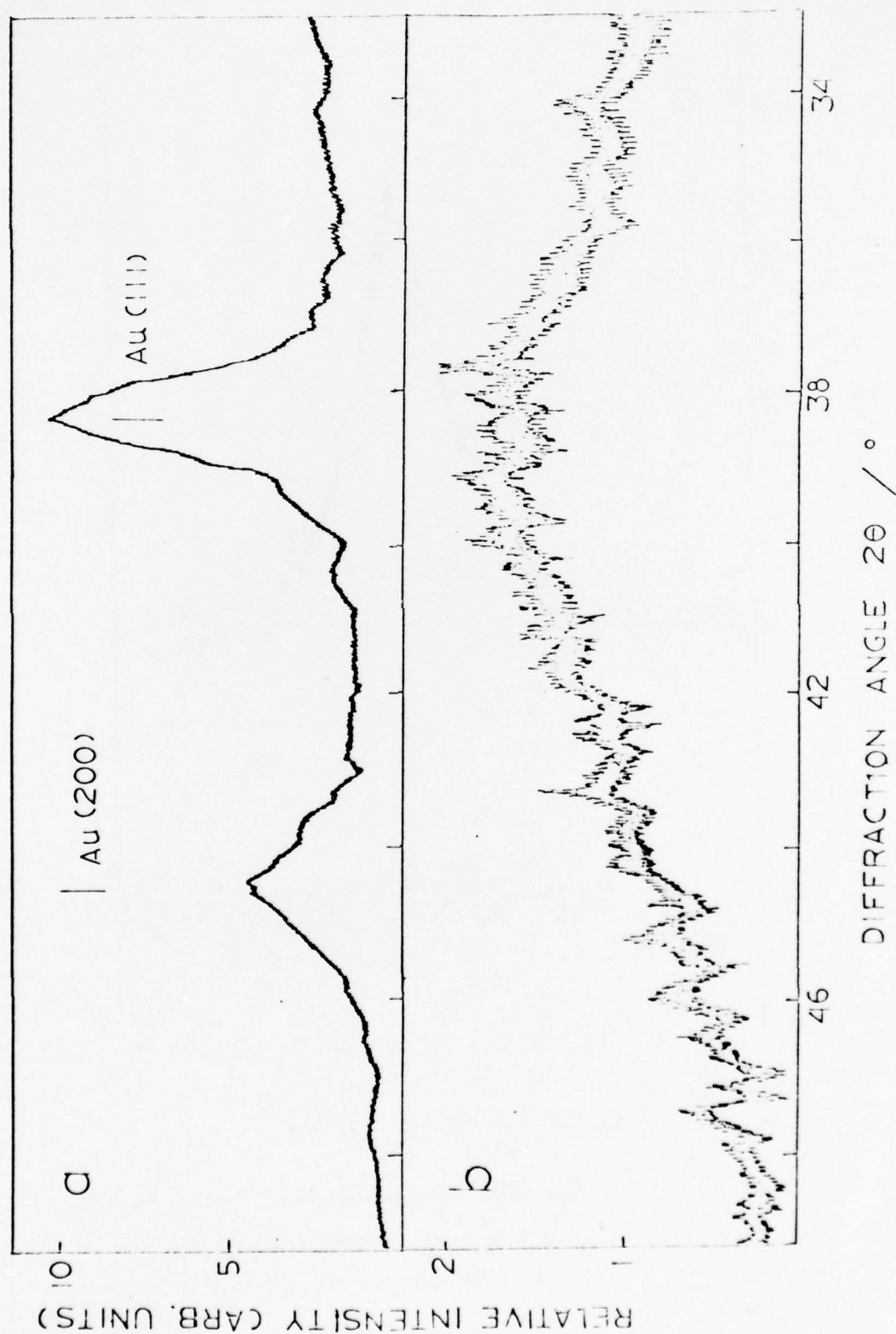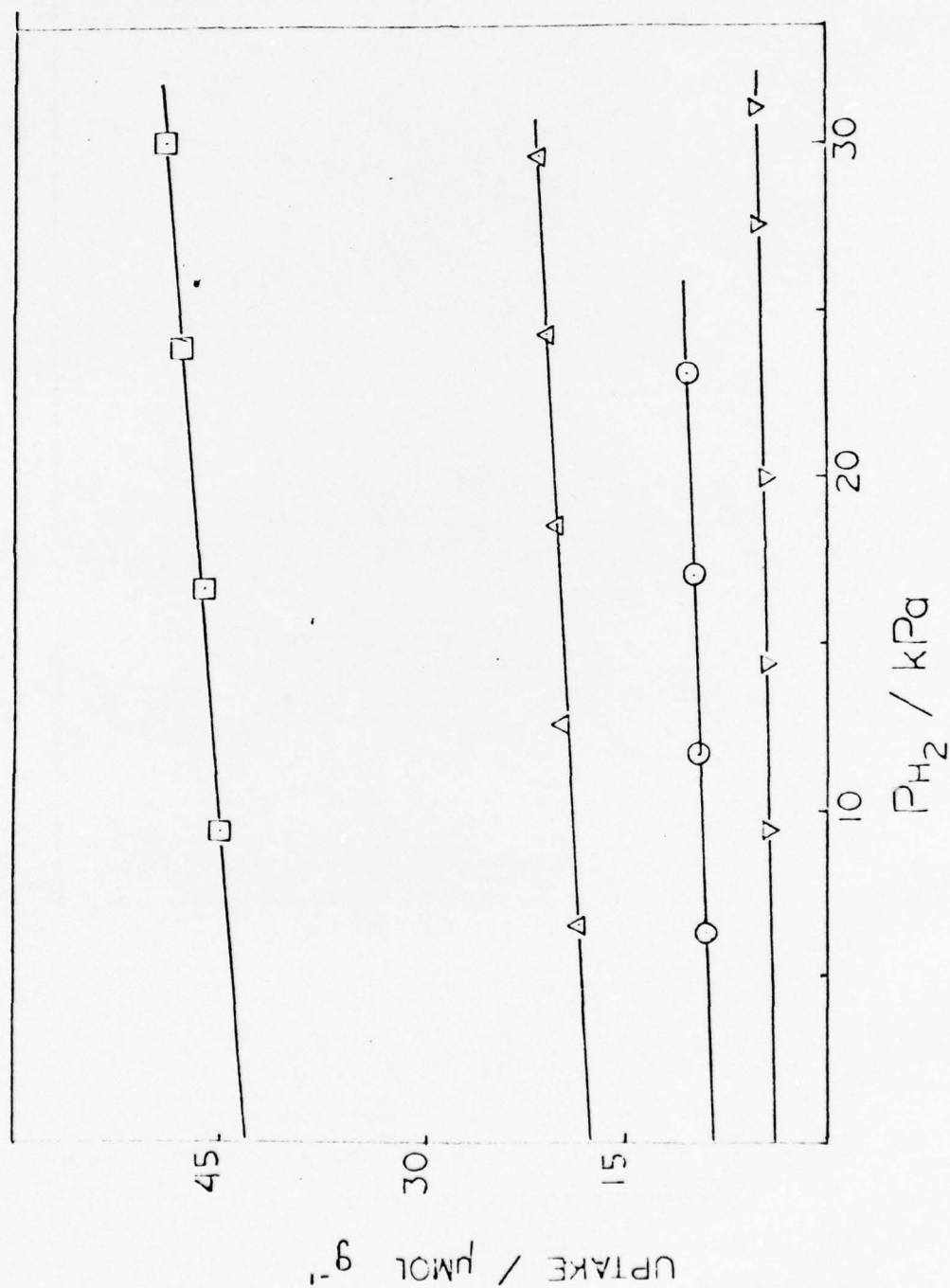
Fig. 2.8 a   Dihydrogen total uptake isotherms at 295 K, after evacuation at 573 K, 1 h

□ L(20:80)   ○ L(60:40)
△ L(40:60)   ▽ L(80:20)
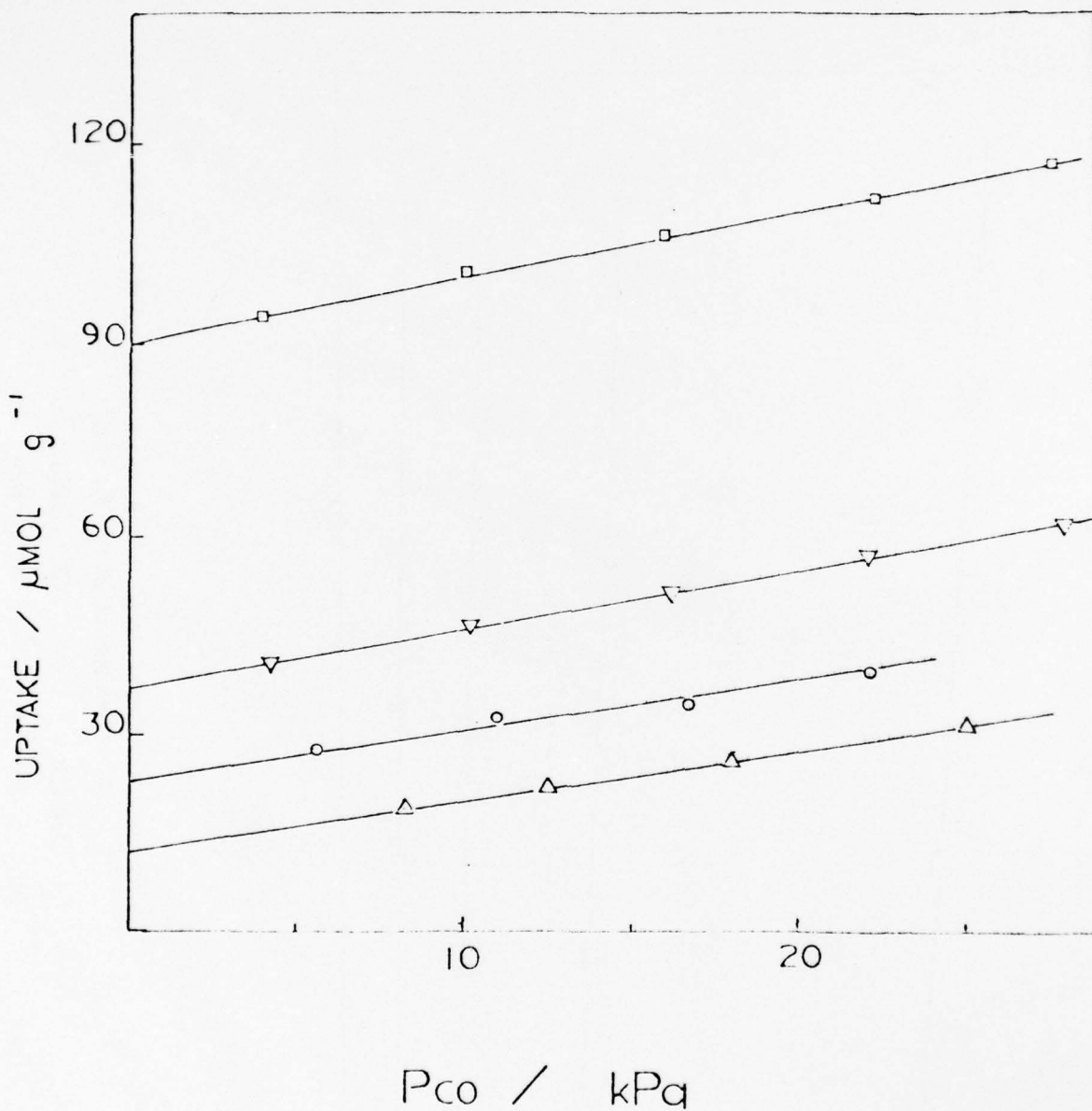
Fig. 2.8.b.   CO adsorption isotherms at 295 K,
after evacuation at 573 K for 1 h

☐   L(20:80)   ○   L(60:40)

▽   L(40:60)   △   L(80:20)

Fig. 2.8 c. Typical O_2 adsorption isotherms at 295 K

□ H(20:80), after evacuation at 573 K
△ H(60:40), after evacuation at 573 K
▲ H(60:40), backsorption isotherm

P_{O_2} / kPa

UPTAKE / μmol g^{-1}
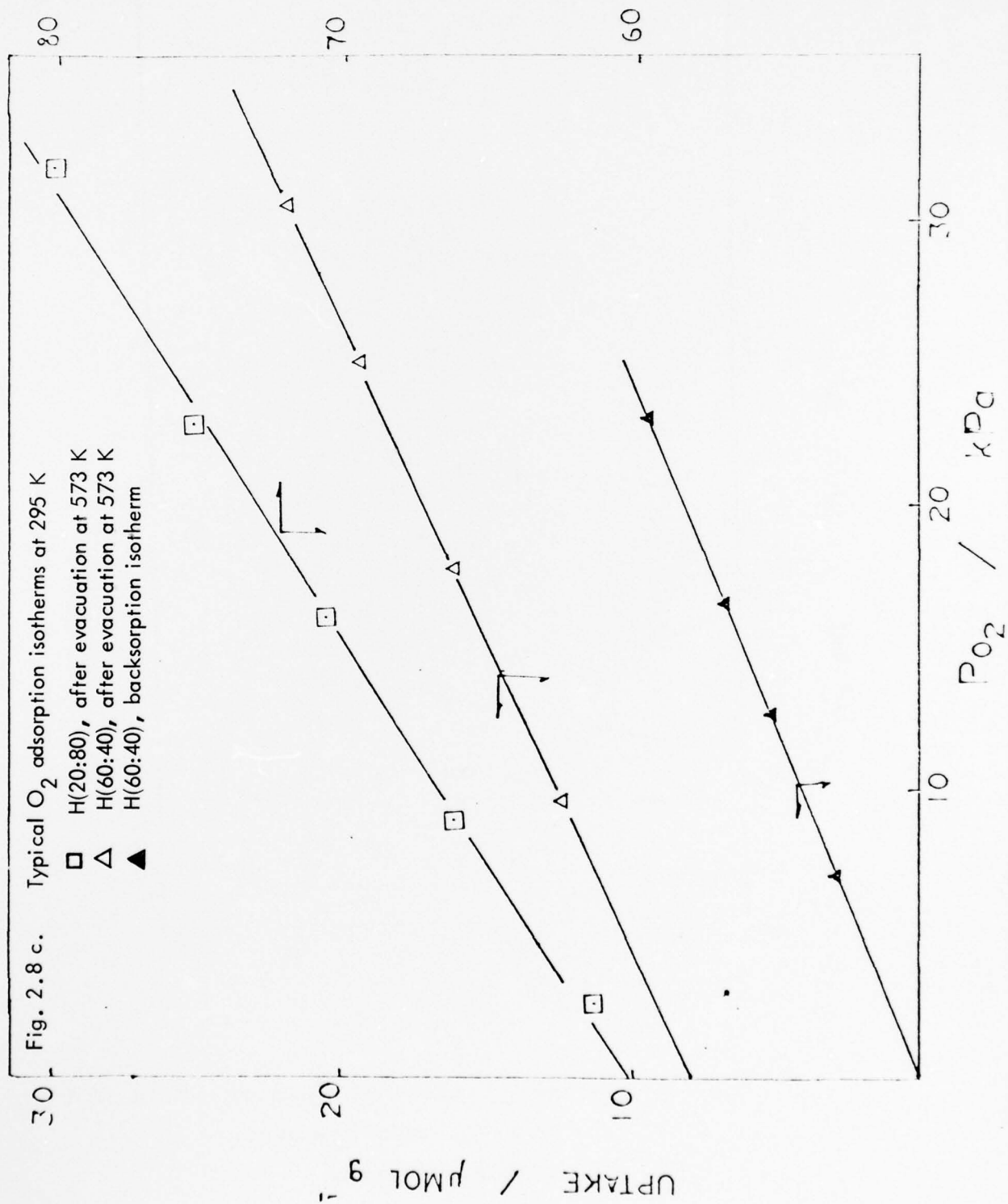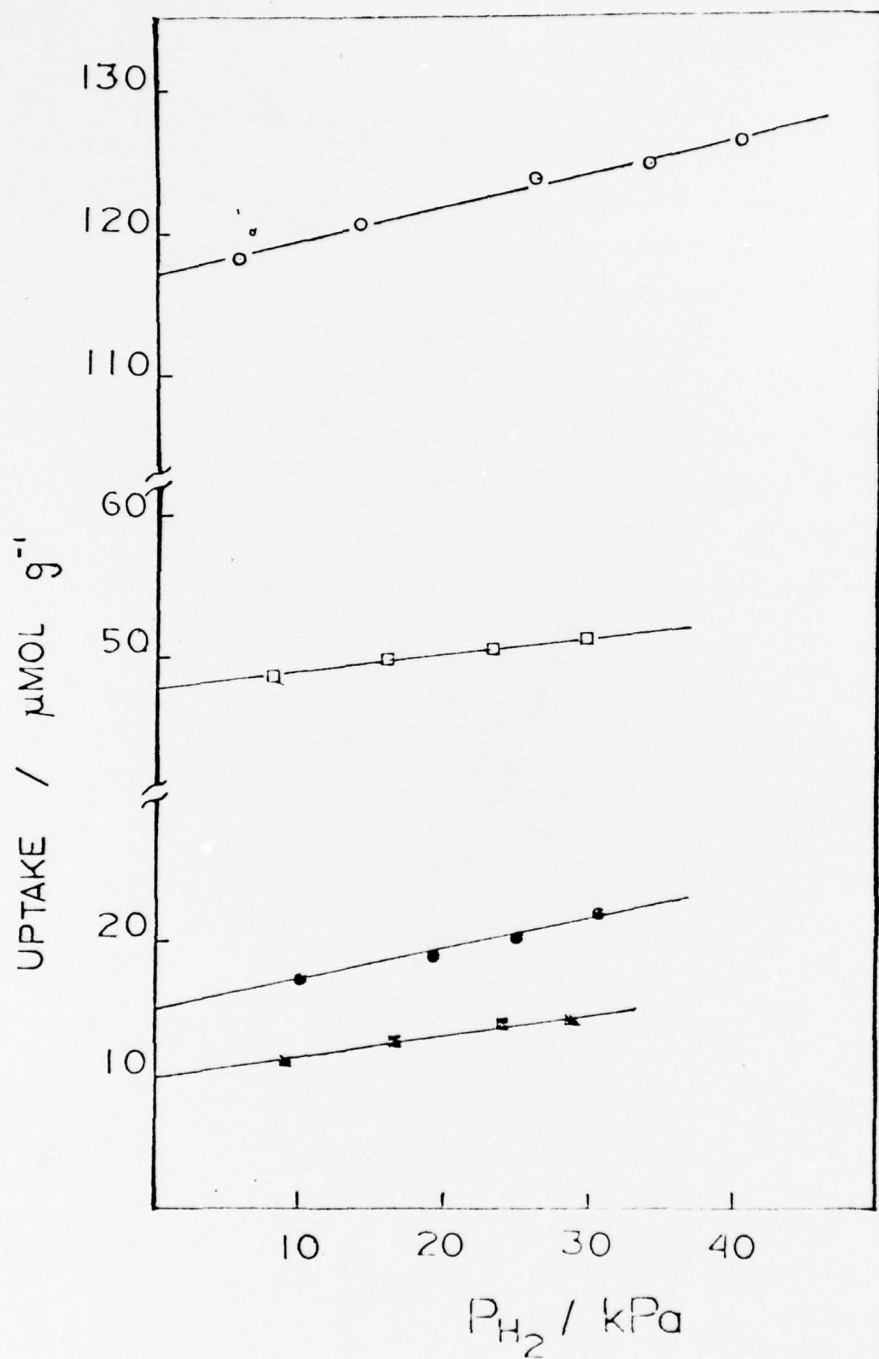
Fig. 2.8 d. Typical H_2 titration and backsorption isotherms at 295 K

    ○   L(20:80), titration total uptake

    ●   L(20:80), backsorption

    □   L(40:60), titration total uptake

    ■   L(40:60), backsorption

Table 2.4   Adsorption and titration data at 295 $\pm$ 2 K

Sample	Gas uptake / μmol g^{-1} *				
	$H_2(ad)$	CO	O_2	$H_2(tit)$	$H_2(back)$.
L(0:100)	--	79.5	41.0	116.5	17.5
L(20:80)	30.0	75.0	32.0	93.5	14.8
L(40:60)	10.5	27.0	11.8	38.0	8.0
L(60:40)	4.0	17.0	7.8	28.0	4.5
L(80:20)	1.8	7.3	3.5	--	1.7(5)
H(0:100)	53.0	84.0	55.5	166.0	38.5
H(20:80)	55.8	98.0	60.0	188.0	26.8
H(40:60)	19.5	52.0	34.0	97.5	19.5
H(60:40)	4.2	24.0	13.8	35.5	5.5
H(80:20)	--	9.3	2.5	7.5	1.7
ME(20:80)	127.5	273.0	--	--	70.0
ME(52:48)	25.0	83.5	--	--	19.2

* uncertainty : $\pm$ 0.5 μmol g^{-1}

Table 2.5   Uptake of gas per Pd atom and ratio of uptakes at 295 $\pm$ 2 K

Sample	H(tit)/3.Pd	O/Pd	CO/Pd	H/Pd	H/O	CO/O	H(tit)/O
L(0:100)	0.59	0.63	0.61	--	--	0.97	2.84
L(20:80)	0.63	0.64	0.76	0.61	0.95	1.19	2.95
L(40:60)	0.37	0.35	0.40	0.31	0.88	1.14	3.20
L(60:40)	0.34	0.28	0.31	0.14	0.55	1.10	3.40
L(80:20)	--	0.16	0.16	0.08	0.51	1.00	--
H(0:100)	0.51	0.51	0.39	0.45	0.95	0.76	2.99
H(20:80)	0.64	0.61	0.50	0.57	0.93	0.82	3.13
H(40:60)	0.41	0.43	0.33	0.25	0.57	0.76	2.86
H(60:40)	0.26	0.30	0.26	0.09	0.30	0.87	2.57
H(80:20)	0.10	0.10	0.19	--	--	--	3.13
ME(20:80)	--	--	0.48	0.45	--	--	--
ME(52:48)	--	--	0.38	0.23	--	--	--

4. Discussion

Effect of Dioxygen on the Decomposition of $[Au(en)_2]^{3+}$

It was rather surprising that controlled oxidation led to the formation of large particles of Au while similar oxidation of precursors led to increased dispersion for Pt and Pd (1, 2, 12). Since oxidation of reduced H(20:80) and H(40:60) did not bring about a growth of metal particles as observed from the x-ray line broadening, formation of large Au particles probably occurred in parallel to the decomposition of the adsorbed $[Au(en)_2]^{3+}$ and not after the metal aggregates were formed.

The following may be a possible explanation of the effect of oxidation. The formation of Au_2O_3 has been reported on heating $Au(OH)_3$ in air at 313 K (3). Assuming a similar oxide of Au is being formed when $[Au(en)_2]^{3+}$ is being decomposed in flowing dioxygen, the ionic forces that hold the Au nucleus to the surface adsorption site may no longer exist. Therefore, a gold oxide species, such as Au_2O_3, may be a mobile species. This is eventually decomposed to Au at higher temperatures (e.g. starting at 333 K, Au_2O_3 decomposes to Au and dioxygen in dioxygen at about atmospheric pressure (13,14)). Hence this species furnishes a pathway for the agglomeration of Au when $[Au(en)_2^{3+}$ is decomposed in dioxygen.

Pre-oxidation of the precursors before reduction will increase the dispersion of Pd, but decrease the dispersion of Au drastically. Hence, in the preparation of a Au-Pd alloy from the precursor, direct reduction by dihydrogen was used. This method suggests an important consideration in the preparation of an alloy catalyst by ion-exchange: the relative mobilities of the adsorbed complexes or their partially decomposed derivatives should be roughly equal so that alloy particles of uniform composition can be formed.

-109-

Qualititative Evidence for Au-Pd Alloy Formation

Figs.2.9a to 2.9d show that the amounts of dihydrogen, dioxygen and carbon monoxide that are strongly held on the Au-Pd samples per mole of Pd fall rapidly as the Au to Pd ratio increases. If normalized against total quantity of metal, the fall would have been more drastic. However, if we assume that surface Au atoms do not adsorb gases strongly, it is more reasonable to normalize the amount taken up to Pd atoms only.

The dispersion of a metal prepared by the same method on the same support generally will not decrease with decreasing metal loading (1,2,15). Note that if we consider samples in the L series (similarly in the H series), the total metal loading has been kept constant. Thus, as the Au contents increase, the Pd contents decrease. Thus the fall of gas uptake per mole of Pd, which can be taken as a measure of the dispersion of Pd, indicated that the Au-Pd associative interaction, i.e., alloying had occurred.

The decrease in gas uptake may be due to several reasons.

First, the size of the alloy particles formed increased with Au to Pd ratio since Au had a larger tendency to agglomerate than Pd (1).

Second, the number of gas molecules taken up by a surface Pd atom was affected by alloying with Au.

Third, surface enrichment of Au on Au-Pd alloy particles caused a decrease in the number of surface Pd atoms.

To separate the above three effects is a non-trivial problem.

Estimation of Particle Size

Pd Dispersion

The stoichiometry of CO adsorbing on a metal surface is defined as the ratio of the number of CO molecules taken up by the surface to the number of surface metal atoms. The amount of CO strongly held has been used to determine the dispersion of Pd. A stoichiometry of one yields values of dispersion in good agreement with those determined by other techniques such as dihydrogen adsorption, dioxygen adsorption,

Fig. 2.9a Gas uptake as a function of total alloy composition H/Pd

□ H(x:y)   O L(x:y)   △ ME(x:y)

-111-

Fig. 2.9 b   Gas uptake as a function of total alloy composition 0/Pd
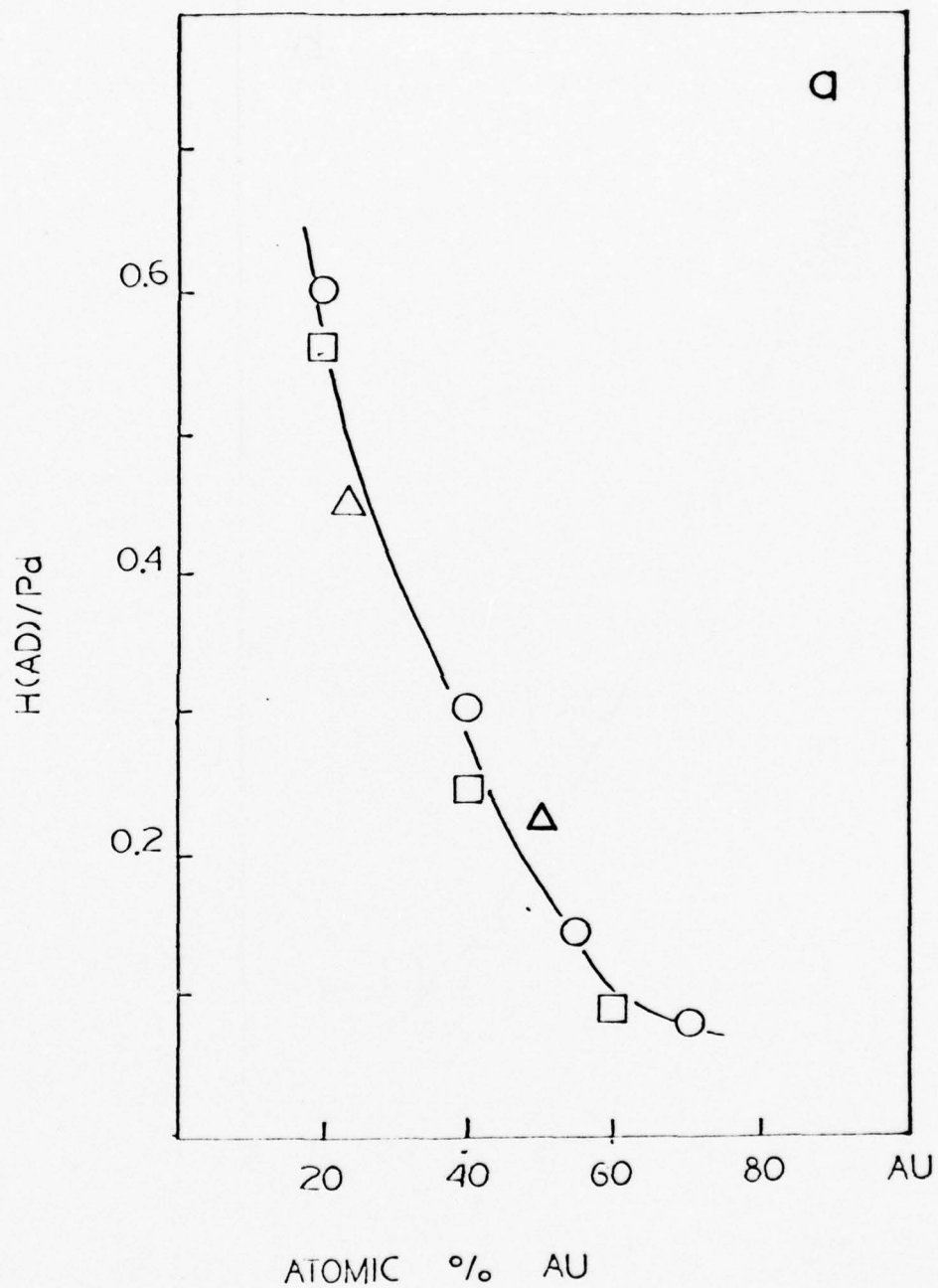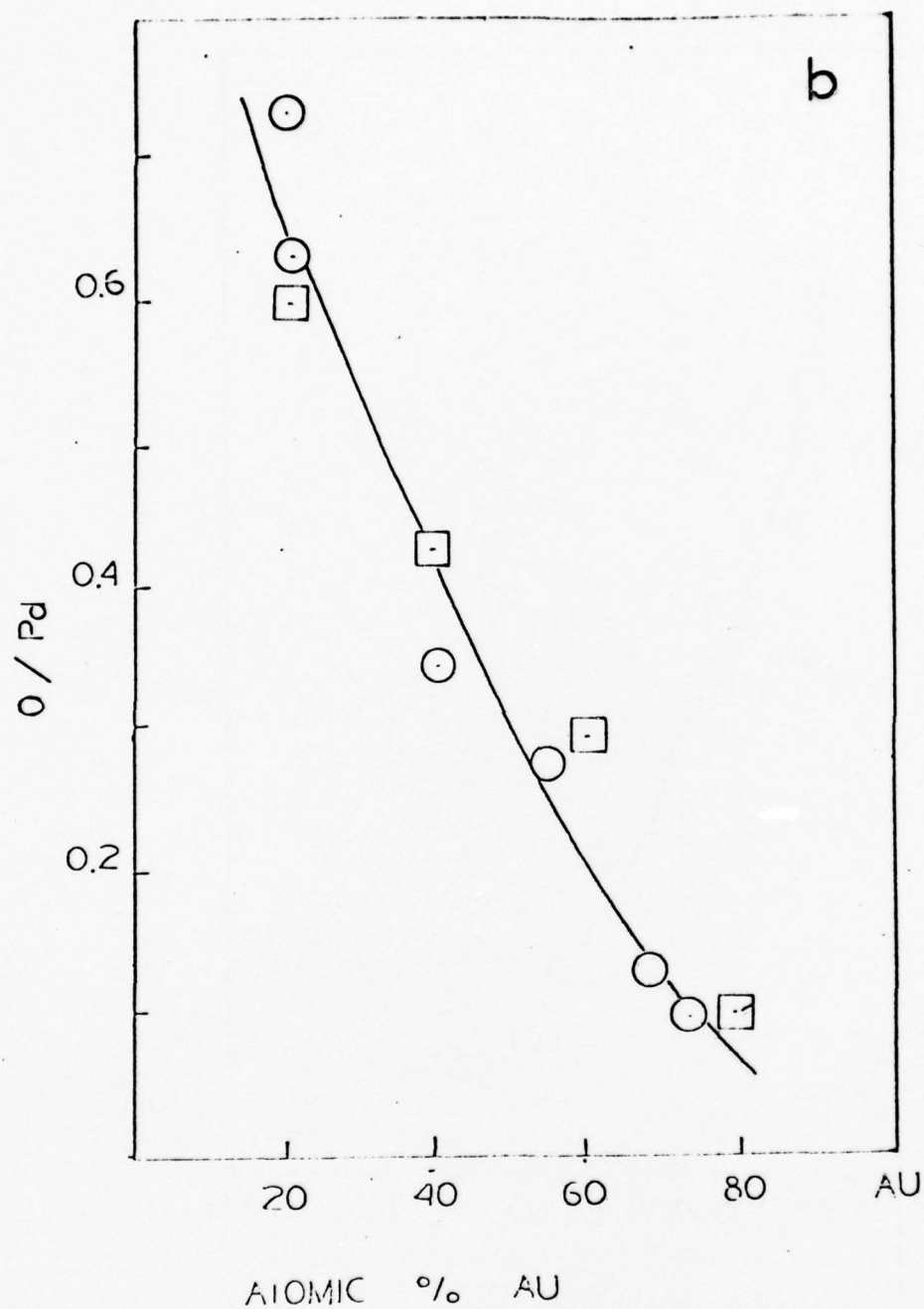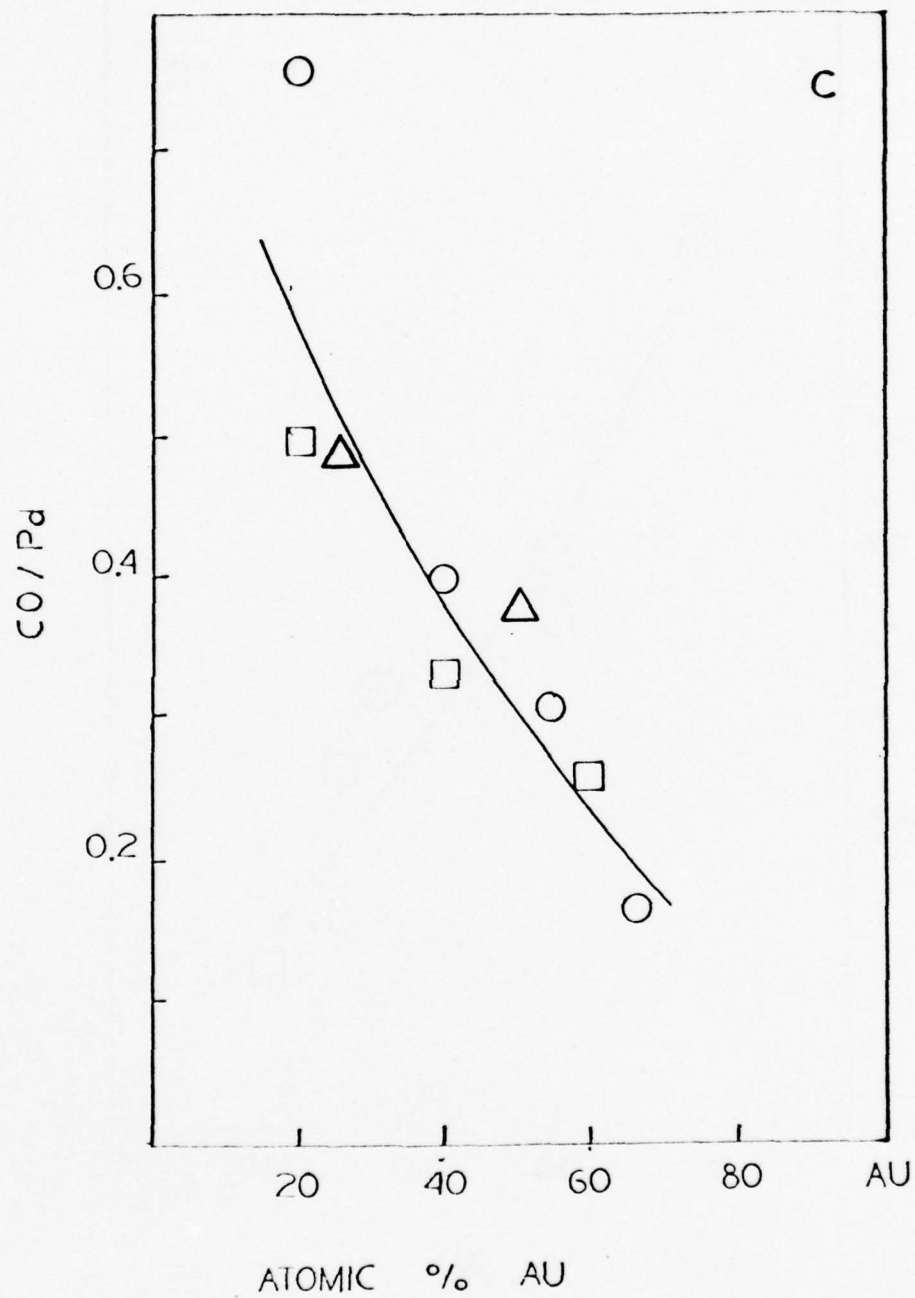
□ H(x:y)   ○ L(x:y)

Fig. 2.9 c   Gas uptake as a function of total alloy composition CO/Pd
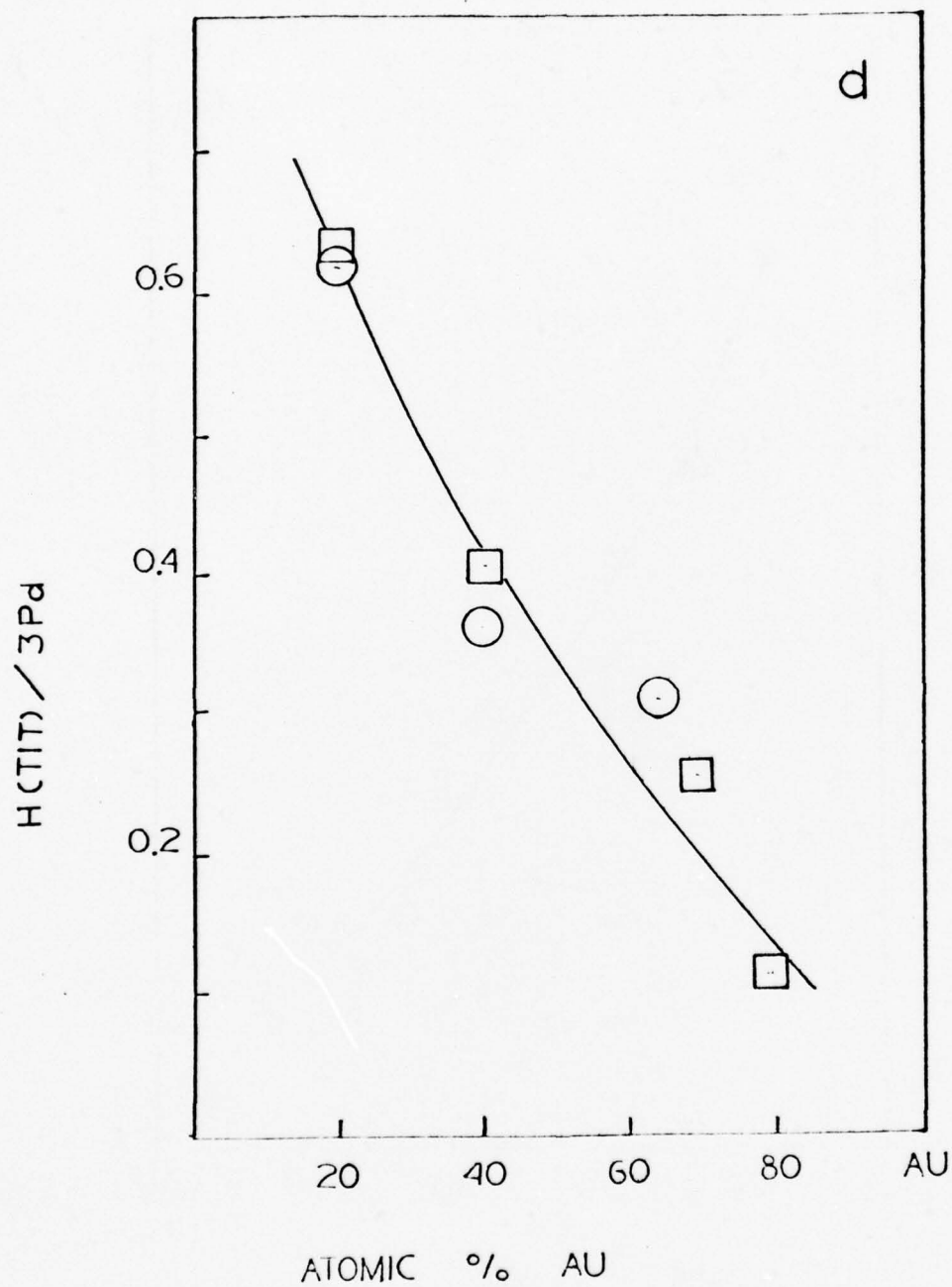
☐ H(x:y)   ◯ L(x:y)   △ ME(x:y)

Fig. 2.9 d   Gas uptake as a function of total alloy composition

H(titration) / 3.Pd

☐ H(x:y)   ◯ L(x:y)

dihydrogen titration of oxygen pre-adsorbed surfaces, and x-ray line broadening for small Pd particles (16). However, on bulk Pd such as powders or films, a stoichiometry of 0.6 is favored (17,18). Presumably, the surfaces of small Pd particles have more sites with low coordination numbers that could accommodate a larger number of CO molecules per site. A similar situation exists for CO adsorption on Ru (19).

The possibility of using CO to adsorb selectively on surface Pd in Au-Pd powders had been demonstrated by Gerberich, et.al. (20). Uptake on CO was used to estimate the total surface area with the following assumptions. First, CO adsorbs only on Pd with a stoichiometry of 0.6. Second, the surface composition is equal to that of the bulk. Comparison of the area deduced from the above method to the surface area determined by the BET method was favorable for all the alloys in this study.

Therefore, in the estimation of Pd dispersion in the alloys prepared in the work, it is reasonable to assume that CO adsorbs only on Pd sites with a stoichiometry of one.

Total Dispersion

To estimate the total dispersion (and hence the particle size) of the alloys, we need a second independent measurement, or the knowledge of their surface composition. There are three good reasons to support that the surface and bulk composition of the alloy particles in this study are similar.

First, for some samples for which x-ray diffraction patterns of the alloys were resolved, the alloy particle sizes were calculated. These values were compared to those determined from CO adsorption. The latter determination assumed that CO molecules strongly held on the Pd surface atoms only with a CO/Pd(surface) ratio of 1 and that the surface composition of an alloy was equal to the bulk. Table 2.3 shows that the two sets of values are in good agreement.

Second, since the heats of vaporization of Au and Pd are approximately equal, current theories on surface composition predict that the surface and the bulk compositions will also be approximately equal for Au-Pd alloys in vacuo.

Third, consider an Au-Pd alloy with an overall composition 50% in Au. Let 50% of the total Pd to be on the surface. Now, if instead of 50% of the total Au atoms on the surface as predicted by theories, 75% of the total Au atoms are on the surface, the surface composition will be 60% in Au instead of 50% in Au. This composition is not very much different from the overall composition. This is an effect due to the small particle size. A more thorough treatment of this effect has already been considered by Williams (21).

Therefore, by assuming that the surface composition of an Au-Pd alloy to be equal to the bulk composition, the total dispersion is equated to the Pd dispersion estimated by CO adsorption. Using these dispersion estimates, the particle size of these alloy aggregates can be deduced. It is found to increase from 1.5 nm to 5.0 nm from Au lean to Au rich alloys.

REFERENCES

1. Benesi, H. A., Curtis, D. M., and Studer, H. P., J. Catal. 10, 328 (1968).

2. Boudart, M., and Hwang, H. S., J. Catal. 39, 44 (1975).

3. Johnson, B. F. G., and Davis, R., "Comprehensive Inorganic Chemistry," Vol. 3, edited by Bailar, J. C., Jr., et al. Pergamon Press, Oxford, 1973.

4. Mason, W. R., and Gray, H. B., J. Am. Chem. Soc. 90, 5721 (1968).

5. Sulcek, Z., Vasak, M., and Dolezal, J., Microchemical Journal 16, 210 (1971).

6. Block, B. P., and Bailar, J. C., Jr., J. Am. Chem. Soc. 73, 4722 (1951).

7. Hwang, S. H., Ph.D. Dissertation, Stanford University, Chapter 3, Stanford, 1975.

8. Dalla Betta, R., Ph. D. Dissertation, Stanford University, Appendix B, Stanford, 1973.

9. Klug, H. P., and Alexander, L. G., "X-ray Diffraction Procedures," Chapter 9, Wiley, N. Y., 1954.

10. Hanson, F. V., Ph.D. Dissertation, Stanford University, Chapter 1, Stanford, 1976.

11. Hair, M. L., "Infrared Spectroscopy in Surface Chemistry," Dekker, 1967.

12. Dalla Betta, R., and Boudart, M., reprint no. 96, in "Proceedings of the Fifth International Congress on Catalysis," North Holland Publishing Co., N. Y., 1973.

13. Veratin, U. D., et al., "Thermodynamic Properties of Inorganic Substances, Handbook," (Russ), Atomizdat, 1965.

14. Watt, G. W., Klett, D. S., Inorg. Chem. 5 (7), 1278 (1965).

15. See for example, Anderson, J. R., "Structure of Metallic Catalysts," p. 276-285, Academic, N. Y., 1975.

16. Benson, J. E., Hwang, H. S., and Boudart, M., J. Catal. $\underline{30}$, 146 (1973).

17. Hayward, D. O., in "Chemisorption and Reactions on Metallic Films" edited by Anderson, J. R., Academic, New York, 1971 and references therein.

18. Ford, R. R., Adv. in Catal. $\underline{21}$, 51 (1970).

19. Dalla Betta, R., J. Phy. Chem. $\underline{79}$, 2519 (1975).

20. Gerberich, H. R., Cant, N. W., and Hall, W. K., J. Catal. $\underline{16}$, 204 (1970).

21. Williams, F. L., Ph.D. Dissertation, Stanford University, Stanford, 1972.

Appendix I: Preparation and Characterization of $[Au(en)_2]Cl_3$

$[Au(en)_2]Cl_3$ was prepared by the method of Block and Bailar(1).
To prepare 1 g of the complex, about 1 g $HAuCl_4 \cdot 3H_2O$ (Englehard)
was dissolved in 10 cm^3 ethyl ether (Mallinckradt). 1 cm^3 of
ethylene diamine (anhydrous, Fisher) was dissolved in 5 cm^3 of ethyl
ether. The latter solution was added dropwise into the solution of
gold salt. A yellow gummy precipitate was formed. The superlatent
was decanted and the precipitate was dissolved in 1 cm^3 of doubly
distilled water. Upon addition of 10 cm^3 absolute alcohol, white
crystals were formed. The crystals were filtered and washed with
three 3 cm^3 portions of absolute alcohol.

Since salts of gold are light-sensitive, decomposing slowly
to metallic Au, after drying for 1 h by suction, the crystals are
stored in dark vials in a dessicator.

An infrared spectrum of $[Au(en)_2]Cl_3$ prepared showed very
good agreement with the spectra of compounds of the formula
$[M(en)_2]Cl_2$, M = Pd, Pt. The absorption bands are analysed and
compared in Table A (2). A spectrum of the gold salt in KBr disc
is shown in Fig. A.

Ref. 1. Block, B. P., and Bailar, J. C. Jr., J. Am. Chem. Soc.
          73, 4722 (1951).

      2. Watt, G. W., Klett, D. S., Inorg. Chem. 5(7), 127 (1966).

-119-

Table A. <u>Infrared absorption peak position (in cm^{-1}) of</u>
<u>ethylene diamine complexes</u>

$[Pd(en)_2]Cl_2$ [1]		$[Pt(en)_2]Cl_2$ [1]		$[Au(en)_2]Cl_3$ [2]			Assignments [3]
1608	s	1613	s	1600	s		$\delta(NH_2)$
1599	s	1593	s	1550	s		$\delta(NH_2)$
1456	s	1457	s	1450	s	*	$\delta(CH_2)$
1392	w	1391	vw	1390	w		$\omega(CH_2)$
1397	s	1374	s	1365	s		$\omega(CH_2)$
1321	m	1328	m	1320	s		$\omega(NH_2)$
1136	vs	1163	vs	1170	vs		$\omega(NH_2)$
1296	m	1313	m	1310	m	*	$\delta(CH_2)$
1277	s	1279	s	1270	m		(CH_2)
1127	s	1140	s	1140	s		(NH_2)
999	w	1000	w	990	m		(NH_2)

* The peak a 1440 cm^{-1} and the shoulder at 1310 cm^{-1} may be due to residual water.

1. From Ref. 2.

2. Recorded in this study.

3. δ = inplane bending, ω = wagging, $\cdot$ = twisting.

Intensity:

vs = very strong, s = strong, m = medium, w = weak, vw = very weak

-120-
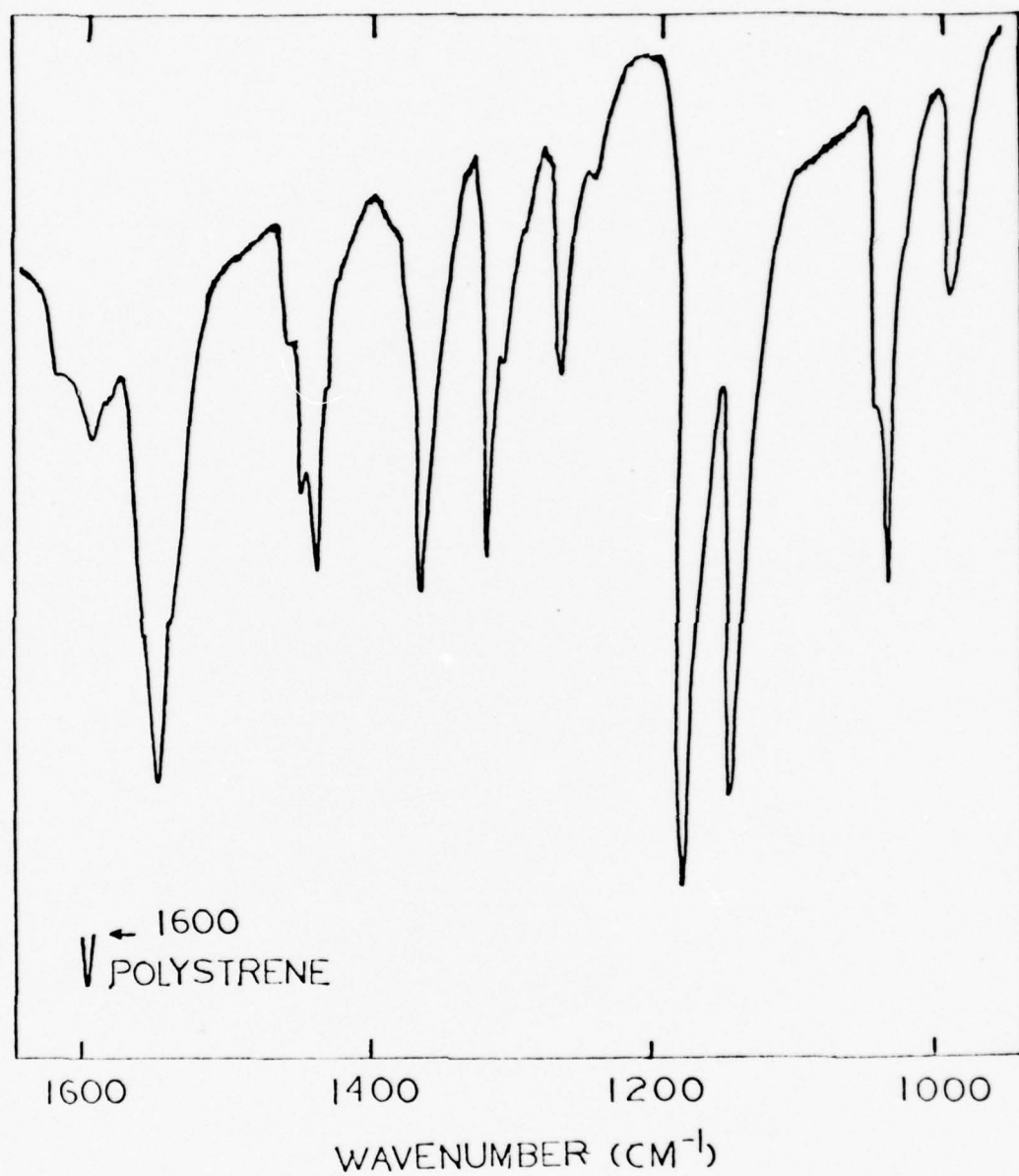
Fig. A   IR Spectrum of [Au(en)$_2$] Cl$_3$ in KBr Disc

APPENDIX II

Purification of Gases

Gas	Source	Purity/%	Further Purification
H_2	Liquid Carbonic	99.93	Pd-diffused
O_2	Liquid Carbonic	99.5	Passed over a Linde 5A molecular trap at 195 K
He	Liquid Carbonic (Grade A)	99.995	Passed over hot Cu wire and then a liquid nitrogen trap
CO	Matheson	99.99	Passed over a Linde 5A molecular trap at 195 K

V. DEVELOPMENT OF ELEVATED TEMPERATURE

ELECTROCRYSTALLIZATION TECHNIQUES

R. S. Feigelson
Director, Crystal Technology
Center for Materials Research

R. C. DeMattei
Research Associate

and

R. A. Huggins
Professor of Materials Science
and Engineering

A. Introduction

The major emphasis of the electrocrystallization phase of this program has been to develop a more sophisticated understanding of the principles involved in the use of molten salt electrochemistry for material synthesis, crystal growth and the preparation of polycrystalline layers of a wide range of materials. Such an in-depth study was designed to lead ultimately to a greater control over both nucleation and growth processes. Little attention had been previously given to this aspect of molten salt electrochemistry and most of the past work reported in the literature on molten salt electrocrystallization concentrated on compound synthesis with the resulting electrodeposits in the form of either powders or tiny crystallites.

During the past few years, we have made significant progress toward our objectives. A number of papers have been published in scientific journals on a variety of topics including the epitaxial deposition of silicon on silicon substrates,[1,2] a theoretical analysis of the rate-controlling process during electrolytic growth and dissolution,[3] and a study of the conditions necessary for stable growth.[4-6] One of the important findings resulting from this work has been that by using an appropriate pulse technique the stable growth rate can be increased by factors of 30-50.[7] Large single crystals of LaB_6 have also been grown for the first time[8] and a potentially important process, the Electrochemical Czochralski Technique (ECT) has been developed.[9] In addition, several phases in the Nb-Ge alloy system have been synthesized from a molten salt bath.

During the past year special emphasis was placed on the synthesis and growth of several new materials including ScB_2, PrB_6, InP and GaP and on further studies of the new ECT technology. The individual programs are discussed separately in the following sections.

B. New Materials and Techniques

1. Introduction

During the first two years, this phase of the program had as its
major goals the development of a sufficiently deep understanding of
the principles involved in molten salt electrocrystallization to allow
the controlled growth of polycrystalline and single crystal deposits and
epitaxial layers. During this period, using the lanthanum hexaboride
(LaB_6) and zirconium diboride (ZrB_2) systems, the effects of deposition
parameters such as voltage, current density and temperature were studied
and their effects on nucleation rate, morphology and deposition efficiency
are now understood. At the same time, a study of crucible and electrode
materials compatible with molten salts was completed. Using this knowl-
edge a new and more sophisticated growth apparatus system was constructed.
This new system allows more precise control of the deposition parameters,
thus leading to better reproducibility. The apparatus is capable of
operating in a stable mode for periods exceeding 300 hours and has rou-
tinely produced clusters of LaB_6 crystals with individual single crystals
as large as 4mm on edge.

With this background firmly established, heavy emphasis was placed
during the early part of this year on seeded growth and the synthesis
of new compounds. Studies were initiated on the scandium and praeseo-
dymium-boron systems and on indium and gallium phosphide.

2. Seeded Growth of Lanthanun Hexaboride (LaB_6)

The logical conclusion of the lanthanum hexaboride studies was the
seeded growth of this material. Seeds were obtained by sectioning a
zone-refined boule of LaB_6 with large grain size. Deposition on a 2 x 3mm
seed for 87 hours at 800°C from the Andrieux type melt[10,3] produced a
well-facetted crystal measuring 4 x 5 x 3mm. Continued deposition on
the same seed at a current density of 20 ma/cm^2 produced a 5 x 6 x 6mm
crystal. The total deposition time was 200 hours.[8] Figure 1 shows
this crystal at two stages of its growth.

With the completion of the seeded growth of LaB_6, this aspect of the
program reached its conclusion. The work with LaB_6 produced an understanding
of the thermodynamic and electrochemical conditions necessary for growth
of a model material by electrochemical crystallization. The emphasis of
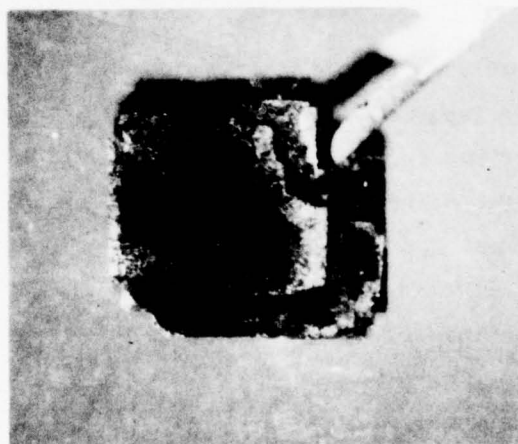this aspect of the program was shifted to new materials.

Figure 1.   Seeded growth, suspended by gold wire ($\sim$ 8X)

(a) After 87 hours of growth

(b) After 200 hours of growth

3. Scandium Borides

The study of the scandium-boron system represented an extension of the previous work on LaB_6 and ZrB_2. Scandium belongs to the same group of elements (III-B) as lanthanum and yttrium, both of which form borides which have been synthesized electrochemically;[10] thus it appeared to be a suitable element for study. While several diborides have been synthesized electrochemically, scandium diboride (ScB_2) has not. The study of this material would, therefore, provide an opportunity to apply the knowledge gained in the LaB_6 phase of the program to a new system.

The first experiments utilized a melt similar to that used for LaB_6[10,3] with the lanthanum oxide replaced by scandium oxide (Sc_2O_3). Melts with scandium to boron ratios of 1:31 to 1:1.8 were electrolyzed. In all cases multiphase deposits were obtained. Analysis of these deposits showed that while scandium and boron were being codeposited no definite compound could be identified.

The Andrieux-type melt suffers from the drawback that one of the electrochemically active species (B_2O_3) also serves as part of the solvent system. This precludes the current vs. voltage (I-V) characterization of the individual species. To facilitate the further study of the scandium-boron system, a change was made to a Flinak- (LiF, KF, NaF eutectic) based melt. The I-V characteristics of both B_2O_3 and Sc_2O_3 solute were investigated. The decomposition potentials of both materials were found to be in the range of 2.0 to 2.5 volts and varied predictably with concentration changes. Electrolysis of melts containing B_2O_3 and Sc_2O_3 produced clusters of black crystals containing both scandium and boron but no identifiable scandium boride compound. Because a prohibitive amount of time and effort was considered necessary to provide a complete understanding of this system, the scandium-boron project was terminated.

4. Praeseodymium hexaboride (PrB_6)

With the termination of the scandium-boron studies, effort was concentrated on the praeseodymium-boron system. The compound PrB_6 had been synthesized, but not by electrochemical means. Praeseodymium itself belongs to the lanthanide series of rare earths and chemically should behave much the

same as lanthanum. In addition, PrB_6 would also be of interest for Moss-
bauer studies, if it could be grown in thin layers.

The melt chosen for the deposition was again a variation of the
Andrieux melt used for LaB_6.[10,3] It contained equimolar amounts of B_2O_3,
LiF and Li_2O with 0.7 mole% of praeseodymium oxide (Pr_6O_{11}).   Initial
experiments using this melt with a gold wire cathode produced PrB_6 crystals
as large as 1mm on a side after a growth time of 3 hours at 800°C.
By decreasing the amount of Pr_6O_{11} in the melt, praeseodymium-
deficient material could be produced. In general this material was
darker colored and the average cube size was smaller than in the stoichiometric
compound.

For potential Mössbauer studies, layers of controlled weight per unit
area are necessary. The ability to accomplish this would further test
the control of deposition parameters during electrolysis. The first layers
were grown on 0.05 mil nickel substrates. Due to embrittlement of the
substrates caused by boriding of the nickel, most of these layers were lost.
Changing to graphite substrates solved this problem and suitable, poly-
crystalline deposits ranging from 0.5 to 1.7 mg/cm^2 were made.   (See Figure 2)
The graphite substrates could be removed by heating in air at 700°C leaving
the PrB_6 unaffected.

This phase of the program reached its goals of electrochemically syn-
thesizing large PrB_6 crystallites and developing the means of depositing
layers of controlled weight per unit area and was subsequently discontinued.

5.   Gallium and Indium Phosphide

For many years worldwide efforts of major proportion have centered
around the preparation of semiconductor materials including III-V, II-VI
and mixed ternary compounds and alloys for electronic and optical
applications. Most of the techniques which have been used to produce bulk
single crystals or layers of these compounds involve temperature control,
complicated equipment and operation at high temperatures.

Several years ago some preliminary experiments were carried out to
synthesize and grow epitaxial layers of some of these semiconducting
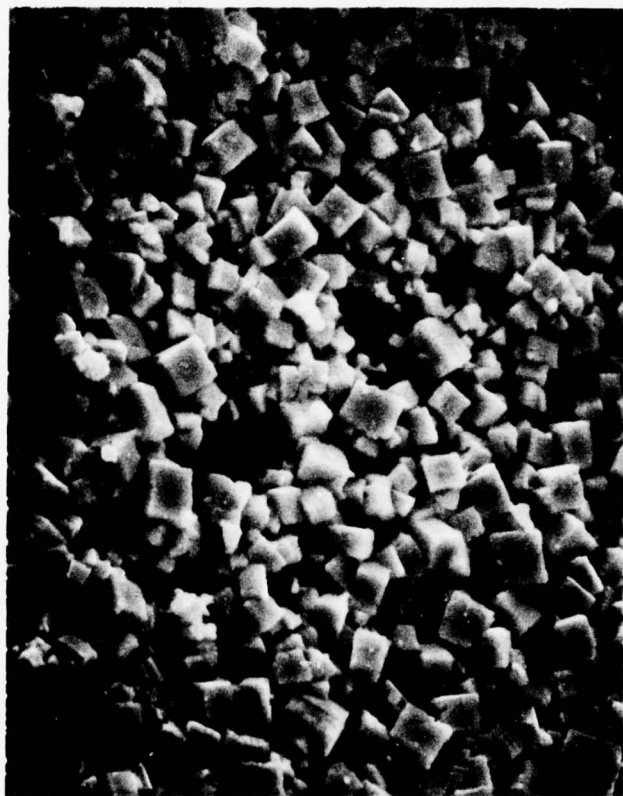materials by electrocrystallization techniques. Cuomo and Gambino[11]

Figure 2. .5 mg/cm^2 deposit of PrB$_6$ on graphite substrate. Crystallites 1 – 5μ on a side. ($\sim$ 2000X)

studied the growth of Ga and In phosphides while Yamamoto and Yamaguchi[12] studied ZnSe preparation by molten salt electrocrystallization. Very little effort by these authors went into developing the process to a level capable of producing useful material competitive with that produced by other techniques. The electrochemical process does, however, offer several potential advantages over more conventional techniques since: (1) the technique is isothermal, depending only on applied potential and current to control growth rate; (2) the technique requires relatively low temperatures, thus, decomposition problems can be avoided and, in principle, the defect concentration can be reduced; (3) the equipment is simple and inexpensive; (4) starting materials can be relatively inexpensive since many impurities can be removed by electrochemical purification techniques; (5) electrochemical, as well as mechanical, techniques can be used to enhance growth rates; (6) deposit uniformity can be controlled by cell design and (7) dopants can be introduced and their concentration controlled electrochemically. This phase of the program has as its principal objective the synthesis, growth and characterization of some commercially important semiconductor compounds, in particular Ga and In phosphide. It will lead to the development of techniques which can produce semiconductor materials with different and perhaps higher quality than now produced by conventional techniques.

The first experiments in this program concerned the growth of InP, since this material is of current interest for solar cell application. While Cuomo and Gambino[11] gave only sketchy results on the method of growing this compound, they did indicate that InP could be produced from a sodium metaphosphate ($NaPO_3$) melt. Using a melt consisting of $NaPO_3$ (73.7 mole %), indium oxide (In_2O_3, 9.1 m/o) and sodium fluoride (NaF, 18.2 m/o), InP was produced electrochemically at 800°C. However, large deposits of salts were found in the cooler regions of the growth apparatus indicating volatilization of one or more of the melt components. Subsequent thermo-gravimetric analysis of the melt constituents showed that In_2O_3 has an appreciable vapor pressure at 800°C, which would lead to premature depletion of this species in the melt. Possible solutions to this problem involve using a lower melting eutectic or substituting a less volatile In-containing compound for the In_2O_3.

In order to facilitate the studies of the phosphate systems, emphasis was shifted to the GaP system. This system was more attractive because gallium oxide (Ga_2O_3) is less volatile than In_2O_3 and because Cuomo and Gambino[11] have presented some limited results on the growth of GaP from a low melting chloride eutectic [60 m/o lithium chloride (LiCl) – 40 m/o potassium chloride (KCl)]. The use of a melt not based on a meta-phosphate also allowed the investigation of the electrochemically active species. Figure 3 shows the I-V characteristics of (1) $NaPO_3$, (2) Ga_2O_3 and (3) $NaPO_3$ and Ga_2O_3. These curves show that (1) phosphorous deposition begins at ~0.85 volts, (2) gallium at ~1.8 volts and (3) GaP at ~2.0 volts. It is interesting to note that in curve 3 there is no indication of phosphorous deposition below 2.0 volts. This indicates that some reaction occurs involving the phosphorous and gallium containing species which suppresses the production of phosphorous.

The high residual current in curve 2, Figure 3, was traced to iron impurities in the melt which came mainly from the chlorides. By electro-lysizing the melt for successive 24-hour periods at successively higher potentials and taking I-V curves after each electrolysis (Figure 4), it was found that iron could be effectively removed by electrolysis at 1.3 volts for a 48-hour period.

These early studies culminated in the growth of layers of GaP on silicon. These layers are up to 1 mm in thickness and work is proceeding on the characterization and on improvements in the quality of the deposits.
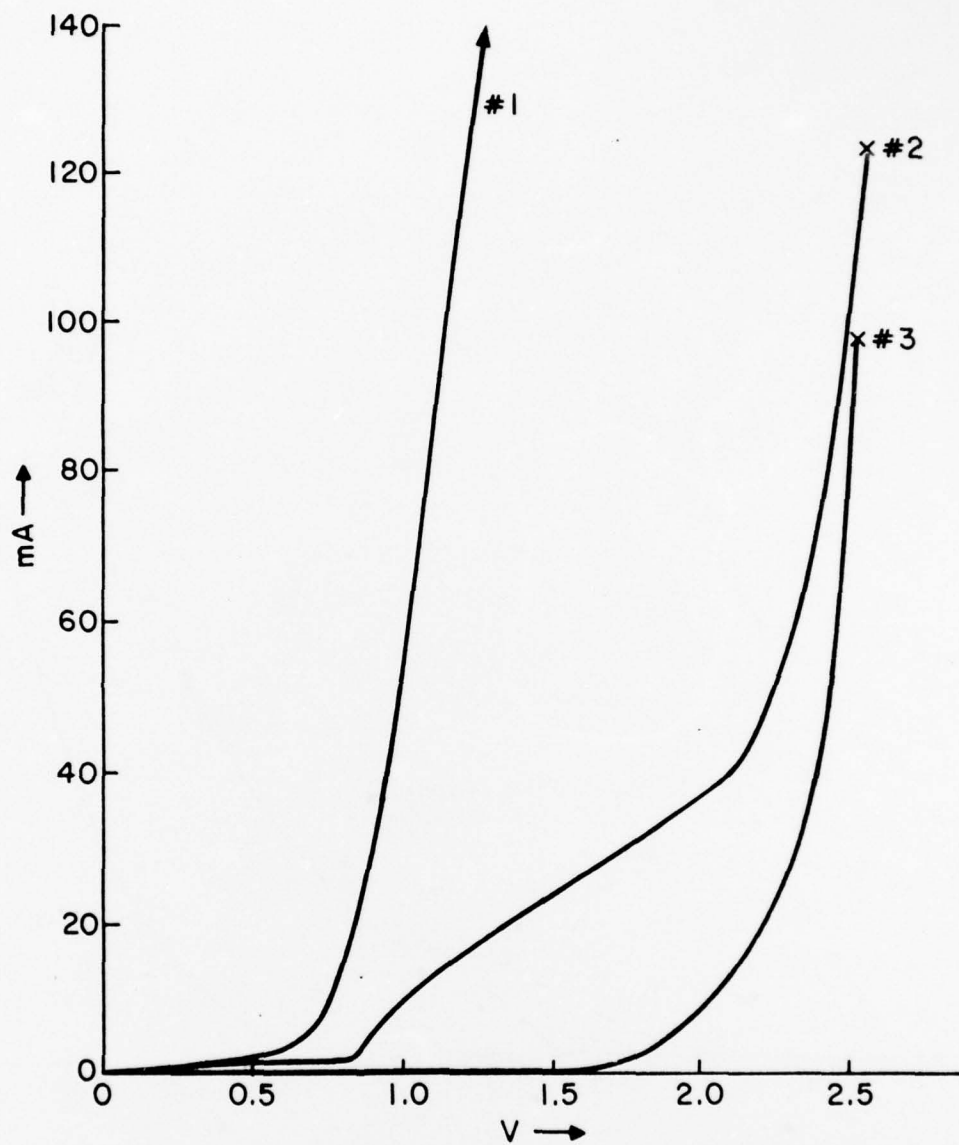
Figure 3. I-V characteristics

Curve #1 $1.2LiCl-.8KCl-.1NaPO_3$ (moles), 600°C

Curve #2 $1.2LiCl-.8KCl-.05Ga_2O_3$, 850°

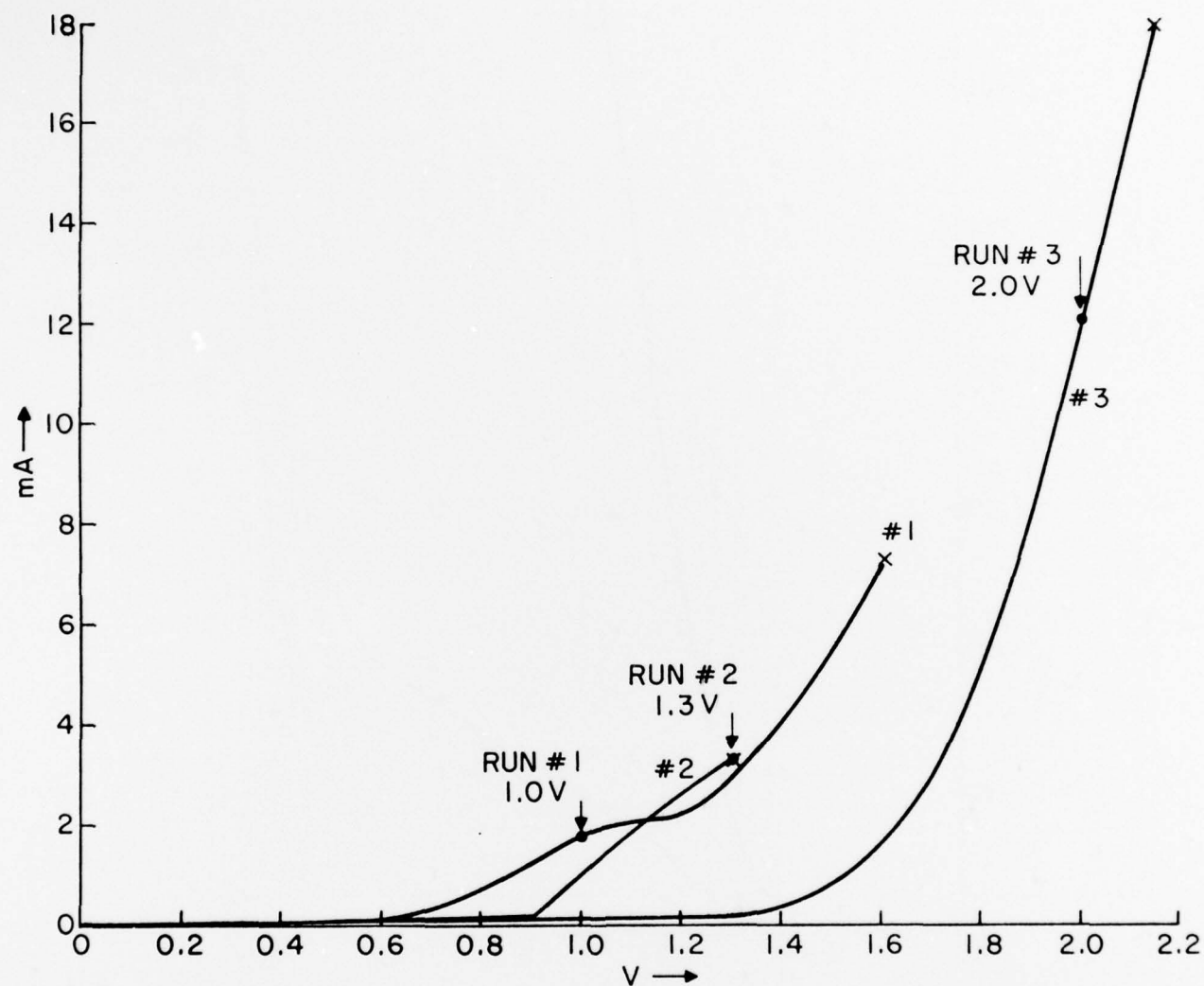Curve #3 $1.2LiCl-.8KCl.-.1NaPO_3-.05Ga_2O_3$, 650°

Figure 4. I-V characteristics vs time for

1.2LiCl-.8KCl-.1NaPO$_3$-.05Ga$_2$O$_3$ (moles)

Curve #1   after 0 hours electrolysis
Curve #2   after ~24 hours electrolysis
Curve #3   after ~48 hours electrolysis

C. Rate-determining Processes in Electrochemical Crystallization

The growth of a crystal is a complicated process involving both diffusional and kinetic attachment steps. In electrochemical crystallization other factors may also become important. By monitoring the current - overpotential behavior of the system, the rate-determining process in an electrochemical reaction can be found. This technique has been applied to two systems - the growth of sodium tungsten bronze (Na_xWO_3) and lanthanum hexaboride (LaB_6).

The model used is an analogy between crystal growth from solution and the flow of current in a circuit.[3] The current-voltage relation in electrocrystallization may be written

$$\Delta V = V - V_d - IR$$

where V is the applied voltage, V_d the decomposition potential, I the total current and R represents the various impedances present in electrocrystallization. The impedances will, in general, be non-ohmic. Comparison with a general expression for the linear growth rate in solution[13] gives a means of identifying the sources of these impedances and their dependence on ΔV. Using this analogy, the total resistance of the system may be written

$$R = R_{vd} + R_{ct} + R_{ik}$$

where vd refers to volume diffusion, ct to charge transfer and ik to interface kinetics. Further analysis indicates that R_{vd} will have ohmic behavior; R_{ct} may, in the simplest case, be expressed by the Butler-Volmer equation, although the actual relationship may be extremely complex; and R_{ik} has linear or non-linear character depending on the nature of material and the effective supersaturation.

The model was applied to two systems: sodium tungsten bronze (Na_xWO_3) and lanthanum hexaboride (LaB_6). In the case of the Na_xWO_3, the plots of current versus overpotential (η) were explained by a combination of volume diffusion and interface kinetics. (See Figure 5.) The data for LaB_6 were not as readily explained, but were shown to be due to a combination of interface kinetics and charge transfer reactions. (See Figure 6.)

This model is capable of explaining all the available resistance data in electrochemical crystallization from molten salts. Further tests of the model will be possible as more data becomes available.
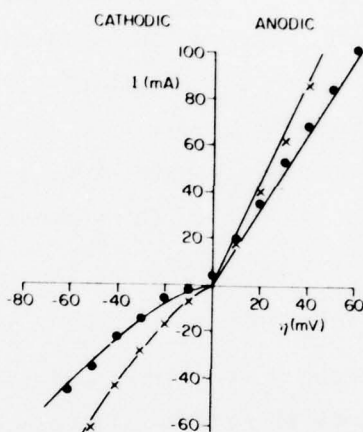
Figure 5. Variation of current with overpotential for tungsten bronzes: (o) $Na_{0.61}WO_3$: (X) $Na_{0.73}WO_3$. The cathodic curves are of the form $R = P_{vd} + BI^{-\frac{1}{2}}$ where $BI^{-\frac{1}{2}} = R_{ik}$
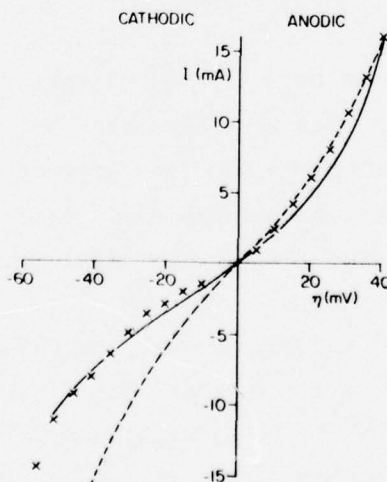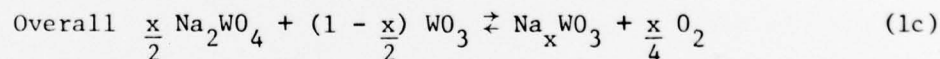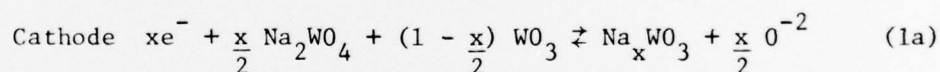

Figure 6. Variation of current with overpotential for LaB_6: (X) experimental points; (- - -) $I = 7.36 \sinh (3.5 \eta F/RT)$ which represents an interface kinetics type impedance; (-·- -) $I = 2.59 [\exp (4.35 \eta F/RT - \exp (-2.65 \eta F/RT)]$ which represents a complex, non-symetric charge transfer reaction.

-135-

D. Continuous Growth and ECT

1. Introduction and Summary of Results to Date
        Since electrochemical crystallization is a Faradaic process,
material is deposited at the growth interface at a controlled rate.
This is similar to the condition necessary for stable growth using the
Czochralski technique. In principle, therefore, it appeared likely
that electrochemical crystallization and crystal pulling could be
combined. Since such a technique would be isothermal the diameter of
the growing crystal should depend only on current and pull rate.
Effort over the last two years has led to the development of
the Electrochemical Czochralski Technique (ECT).[9,14]

        The feasibility of ECT has now been conclusively demonstrated
using sodium tungsten bronze (Na_xWO_3, $0.1 < x < 1$) as a model compound.
This well-characterized compound[15-23] can be synthesized in its cubic
phase ($0.38 < x < 0.9$) at the cathode of an electrochemical cell over
a melt composition range 5-58 m/o tungstic oxide (WO_3) - sodium
tungstate (Na_2WO_4) according to the reactions:

$$\text{Cathode} \quad xe^- + \frac{x}{2} Na_2WO_4 + (1 - \frac{x}{2}) WO_3 \rightleftarrows Na_xWO_3 + \frac{x}{2} O^{-2} \qquad (1a)$$

$$\text{Anode} \quad \frac{x}{2} O^{-2} \rightleftarrows \frac{x}{4} O_2 + xe^- \qquad (1b)$$

$$\text{Overall} \quad \frac{x}{2} Na_2WO_4 + (1 - \frac{x}{2}) WO_3 \rightleftarrows Na_xWO_3 + \frac{x}{4} O_2 \qquad (1c)$$

        Numerous crystals have been grown using 25 m/o WO_3 - Na_2WO_4
melts ($Na_{0.82}WO_3$) at 750°C with <111> oriented seeds in an apparatus
designed for pulling under a controlled atmosphere. These crystals
exhibited a three-fold axial symmetry with convex sides; and, unlike
normal Czochralski growth, the interface region was facetted with well-
developed {100} planes. The cross section of these crystals was
controllable and depended only on the current and pull rate. This

-136-

dependence follows the relation:

$$d_{[111]} = \left[\frac{M\varepsilon}{nF\rho} \frac{I}{0.75(dy/dt)} \right]^{1/2} \tag{2}$$

where $d_{[111]}$ is the distance across the side of the crystal, M the molecular weight of the depositing species, ε the faradaic efficiency (approximately 0.92 for $Na_{0.82}WO_3$), I the total current, n the number of electrons transferred per depositing unit, F Faraday's constant, ρ the density of the crystal and dy/dt the pull rate. Attempts to grow along the other major directions (<100> and <110>) with the same degree of control were not successful. Crystals grown in these directions widened uncontrollably owing to the inclination of the fast growth direction (<111>) to the pulling axis. Eventually these crystals lost contact with the melt. Preliminary experiments using a mechanical constraint to control lateral growth indicated that we may be able to grow <100> or <110> oriented crystals in this manner.

Seed rotation was shown to have a beneficial effect on growth stability up to about 32 rpm. In this region the relation between maximum stable pull rate and rotation rate (ω) in rpm may be expressed as

$$dy/dt = 2.25 + K\omega^{1.17} \tag{3}$$

where K is a constant. Above 48 rpm, the maximum pull rate increased three-fold, but the sides of the crystal became convex. This behavior is believed to be due to flow separation at the interface.

Small temperature changes ($\pm$ 10°C at 750°C) had no visible effect on the growing crystals. Larger changes (+ 50°C) caused a visible decrease in the deposition rate and the formation of a grey, powdery tungsten deposit due to the reaction

$$6Na_xWO_3 \rightleftharpoons x\,W + 3x\,Na_2WO_4 + (6 - 4x)\,WO_3$$
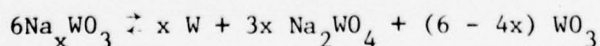
which was reported by Randin[23].

To test the effect of composition on the growth of ECT-grown tungsten bronze crystal, crystals were grown from 10 m/o WO_5 - Na_2WO_4 ($Na_{0.89}WO_3$) and from 45 m/o WO_3 - Na_2WO_4 ($Na_{0.6}WO_3$) melts. All of the <111> oriented crystals grown from these melts exhibited cross-sections which would be predicted by equation (2). Crystals grown from various melt compositions differed in the distance (d) due to differences in molecular weight (M), in the number of electrons transferred [n, where n = x (Eqn.1c)] and in the density (ρ) of the depositing crystal.

2. Deposition of Metals by ECT

Previous work was on a material with anisotropic growth behavior. Control of the diameter was difficult on seed orientations other than the fast-growth direction <111>. To further define the limits of the ECT process an effort was recently initiated to study the growth of materials with isotropic-growth behavior.

Crystals which show a high degree of anisotropy in their growth kinetics will have cross-sectional dimensions which can be predicted for ECT growth along the fast-growth direction. In other orientations, however, it has been shown that growth still proceeds along the fast-growth direction and the crystal does not exhibit dimensional stability but steadily increases its interfacial area and eventually loses contact with the melt. To test the role of anisotropic growth kinetics in stabilizing the cross section of the growing crystal, ECT growth of a more isotropic material was attempted.

The initial material chosen for this phase of the program was niobium. Niobium has been previously grown in the static mode in a similar system[7] and single-crystal seeds were available. The melt consisted of 6 mole % potassium hexafluoroniobate (K_2NbF_7) in a lithium fluoride (LiF) - potassium fluoride (KF) eutectic. Operating temperature was ~750°C. All melts were pre-electrolyzed to equilibrate the Nb^{IV}/Nb^{V} ratio.[24,25]

In its most general form, equation 2 may be written

$$v = \frac{K \varepsilon I}{A} \tag{4}$$

where A is the area of deposition, v the linear growth velocity and K is defined by

$$K = \frac{M}{nF\rho}$$

Equation 4 is only valid for a system which has a constant interfacial area (i.e. Czochraski type growth) and is based only on Faradav's laws. The value K (the growth rate constant) depends onlv on the molecular weight (M), the density (ρ) of the material being deposited and the number of electrons (n) transferred per unit of material deposited. Thus, the value of K is fixed for any given electrochemical process and when multiplied by 3600 sec/hr is expressed in units of cm^3 amp-hour.

The growth rate constant (K) for niobium was calculated to be 0.1011 cm^3/amp-hr compared to 2.136 for the growth of $Na_{0.8}WO_3$. Using equation (4) in the form

$$v = K \varepsilon i \qquad (5)$$

where i is the current density (I/A) and assuming $\varepsilon = 1$, the current density necessary to grow niobium at the rate of 1 mm/hr would would be 989 ma/cm^2 as compared to 47 ma/cm^2 necessary to grow $Na_{0.8}WO_3$ at the same rate. Due to the low solute content of the niobium melt (0.6 atom % niobium), this high value of current density could lead to dendrite formation. To avoid this possibility, previously-developed electropolishing techniques[7] were employed from the outset.

Initial experiments were conducted on static cathodes to study the system. Growths were performed on both polycrystalline and single crystal cathodes at a current density of 30 ma/cm^2 (growth rate: theoretical 0.03 mm/hr, experimental 0.028 mm/hr). Good deposits were obtained in all cases and those on the single-crystal cathodes were epitaxial.

Pulled growths were attempted on single-crystal seeds of various orientations (<100>, <110> and <111>). Initially <110> seeds were used and various combinations of cathodic and anodic currents were employed to optimize the deposition parameters. The parameters chosen were: cathodic current (I_c) 37.5ma; cathodic period (τc) 25 sec.; anodic current (I_A) 47 ma; anodic period (τ_A) sec. (average current 13.4 ma); pull rate 0.1 mm/hr; rotation rate 18 rpm and seed area ~0.1 cm^2. The values of I_c, τc, I_A, and τa are comparable to those used in the previous niobium experiments.[7] Laue patterns of initial deposits (24 hours or less) showed substantially epitaxial growth, while deposits over substantially longer growth periods (72 hours or more) were essentially polycrystalline. These results were the same on all three seed orientations employed. This behavior is consistent

with results of Setty and Wilmer.[26] The best result was a branched poly-crystalline growth whose diameter was predicted by equation (2).

The niobium system contains only 0.6 atomic % niobium of which only about half is Nb^{IV} which is the electroactive species. Since such low concentrations coupled with moderately high current densities (134 ma/cm^2) could lead to the type of problem encountered during these experiments, a new model system with higher solute concentration was sought. In order to facilitate experimental procedure the new system should operate at a low temperature and be noncorrosive, allowing operation in quartz. Several systems were considered and the ferrous chloride ($FeCl_2$) - potassium chloride system was chosen. This system has both a low melting eutectic (~390°C) and a high metal ion content (~55 mole % $FeCl_2$, ~18 atomic % iron) (Figure 7). Initial experiments with this sytem proved that Fe could be electrodeposited but only as dendrites even at moderate current densities (40 ma/cm^2). Application of electropolishing techniques did not signifi-cantly improve the deposits. Even if coherent deposits could be obtained at 40 ma/cm^2, the growth rate for Fe would be only 0.05 mm/hr since $K = 0.125$ cm^3/amp-hr.

The change to the iron system was made in order to increase the solute content of the system and, thus, to avoid what appeared to be a concentration-related problem in the niobium system. However, in the case of iron, dendrites formed at even lower current densities than those which produced polycrystalline deposits of niobium. Despic and Popov[27] have pointed out that most dendritic phenomena result from difficulties in the transport of the depositing ions. Thus, it appears that even with the high iron content of the $FeCl_2$-KCl melt rapid diffusion to the interface region is prevented by a low diffusion coefficient, perhaps due to complex formation in the melt.

Despic and Popov[27] have developed a criterion for the critical current density for the initiation of dendritic growth. In light of this criterion growth regime, it is desirable to operate at a low current density. To maintain an acceptable growth rate at a low current density, a material with a large growth rate constant (K) is necessary. (See Eqn. 5.) Calcula-tion of the values of K for most common metals showed that they fell in the
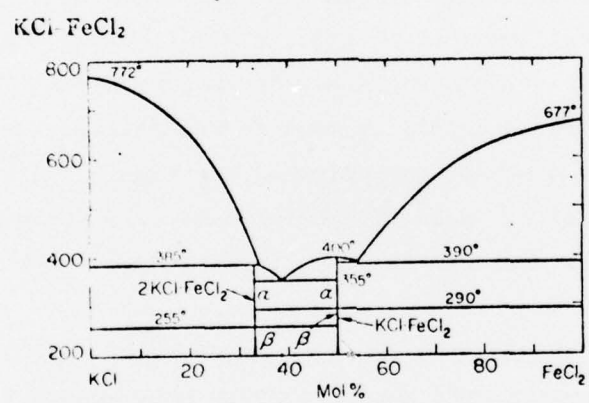
Figure 7. KC1-FeCl$_2$ System

range of 0.08 to 0.3 cm^3/amp-hr. (Notable exceptions are barium and calcium with values of 0.73 and 0.48 respectively.) If these constants are translated into current densities necessary to sustain growth at 1 mm/hr., the range of current densities is 333 to 1250 ma/cm^2. There have been several reports of current densities of this magnitude being used to produce metal powders.[28,29]

A long range program to grow metals by ECT would involve not only melt and substrate (seed) selection, but also an extensive study of electropolishing to optimize the values of the various parameters.

E.   Future Plans

While semiconducting compounds have been synthesized,[11,12] the information concerning their synthesis is limited. Future work in this area will emphasize an understanding of these systems. Initial experiments will center on the synthesis of GaP from a melt similar to that of Cuomo and Cambino.[11] When smooth, thin layers of this material have been obtained the melts will be modified to obtain InP. In addition, Yamamoto and Yamaguchi's[12] method for the deposition of ZnSe will be investigated as a model for the II-VI type semiconducting materials. When the binary systems have been investigated and the conditions for their deposition are understood, a similar approach will be applied to the ternary compound/ alloy semiconductor systems. Of particular interest may be the ternary alloys of the chalcopyrite or chalcogenide types (i.e. $CdGeP_2$, $CdInSe_2$).

In the area of continuous growth, studies will continue on the growth of materials with isotropic-growth behavior. In addition, the growth of anisotropic materials in directions other than the fast-growth direction will be studied.

References

(1)   U. Cohen and R. A. Huggins, "Silicon Epitaxial Growth by Electro-
      deposition from Molten Salts," presented at the Electrochemical
      Society Meeting, Dallas, Texas, October 5-10, (1976).

(2)   U. Cohen and R. A. Huggins, Jour. Electrochem. Soc. 123, 381 (1976).

(3)   D. Elwell, R. C. De Mattei, I. V. Zubeck, R. S. Feigelson and
      R. A. Huggins, J. Crystal Growth 33, 232 (1976).

(4)   D. Elwell, I. V. Zubeck, R. S. Feigelson and R. A. Huggins,
      J. Crystal Growth 29, 65 (1975).

(5)   R. A. Huggins, "Interface Stability During Electrodeposition from
      Molten Salts," presented at Electrochemical Society Meeting,
      Toronto, Canada, May 11-16, 1975.

(6)   R. A. Huggins and D. Elwell, "Control of Interface Morphology
      During Electrocrystallization from Molten Salts - Electrochemical
      Analog to Constitutional Supercooling," J. Crystal Growth (to be
      published).

(7)   U. Cohen and R. A. Huggins, "High Rate Electrodeposition of
      Niobium from Molten Fluorides Using Alternating Square Wave Pulses,"
      presented at Meeting of the Electrochemical Society, Dallas, Texas,
      October 5-10, 1975.

(8)   I. V. Zubeck, R. S. Feigelson, R. A. Huggins and P. A. Pettit,
      J. Crystal Growth 34, 85 (1976).

(9)   R. C. De Mattei, R. A. Huggins and R. S. Feigelson, J. Crystal
      Growth 34, 1 (1976).

(10) L. Andrieux, Ann. Chim. 12 (1929) 424.

(11) J. J. Cuomo and R. J. Gambino, J. Electrochem. Soc., 115,
      (1968) 755.

(12) A. Yamamoto and M. Yamaguchi, Japan J. Appl. Phys. 14 (1975) 561.

(13) G. H. Gilmer, R. Ghez and N. Cabrera, J. Crystal Growth, 8
      (1971) 79.

(14) R. De Mattei, Semi-Annual Technical Report, Long Range Materials
      Research, ARPA Order No. 2470-Amendment F. June 1975, p. 102.

(15) K. B. Morris and P. L. Robinson, J. Chem. Eng. Data. 9, 444 (1964).

(16) E. Banks and A. Wold, Prep. Inorg. React. 4, 237 (1968).

(17) P. G. Dickens and M. S. Whittingham, Quart. Rev. 22, 30 (1968).

(18) E. Banks, C. W. Fleischmann and L. Meites, J. Solid State Chem.
1, 372 (1970).

(19) C. T. Hauck, A. Wold, and E. Banks, Inorg. Synth. 153 (1970).

(20) R. A. Fredlein and A. Damjanovic, J. Solid State Chem. 4, 94
(1972).

(21) M. S. Whittingham and R. A. Huggins, NBS Special Publication, 364
51 (1972).

(22) H. R. Shanks, J. Crystal Growth 13/14, VIII-4 (1972).

(23) J. P. Randin, J. Electrochem. Soc. 120, 1325 (1973).

(24) G. W. Mellors and S. Senderoff, J. Electrochem. Soc. 112, 266 (1965).

(25) G. W. Mellors and S. Senderoff, Ibid. 113 (1966) 66.

(26) T. H. V. Setty and H. Wilman. Trans. Faraday Soc. 51 (1955) 984.

(27) A. R. Despic and K. I. Popov, Transport-Controlled Deposition
and Dissolution of Metals, in Modern Aspects of Electrochemistry
No. 7, ed. by B. E. Conway and J. O'M. Bockris, Plen Press, 1972.

(28) W. J. Kroll Trans. Electrochem. Soc. 87 (1945) 551.

(29) F. P. Haver, et al., U. S. Bur. Mines, Rep. Invest. (1976) R. I.
8133.